Coherent structures in the boundary plasma of EAST Tokamak

Yan, Ning

Publication date:
2014

Document Version
Publisher's PDF, also known as Version of record

Technical University of Denmark

Department of Physics

Coherent structures in the boundary plasma of EAST Tokamak

Ning Yan

Copenhagen, Apr, 2014

Abstract:

In recent years, with the application of fast camera in fusion plasma, as well as other diagnostic of spatial-temporal resolution such as Langmuir probe, it has become generally clear that the turbulence transport is mostly dominant by cross-field propagation of coherent structures, namely blobs or filaments in low-confinement mode (L-mode). Analogously, the fine structures associated with the edge-localized modes (ELMs), i.e., ELM filaments, have been shown to be the main carriers of the transport in the high-confinement mode (H-mode). The filaments carry particles and heat, impinging upon the plasma-facing material, leading to intensive transient heat load and particle load on the local areas of both the divertor target plates and the first wall, which damages the material and causes enhanced recycling and impurity generation, then further pollutes the core plasma. In this project, we carried out experiment in the boundary plasma using multi-pin Langmuir probe in L-mode discharge. It was found that the coherent structures (Blobs and Holes) are created in the edge shear layer of poloidal flows where the plasma shows steep pressure gradient. Simulations have been performed using the ESEL code, which is a 2D fluid turbulence-simulation code based on the interchange instability as the main drive for the turbulence and structure motion in the scrape-off layer (SOL) plasma, with the input parameters from the EAST experiments. The simulations successfully reproduce the statistical characteristics of the SOL turbulence as well as the profiles of the plasma main parameters measured by the Langmuir probes on EAST. Our observations suggest that the coherent blobs/filaments are generated from the interchange driven instability. On the other hand, an improved understanding on the particle and heat transport by ELM filaments has been obtained though intensive research in different machines. Nevertheless, it is still rather unclear about the ability of current transport in ELM filaments in the international fusion community. A Langmuir-magnetic probe array has been used to study the electromagnetic features of the ELM filaments in the SOL or slightly inside the separatrix. It is observed that the topological configuration of density and potential in the ELM filaments deviate from each other. Furthermore, isolated electromagnetic filaments have been clearly identified during the type-I-like ELMs. They propagate radially outwards and poloidally in the electron diamagnetic drift direction. Based on the reconstruction of the topological structure from the associated magnetic perturbations, we demonstrate that the ELM filaments carry mono-polar current, which provides important evidence for current transport by filamentary structures at the plasma edge. These studies further improve our understanding on the characteristics of filaments and the transport mechanism in the fusion plasma boundary.

Dansk résumé:

Fusionsenergi, der udvikles når to brint isotoper – f.eks. deuterium og tritium - fusionerer, vil blive fremtidens uudtømmelige og miljøvenlige energikilde. Fusionsenergi kan udvikles i et 100 mill grader varmt plasma, der er indesluttet i et toroidalt kammer ved hjælp af et magnetisk felt. En af de store udfordringer er at holde plasmaet indesluttet i tilstrækkelig tid for at fusionsprocesserne kan producere energi overskud. Det har vist sig at turbulente fluktuationer er en dominerende mekanisme for transport af plasma ud af den magnetiske indeslutning. Det er derfor af højeste prioritet inden for fusionsforskningen at forstå denne transport mekanisme og ultimativt blive i stand til at kontrollere den. Gennem de senere år er der sket store fremskridt på denne front, både eksperimentelt og teoretisk. Specielt er de diagnostiske metoder, der anvendes ved eksperimentelle undersøgelser af magnetisk indesluttede fusions plasmaer, blevet signifikant forbedrede. Det gælder især anvendelsen af hurtige kameraer, som gør det muligt at undersøge plasma dynamikken både rumligt og tidsligt opløst. Dette, kombineret med andre diagnostiker, såsom arrays af Langmuir sonder, har gjort det muligt, at undersøge den detaljerede udvikling af plasma turbulensen og den afledte transport, hvilket har bidraget til udvikling og verificering af modeller, som kan forudsige den turbulente transport.

Det har vist sig at transporten for det meste er domineret af udbredelse af sammenhængende strukturer, såkaldte plasma blobs, som bærer det varme plasma ud af det indesluttende magnetfelt i klumper. Disse strukturer er lokaliserede i planen vinkelret på magnetfeltet og tager form af langstrakte filamenter langs med magnetfeltet. Dette gælder for langt de fleste plasma tilstande. Specielt i den såkaldte høj-indeslutnings tilstand – H-mode – vil disse klumper af varm plasma – plasma blobs - føre til meget kraftig energiafsætninger og dermed opvarmning af kammer væggene og de materialer, som plasmaet kommer i berøring med. Det medfører skader på materialerne og forårsager afdampning af materiale, som forurener plasmaet, hvorved fusionseffektiviteten falder.

Dette projekt omhandler detaljerede eksperimenter i randområdet af et toroidalt magnetisk indesluttet plasma, som gør brug af den avancerede diagnostik, der er omtalt ovenfor. Specifik er dynamikken af de omtalte plasma blobs og deres bidrag til transporten blevet klarlagt. Eksperimenterne er udført i EAST (Experimental Advanced Superconducting Tokamak) ved Institut for Plasma Physics (IPP) of the Chineese Academy of Science (CAS), Hefei, Kina. De eksperimentelle resultater er blevet sammenlignet med og suppleret af simuleringer, udført med ESEL koden (udviklet på DTU Fysik), som er en 2D fluid baseret kode, der modellerer plasma dynamikken i kantområdet af magnetisk indesluttede plasmaer, og specielt inkluderer det såkaldte “scrape-off layer” (SOL) plasma, hvor magnetfeltlinerne har kontakt til

materielle overflader. Med inputparametre fra EAST eksperimenter har simuleringerne vist detaljeret overensstemmelse med de eksperimentelle resultater. Observationerne viser, at de kohærente plasma blobs genereres ved udviklingen af instabiliteter i plasma randområdet og accelereres ud gennem SOL mod kammer væggen. Herudover er der ved hjælp af målinger af topologien af magnetiske perturbationer, blevet klarlagt at disse blobs bærer en betydelig strøm langs magnetfeltet. Strømmen kan tage både en dipolar og monopolar form, afhængig af plasma tilstand og parametre. Disse undersøgelser har bidraget med vigtig ny forståelse af plasma transport og specifikt af dynamikken af plasma blobs, disses bidrag til transport og energi afsættelse på materialer der “ses” af plasmaet.

Acknowledgements

Thanks to my supervisor Volker Naulin for providing me the great PhD project together with the instructive advice and support on it. I sincerely acknowledge my co-supervisor Baonian Wan and Guosheng Xu for their guidance on the design of scientific experiments. It is grateful for the patient and fruitful discussion from Jens Juul Rasmussen, Anders Henry Nielsen, Jens Madsen. I appreciate the kind support from my colleagues in PPFE, especially the PhD fellows: Asger Schou Jacobsen, Frederik Treue and Michael Løiten Magnussen. My thanks are also given to the colleagues in EAST boundary team, Zhang Wei, Wang Huiqian, Wang Liang, Liu shaocheng, Shao Linming and so on, who suffer from handling the diagnostics together with me in the deep night.

Finally, I would like to thank my family for supporting me during this period.

This work was supported by the Department of Physics, Technical University of Denmark, DTU; Institute of Plasma Physics, Chinese Academy of Sciences; Sino – Danish Center for Education and Research.

Contents

Chapter 1

Introduction

1.1. Fusion energy

At present, 80% of the human consumed energy comes from fossil fuels, such as coal, gas and oil. fossil fuels are not renewable, and the reserves will be exhausted in several hundred years at present consumption levels. On the other hand, the emissions of CO_2, H_2S from the fossil energy lead to a global warming and climate change on the earth. A alternative new energy are expected not only to supply our increasing energies demand from economics growth but also to be advantageous for our environment optimization. Several sustainable energy schemes, such as solar power, wind energy, biomass, and nuclear power are developed to replace the fossil fuels. Among them, fusion power is the prime candidate for a future source of sustainable energy. It is clean, safe, efficient, and available in billions of years. Nuclear fusion is the fundamental process that the sun generates its power. As a magnetic confinement device, the tokamak, is supposed to be the best way, which can achieve the generation of fusion power by technical means on the earth. Research tokamaks at present provide important indication for the realization of fusion energy from burning plasmas.

1.1.1 Binding energy

Atomic nuclei are composed of protons and neutrons, each of which weighs about the same, but has a different electric charge: positive elementary charge for protons and no charge for neutrons. Binding energy is defined as the energy required to disassemble a nucleus at a given mass number into free neutrons and protons. The higher binding energy per nucleon of an atom the more stable the atom is, thus the binding energy could be interpreted as a negative of potential energy. Quantitatively, the binding energy is calculated as a product of the lost mass and the square of light speed ($E = mc^2$) [1]. To estimate the lost mass, one sums the mass of the individual nucleons and subtracts the mass of the atom itself. According to the distribution of binding energy in different atoms shown in figure 1.1, the binding energy of elements near the middle of the periodic table is higher than either ends. It peaks at the elements with a mass number around 56, i.e. iron Fe^{56}. To convert atoms at either ends of the periodic table to atoms in the middle will increase the binding energy and equivalently decrease the potential energy. As a result, the reduced potential energy will be converted to the kinetic energy and/or radiant energy of atoms. This knowledge implies two methods towards the converting of mass into useful amounts

of energy: splitting large nuclei into smaller ones (fission) or combining small nuclei into larger ones (fusion).

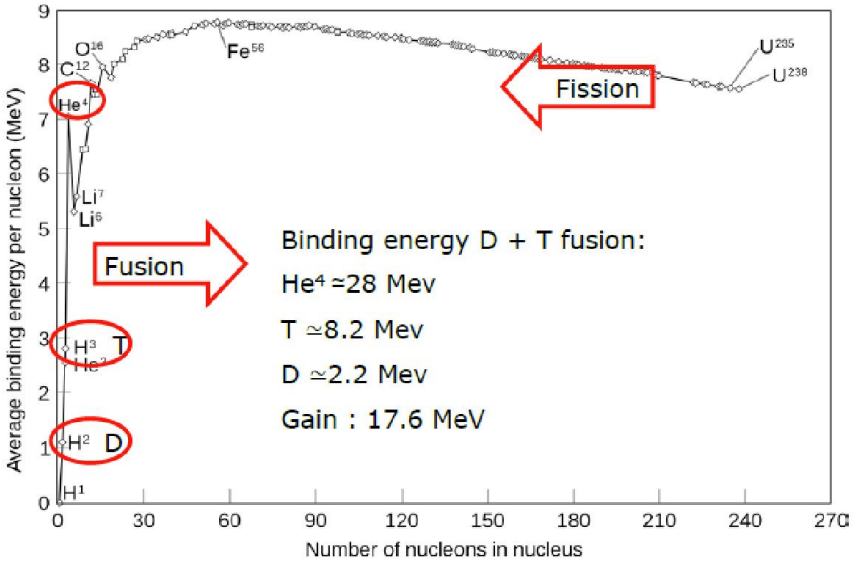

Figure 1.1. Binding energy vs. atomic number for all elements from hydrogen to uranium.

At present, the deuterium-tritium (D-T) reaction is most viable fusion process for its high reaction rate [2].

$$ {}_{1}^{2}\mathrm{D}+{}_{1}^{3}T \rightarrow {}_{2}^{4}He(3.52\mathrm{MeV})+{}_{0}^{1}\mathrm{n}(14.06\mathrm{MeV}) \qquad (1.1) $$

As described in equation (1.1), each D-T reaction can produce a fusion energy E_{fusion}=17.6MeV in the form of kinetic energy of the neutron (14.1MeV) and the alpha particle (3.5MeV). Distinct from fission, the fusion reaction does not produce radioactive nuclear waste, and there is no danger of uncontrolled nuclear chain reactions. Moreover, fuel supplies are almost inexhaustible, since deuterium can be extracted from water, and tritium can be bred from the lithium element. Fusion power is believed to be a future source of clean and sustainable energy.

1.1.2 Burning Plasma

It is well known that the matter exists usually in the form of solid, liquid and gas. The solids can be transferred to liquids, and liquids could be vaporized to gases if the matter keeps absorbing heat energy. Plasma as ionized gas at high temperature is often termed as the forth state of matter. In hot plasma, the thermal velocity of atoms is very high, and collisions between atoms knock electrons away from their nuclei. The charged particles transfer their energy through random coulomb collisions. The velocity of hot particles in plasma near thermal equilibrium will obey a Maxwellian/Gaussian distribution. Plasmas are composed of same numbers of charged nuclei and electrons. It tends to be quasi-neutral on the whole. Nevertheless,

the separation of electrons and ions raise a finite electric field inside a plasma. This also means that plasma can create, and respond to, electric and magnetic fields, which makes plasma behave in much more complicated ways than does gas.

To achieve fusion reaction in plasma, nuclei have to overcome their mutual electric repulsion. The higher the kinetic energy of nuclei, the more chance a fusion reaction takes place. Thus, the energetic nuclei in the tail of Maxwellian energy distribution are much easier to ignite a fusion reaction. The fusion reaction rate (i.e. number of reactions per volume) f is proportional to the product of cross-section σ and relative velocity υ of nuclei. It is defined as $f = n_1 n_2 < \sigma\upsilon >$, where n_1 and n_2 present the density of two light elements in plasma, sharp bracket < > is a operator for ensemble average[3]. Suppose deuterium density n_D and tritium density n_T are equal ($n_D + n_T = n_e$) in the fusion plasma, the produced fusion power is calculated as:

$$P_{fusion} = \frac{1}{4} n_e^2 < \sigma\upsilon > E_{fusion} \qquad (1.2)$$

In order to self-sustain the thermal fusion reaction, the output fusion power itself should be able to compensate the energy loss P_{loss} from the plasma. Here $P_{loss} = 3n_e T_i / \tau_E$, T_i is the ion temperature in eV, and τ_E is the energy confinement time in units of s ($\tau_E = E/(P - dE/dt)$, where E is the plasma energy and P is the total heating power). A criterion given in equation (1.3) defines a requirement for the ignition of fusion plasma :

$$n_e T_i \tau_E > 3 \times 10^{21} m^{-3} keVs \qquad (1.3)$$

The expression of triple product is an extension form of the well known ‘Lawson-criterion’ [4]. In a future D-T power plant, the energy of alpha particle retained in plasma is sufficient to maintain the fuels at thermonuclear temperature without any external heating power.

1.2. Tokamak device

In the laboratory, scientists devote themselves to explore an effective approach to fuse together deuterium and tritium. They manage to create the optimum fusion conditions by heating low density plasma to much higher temperatures of 100 million degrees Celsius. The high temperature required by burning plasma poses a substantial challenge for the realization of fusion power. No solid material can be used as a direct container for burning plasma, since none can withstand temperatures of millions of degrees. Magnetic fields have been selected as a prime candidate to confine and control charged particles. With the help of magnetic confinement, high temperature gradients between the plasma and the containing vessel can be maintained, which keep the plasma hot and the wall of vessel cool. Some machines such as tokamak,

stellarator, etc. are set up with magnetic confinement system to implement the fusion reaction.

The scientific research in this work is carried out on a tokamak machine. Therefore, we will briefly introduce the principle and setup of tokamak device in this section. The tokamak machines may differ from each other in details, but their main concept is the same.

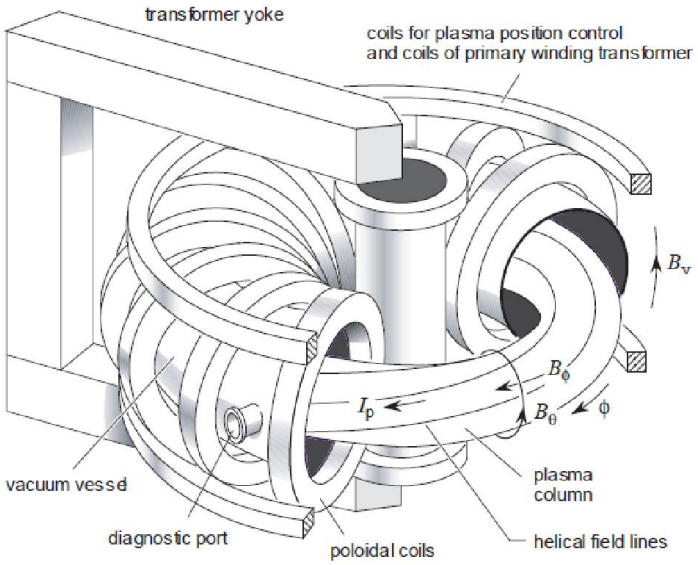

Figure 1.2. Schematic view of a tokamak

As illustrated in figure 1.2, the magnetic configuration of tokamak looks like a tire of a car. The hot plasma is expected to be trapped in the magnetic loop. Specifically, the toroidal magnetic field B_ϕ is generated by the external poloidal magnetic coils spaced equidistantly in the toroidal direction. B_ϕ in tokamak is not uniform ($B_\phi \propto 1/R$, where R is the major radius of magnetic flux surface). The poloidal magnetic field B_θ is produced by the plasma current I_p conducting in the toroidal direction. The resulting helical magnetic field lines circle around the surface of the torus. The magnetic configuration of a tokamak can be depicted as a set of nested magnetic surfaces, whereas the innermost surface (B_θ=0) is just a line: the magnetic axis.

For an given magnetic field line on a magnetic flux surface with minor radius r, the number of toroidal turns required to execute one full poloidal turn is called the safety factor. In the case of a cylindrical tours with a large aspect ratio (the ratio R_0/a of major and minor radius), safety factor q is approximatly written as:

$$q = \frac{rB_\phi}{RB_\theta} \qquad (1.4)$$

q is used to measure the pitch of the helical field lines All field lines on a given same magnetic surface are of the same q .

The charged particles confined in tokamaks are of different parallel kinetic energy and perpendicular kinetic energy. The parallel velocity $v_{//}$ along the magnetic field lines leads them to move freely along the magnetic field lines. The particle with perpendicular velocity across the magnetic field lines $v_{\perp}$ experience the well known Lorentz force $F = zv_{\perp} \times B$, where z is the charge of the particle, B the magnetic field. The Lorentz force does not affect the kinetic energy of particles, but it changes the direction of perpendicular motions and cause a so-called gyration. The radius of the circular motion is called the gyroradius or Larmor radius ρ and the frequency is the cyclotron frequency ω_c . To be specific, $\rho = mv_{\perp}/|z|B$, $\omega_c = |z|B/m$, where the m denotes particle mass. They are used to characterize the spatial and temporal scale of a charged particles.

In a non-uniform magnetic fields, the Larmor radius vary with the strength of B. Figure 1.3 shows the dynamics of electrons and ions in the magnetic field of tokamak. The Larmor radius of ions is larger than of electrons due to heavier mass. As a result of the radial gradient of B, the guiding centers of charged particles deviate from their original location. They drift across B with a velocity perpendicular to the gradient of magnetic field ▽B, which is called 'grad B drift'. In general, any steady force F affecting the perpendicular kinetic energy of particles is able to accommodate the Larmor radius during a gyromotion. This creates a cross field drift velocity ($v_F = F \times B/qB^2$) of plasma. A centrifugal force $F_c = mv_{//}^2/R$ originates from the toroidal geometry of magnetic field lines induce a 'curvature drift'. The cross field drift of plasma due to electric field **E** is called 'E×B' drift.

$$v_{\nabla B} = -\frac{mv_{\perp}^2}{2qB^3}\nabla B \times B \qquad (1.5)$$

$$v_{curv} = \frac{mv_{//}^2}{R}\frac{\vec{R} \times B}{qB^2} \qquad (1.6)$$

$$v_{E\times B} = \frac{E \times B}{B^2} \qquad (1.7)$$

The direction of ▽B drift and curvature drift depend on the polarity of charge of particles, thus the ▽B drift and curvature drifts consequently separate the ions and electrons. On the contrary, the E×B drift is charge independent, which does not break down the quasi-neutrality prevails of plasma.

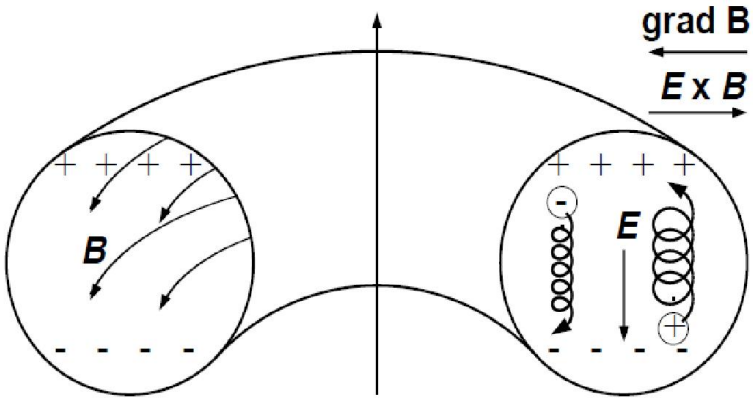

Figure 1.3. Charged particles gyrate around the magnetic field lines. Gradient and curvature of magnetic field drive the electron and ions to drift in opposite direction

As shown in the figure 1.3, assuming there is only toroidal magnetic field in tokamak, the ions and electrons drift vertically in opposite directions due to the curvature and radial gradient of magnetic field. The separation of ions and electrons in turn establishes a vertical radial electric field **E**. With the vertical radial electric field E, plasma will collectively drift outwards and turn to be out of control. In order to balance the charge separation, the poloidal magnetic field is demand to circuit the ions and electrons that tend to accumulate in the top and bottom of the magnetic torus.

1.3. Boundary plasma

1.3.1 Limiter and Divertor configuration

The essence of magnetic confinement is to isolate the confined hot plasmas from the wall of vacuum vessel. To achieve this goal, the closed magnetic flux surface should be kept apart from the first wall of the tokamak machine with a spatial distance. Technologically, limiter and divertor configurations are two typical approaches implemented in the tokamaks.

The poloidal cross section view of limiter and divertor plasma is depicted in figure 1.4. In a limiter discharge, the poloidal magnetic field is mainly created by plasma current I_p, and It is approximately circular. The closed magnetic flux surfaces are transmuted into open field lines once they interact with a surface of solid limiter. Hence, the leading edge of the limiter defines the position of the last closed flux surface (LCFS). In a divertor configuration, the poloidal magnetic field is created not only by plasma current I_p but also with an external conductor carrying a current I_D in the same direction with I_p. The poloidal magnetic field generated by I_p and I_D cancel

each other at so-called X-point. The magnetic flux surface passing through the X-point is called the magnetic separatrix or LCFS.

The magnetic field lines in the region between closed magnetic field surface and the first wall are open to the solid surface of limiter or divertor target. This intermediate zone is called scrape-off layer (SOL). Plasmas in SOL are apt to move along the magnetic field line rather than to diffuse across due to higher mobility in parallel direction. A majority of particles in the SOL eventually strike the limiter or divertor plate, where the intersection of magnetic field lines and solid surface are known as strike points. The limiter and divertor plates are thus expected to be tough enough to accommodate the power load and particle flux.

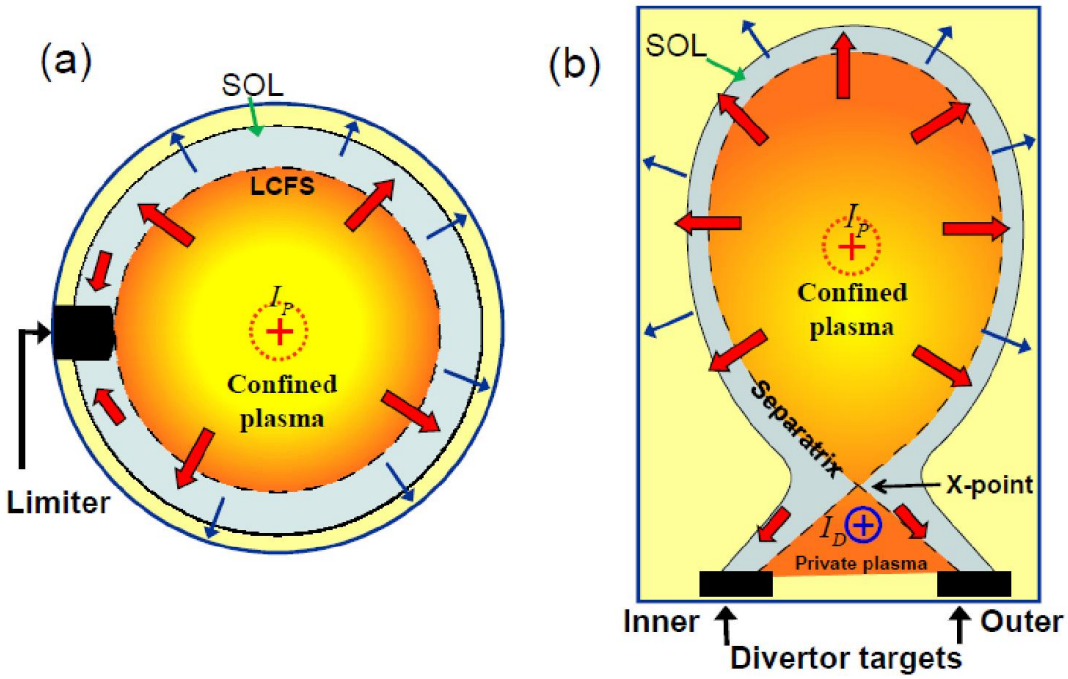

Figure 1.4. The poloidal cross section of a limiter (left) and divertor (right) plasma.

1.3.2 Edge shear layer

The radial electric field E_r is known to play a key role in confinement improvement of plasma in tokamak. A naturally occurring E_r layer in the edge plasma has been ubiquitously observed in toroidal magnetic confinement devices [5-14]. Particularly, a deep negative E_r well is found to establish spontaneously inside the LCFS at the transition from low energy confinement state (L-mode) to a higher energy confinement state (H-mode) [15-17], which is accompanied by a steepening of the edge profiles, or formation of a edge transport barrier (ETB). The confinement improvement at L-H transition is usually characterized by a fast drop of the $H_\alpha(D_\alpha)$ signal at divertor target and an abrupt quenching in plasma turbulence. The

pronounced E_r well persists in H-mode and is a distinctive and characteristic feature of H-mode plasmas.

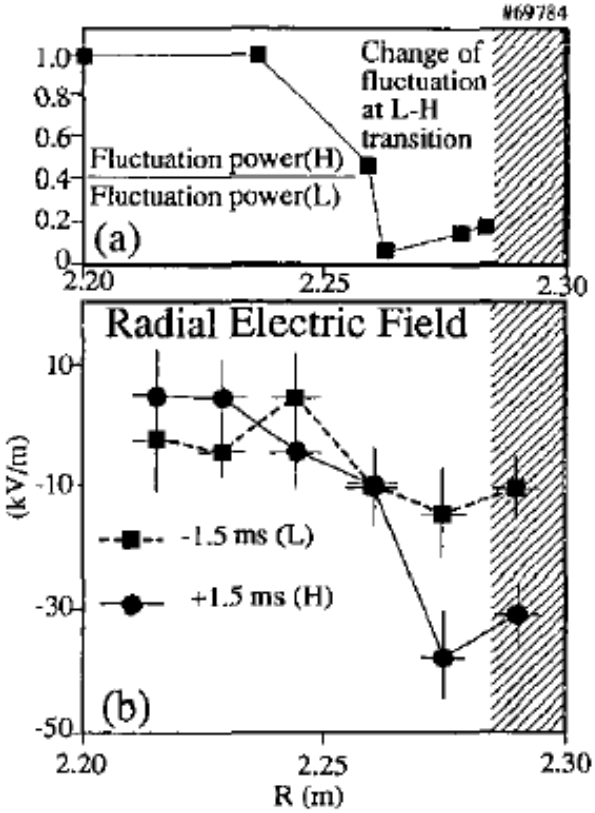

Figure 1.5. Comparison of the sheared radial electric field and the suppression of the edge fluctuation on DIII-D. (a) Change of density fluctuation at the L-H transition. (b) Changes in the radial electric field at the L-H transition [18].

The evolution of equilibrium radial electric field couple with the dynamics the pressure gradient and the flow velocity of ions though the radial force balance equation [19]:.

$$E_r = \frac{1}{Zen_i}\nabla_r P_i + V_{\phi i}B_\theta - V_{\theta i}B_\phi \qquad (1.8)$$

Here, the P_i is the ion pressure, Z is the ion charge number, e is the elementary charge, n_i is the ion number density and the subscripts θ and ϕ indicate the components of the poloidal and toroidal ion rotation velocity and magnetic field. All these three terms on the right hand of the equation (1.8) together with the radial electric field are observed to undergo a substantial change simultaneously at the L-H transitions[5, 20]. Therefore, although the previous works notice that the edge E_r is strongly affected by the L-H transition, it is still difficult to identify whether the equilibrium E_r is the cause or consequence of improved confinement in the H-mode.

The origin of the radial electric field could be very complicated. A variety of mechanisms such as Stringer–Hassam poloidal asymmetric driving force [21, 22], ion orbit loss effect [23, 24], turbulence-induced Reynolds stress [25, 26] have been proposed to modify the E_r in detail. However, the development of E_r at L-H transition is still not fully understood yet.

1.3.3 SOL sheath

Assuming a electrically floating solid object inserted into plasma, a plasma sheath layer will be established at the interactional surface in few microseconds due to the imbalance of dynamics of electrons and ions in plasma. The thermal velocity of electrons is significantly larger than it of the ions, hence the electron flux take over the solid surface and charge them negatively once the plasma are contacting the solid surface. The collective electrons in turn repel the following electrons. A slight displacement between ions and electrons produce an potential barrier at the contacting surface of solid object. The resulting ambipolar electric field slows the loss rate of electrons and enhances the loss rate of ions in plasma. This potential barrier here is termed Debye sheath. Plasma outside of Debye sheath is deemed quasi-neutrality.

In the SOL, a parallel electric field are provoked to balance the electron pressure, i.e. force balance between a parallel pressure gradient force pushing the electrons toward the surface, and the retarding electric field force. The parallel electric field penetrates throughout the whole SOL. By this fact, the SOL plasma itself could be regarded as a pre-sheath. On the other hand, the parallel electric field accelerate ions downwards the pressure gradient of plasma.

In a pre-sheath, the fluid velocity u of ions increases towards the solid surface of limiter or divertor, and it must reach a value of at least the sound speed c_s at the sheath edge of limiter or divertor. This is known as the Bohm criterion:

$$u \sim c_s \qquad (1.9)$$

The parallel electric field in the pre-sheath serves to accelerate the ions to c_s. The ion flux density striking at the solid surface edge (along the magnetic field lines) is conserved from the time it enters the sheath edge. It reads:

$$J_i = nc_s e \qquad (1.10)$$

Where the plasma density at the sheath edge is n. The electron flux strike the solid surface and charge the solid object to a potential ϕ with respect to the potential at the sheath edge. The electron flux density at the solid surface is derived as:

$$J_e(\mathrm{x}) = \frac{n\cdot(-e)\cdot e^{-(-e)\phi/kT_e}}{\sqrt{2\pi kT_e/m_e}}\int_0^\infty v e^{-mv^2/2kT_e}dv$$

$$= -ne\sqrt{\frac{kT_e}{2\pi m_e}}e^{e\phi/kT_e} = -nec_s\sqrt{\frac{kT_e}{2\pi m_e c_s^2}}e^{e\phi/kT_e} \qquad (1.11)$$

The equilibrium ion current density is supposed to cancel the electron current density at the solid surface edge, otherwise it will charge the plasma and the quasi-neutrality of plasma will be broken drown.

The total parallel current density reads:

$$J_{//} = J_i + J_e = enc_s(1-\exp(\ln\sqrt{\frac{kT_e}{2\pi m_e c_s^2}} + \frac{e\phi}{kT_e}))$$

$$= enc_s(1-\exp(\Lambda + \frac{e\phi}{kT_e})) \qquad (1.12)$$

Here, $\Lambda = \ln\sqrt{\frac{kT_e}{2\pi m_e c_s^2}} \approx 2.5$ for a hydrogen plasma.

When $\phi \approx -2.5kT_e/e$, the electron losses equal the ion loss, and the net current cross the solid surface becomes zero. This potential is called the floating potential V_f. An insulated object immersed in plasma will always charge to a floating potential. The floating potential is more negative than the sheath potential by -2.5 kT_e/e, which ensures that no net current flows to the object.

The potential drop V_{se} in pre-sheath could be deduced according to ion energy conservation $\frac{1}{2}m_i c_s^2(\mathrm{x}) = eV_{se}$, provided that the ion velocity in plasma center is zero. We further obtain the plasma density n_0 in the center, through the expression:

$$n = n_0 e^{-e\phi_{se}/kT_e} = n_0 e^{-1/2} \sim n_0/2 \qquad (1.13)$$

Hence, the plasma density at the sheath edge is about half of the density in the plasma center. The potential drop V_{se} across the pre-sheath is about -0.5kT_e/e. The floating potential relates to the plasma potential as $V_f \sim V_p$ -3kT_e/e. Note that although the potential drop in pre-sheath electric field is much smaller than that in the sheath, it is of critical importance to transfer a considerable amount of energy from the electrons to the ions. The electric potential of a plasma in different location is illustrated in figure 1.6.

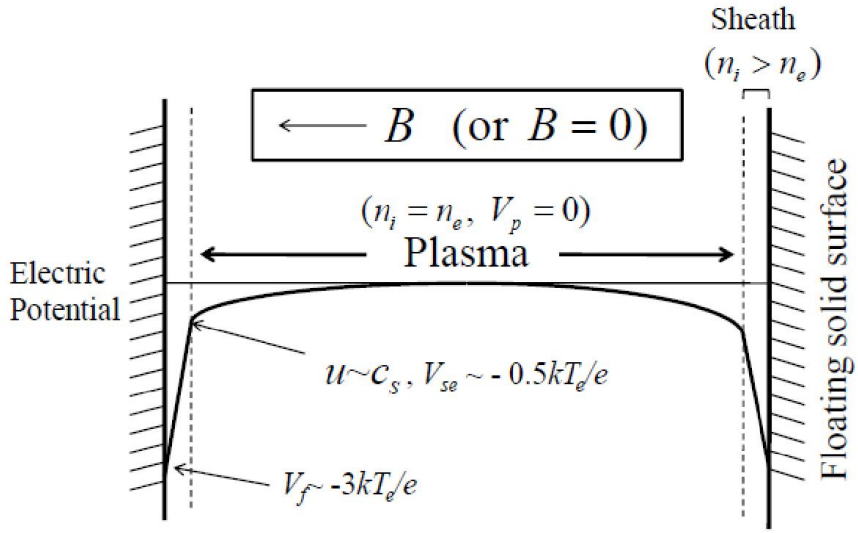

Figure 1.6. Schematic of the variation of electric potential in the plasma between two semi-infinite planes. The thickness of the sheath is exaggerated for clarity.

1.3.4 Turbulence and transport in boundary plasma

Considering a tokamak device, people address the region inside the normalized radius r/a ~ 0–0.9 as ‘core’, and the region at r/a ~ 0.9–1.0 as 'edge'. The region outside of the LCFS r/a >1.0 is the 'SOL'. Here , 'r' denotes the minor radius of any magnetic flux surface and 'a' signifies the minor radius of the LCFS. The integrated region of edge and SOL is called boundary in tokamak. The plasma density and temperature in the core and boundary are distinct. Density and temperature in core plasmas can be 10-100 times higher than that in the boundary plasmas.

The physical situation of the plasma strongly depends on plasma parameters. There are three factors can significantly impact the performance of electrons in magnetically confined plasma: inductivity $\hat{\beta}$, electron inertia $\hat{\mu}$ and collisionality C [27, 28].

$$\hat{\beta}=\frac{4\pi P_e}{B_0^2}\left(\frac{L_{//}}{L_\perp}\right)^2, \quad \hat{\mu}=\frac{m_e}{M_D}\left(\frac{L_{//}}{L_\perp}\right)^2, \quad C=\frac{0.51\nu_e}{C_s/L_\perp}\hat{\mu} \quad (1.14)$$

Here, P_e presents the electron pressure, B_0 the equilibrium magnetic field. $L_{//} \sim qR$ the parallel scale length, $L_\perp$ the profile scale length. q the safety factor, R the major radius of torus, ν_e the electron-ion collisinality. The masses of electron and ions are denoted by m_e and M_D, respectively. Parameter $L_{//}/L_\perp$ characterizes the parallel/perpendicular scale ratio, which is in the range of 100-200. Inductivity, electron inertia and collisionality impede the free motion along the magnetic field

lines. In core plasma $\hat{\mu}$, C are very small and $\hat{\beta}$<1, the electron response along the magnetic field lines can be regarded as adiabatic. In other words, the electron parallel dynamics is arbitrarily fast. In Edge/SOL plasma $\hat{\mu}$>1, C>1, $\hat{\beta}$>1 ,the electron response is always nonadiabatic. In the core plasma, the higher mobility of electrons will lead the density perturbations $\tilde{n}$ and potential perturbations $\tilde{\varphi}$ of electrons to obey a Boltzmann relation:

$$\tilde{n} = n_0 \exp(\frac{e\tilde{\phi}}{T_e}) \sim n_0 \frac{e\tilde{\phi}}{T_e} \qquad (1.15)$$

where the density and potential fluctuations are in phase $\tilde{n}/n_0 \sim e\tilde{\phi}/T_e$. Due to the much higher mobility of electrons compared to the ions, they move out of density maxima into minima along the magnetic field lines and leave the ions behind. As illustrated in figure 1.7, for a drift-wave, the corresponding E×B velocity will establish with density and potential fluctuations and make them stably propagating in the electron diamagnetic $V_{dia,e}$ direction.

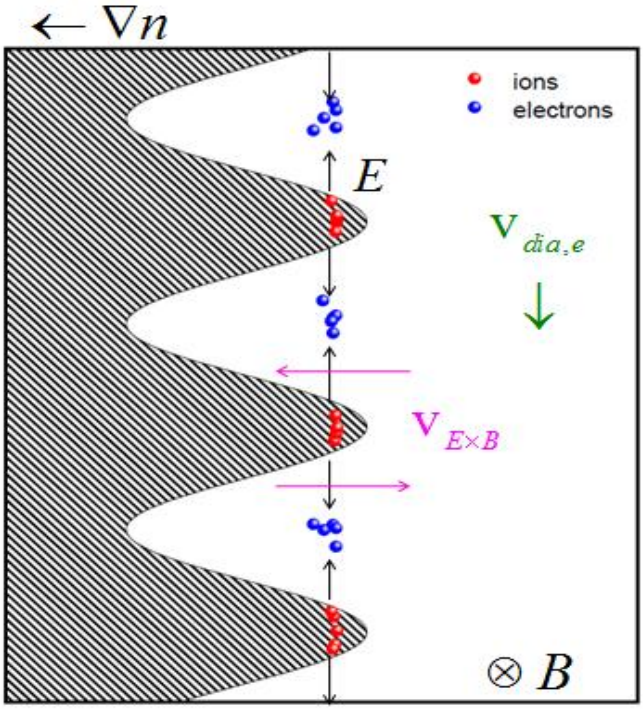

Figure 1.7. Isodensity Contour for a single drift wave mode.

However, the physical scenario of plasma turns to be very complex in the real situation. As aforementioned, the plasma resistivity, magnetic induction, electron inertia can inhibit the parallel electron motion and cause the non-adiabaticity of electrons. As a result, the propagation of the potential perturbations is delayed relative to the propagation of the density perturbations. The cross-phase between density and

potential fluctuations gets larger than zero. To get better understanding on the physics behind this point, two field $(\tilde{n},\tilde{\varphi})$ fluid models for the dynamics of low-frequency density and electrostatic potential fluctuations in a purely toroidal magnetized low-β plasma are reviewed in this section.

Before we go to the dedicated turbulence models, some vectors and mathematical operators are clarified in advance to simplify notation in our expressions.

$$\vec{B} = B \cdot \mathbf{b}$$
$$\boldsymbol{\kappa} = \vec{B} \cdot \nabla \vec{B} = -\vec{R}/R$$
$$\mathbf{g} = \nabla \times \frac{\mathbf{b}}{B} = \frac{\mathbf{b} \times \nabla B}{B^2} + \frac{\nabla \times \mathbf{b}}{B} \approx 2\frac{\mathbf{b} \times \boldsymbol{\kappa}}{B} \approx -2\frac{\mathbf{z}}{B}$$
$$\mathbf{v}_E = B^{-1}\mathbf{b} \times \nabla_\perp \tilde{\phi} = c_s \rho_s \mathbf{b} \times \nabla_\perp \hat{\varphi}$$
$$\mathbf{g} \cdot \nabla \tilde{\phi} = \nabla \cdot \mathbf{v}_E \approx 2\frac{\mathbf{b} \times \boldsymbol{\kappa}}{B} \cdot \nabla \tilde{\phi} = -2\mathbf{v}_E \cdot \boldsymbol{\kappa} = 2c_s \rho_s \mathbf{b} \times \boldsymbol{\kappa} \cdot \nabla \hat{\varphi}$$
$$d_t = \partial_t + \mathbf{v}_E \cdot \nabla_\perp$$

Ion gyro-frequency $\omega_{ci} = eB/m_i$ and the (hybrid) thermal gyro-radius $\rho_s = c_s/\omega_{ci}$ are important parameters which is often chosen to characteristic temporal and spatial scales of particle dynamics. Here, *R* is the magnetic field radius of curvature, and **g** is equal to the electron grad *B* and curvature drifts. $\mathbf{v}_E$ is the E×B drift velocity, d_t is termed convective derivative.

Resistive drift-wave turbulence:

The evolution of plasma density and the plasma potential is governed by the continuity equations of ions and electrons. Here, we divide the density fields into a stationary n_0 and fluctuating components $\tilde{n}$. The relative density fluctuations is denoted as $\hat{n} = \tilde{n}/n_0$. An explicit equation for the E×B vorticity can be derived by subtracting the electron and ion continuity equations. With the assumption of isothermal plasma and cold ions, the electron density continuity equation (1.16a) and E×B vorticity equation (1.16b) respectively read as follows:

$$d_t\tilde{n} + B^{-1}\mathbf{b} \times \nabla\tilde{\phi} \cdot \nabla_r n_0 = \frac{T_e}{e}\mathbf{g} \cdot \nabla\tilde{n} - n_0\mathbf{g} \cdot \nabla\tilde{\phi} + n_0\sigma_\parallel\left(e\tilde{\phi}/T_e - \tilde{n}/n_0\right) + D\nabla_\perp^2\tilde{n} \quad (1.16a)$$

$$d_t\varpi = \frac{T_e}{en_0}\mathbf{g} \cdot \nabla\tilde{n} + \sigma_\parallel\left(e\tilde{\phi}/T_e - \tilde{n}/n_0\right) + \mu\nabla_\perp^2\varpi \quad (1.16b)$$

Where the E×B vorticity $\varpi = \rho_s^2\nabla_\perp^2\hat{\varphi}$ is defined as the curl of $\mathbf{v}_E$, note $\hat{\varphi} = e\tilde{\phi}/T_e$. D and μ are coefficients of viscosity. $\sigma_\parallel$ denotes the parallel conductivity. In the absence of magnetic field curvature and cross field dissipation, equations are

reduced to the well-known Hasegawa-Wakatani model for resistive drift waves; In the collisionless limit, adiabatic electron response ($\hat{n} \sim \hat{\varphi}$) along the magnetic field lines, simplify the equations to the Hasegawa-Mima model .

Hasegawa-Wakatani model:

$$d_t \tilde{n} + B^{-1}\mathbf{b} \times \nabla \tilde{\phi} \cdot \nabla_r n_0 = n_0 \sigma_{\parallel} \left(e\tilde{\phi}/T_e - \tilde{n}/n_0 \right) \quad (1.17a)$$

$$d_t \varpi = \sigma_{\parallel} \left(e\tilde{\phi}/T_e - \tilde{n}/n_0 \right) + \mu \nabla_{\perp}^2 \varpi \quad (1.17b)$$

Hasegawa- Mima model ($\sigma_{\parallel} \to \infty,\ \mu \to 0$):

$$d_t (\varpi - \hat{\varphi} - \ln n_0) = 0 \quad (1.18)$$

Interchange turbulence

In the limit of resistivity, $\sigma_{\parallel} \to 0$, adiabatic electron response along the magnetic field lines become invalid. The separated ions and electrons due to gradient-*B* and curvature drifts can't be neutralized immediately. They raise a vertical electric field E_θ, and lead the plasma to drift outwards according to a radial $E_\theta \times B$ drift velocity. The physical picture of interchange motion is reviewed in the figure 1.8.

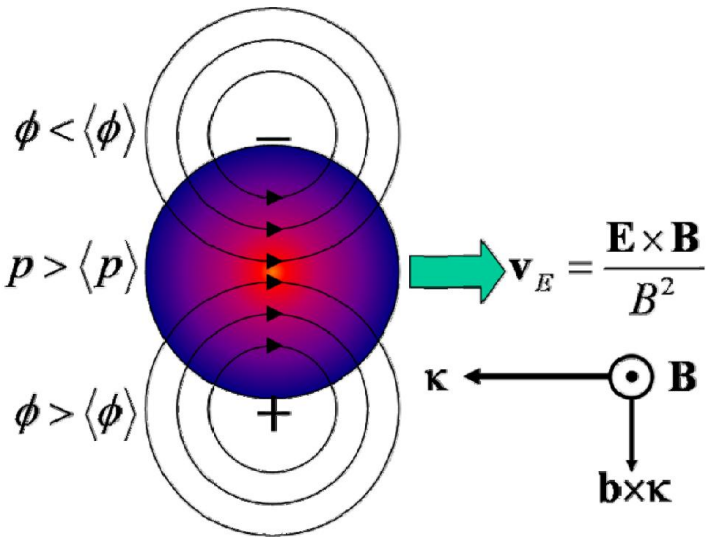

Figure 1.8. Illustration of the ideal interchange mechanism leading to radial motion of a localized density structure with an excess pressure *P* relative to the ambient plasma. The vertical polarization of electric charge and vorticity due to magnetic guiding center drifts leads to a radial electric drift at the center of the density structure. Redrawn from [29].

In the electron continuity equation (1.16a), the lowest-order cross-field plasma motion is dominated by the electric drift. Neglecting the first and second term on the right hand of electron continuity equation (1.16a), the simplest model for interchange motion is obtained as follows:

$$\begin{cases} \partial_t \hat{n} + c_s \rho_s \mathbf{b} \times \nabla \hat{\varphi} \cdot \nabla \ln n_0 = D \nabla_\perp^2 \tilde{n} & (1.19a) \\ \dfrac{1}{\omega_{ci}} \partial_t \nabla_\perp^2 \hat{\varphi} + \dfrac{2}{R} \mathbf{z} \cdot \nabla \hat{n} = \mu \nabla_\perp^2 \varpi & (1.19b) \end{cases}$$

To analysis the ideal interchange instability, we neglect the diffusion and viscosity coefficients in the equations, and make some assumptions:

$\partial_t \to -i\omega$, $\nabla_\perp \to ik_\perp$, for unstable mode $\omega = \omega_0 + i\gamma \approx i\gamma$, $\mathbf{z} \cdot \nabla \to ik_z$, $L_n = 1/\left|\partial_r \ln n_0\right| \sim \ell$

The relation between the density and potential perturbations can be found out as.

$$\begin{cases} \gamma \hat{n} = -\dfrac{c_s \rho_s}{\ell} i k_\perp \hat{\varphi} & (1.20a) \\ \dfrac{1}{\omega_{ci}} \gamma k_\perp^2 \hat{\varphi} = \dfrac{2}{R} i k_z \hat{n} & (1.20b) \end{cases}$$

Which could be further resolved as:

$$\gamma = c_s \sqrt{\frac{2}{R\ell} \frac{k_z}{k_\perp}} \qquad (1.21)$$

$$\frac{\hat{n}}{\hat{\varphi}} = -ik_\perp \rho_s \sqrt{\frac{R}{2\ell} \frac{k_\perp}{k_z}} \sim -i5k_\perp \rho_s \qquad (1.22)$$

As shown in equation (1.22), the potential fluctuations lags the density fluctuations by $\pi/2$ in the interchange motion of plasmas.

Turbulent transport

The random walk of particles is the fundamental assumption in the concept of classical transport. It argues that the particles diffusion coefficients scale as $D \sim (\Delta x)^2 / \tau$, where the Δx is the characteristic step size in the random walk and τ is the characteristic time between steps. In magnetic confined plasma, a charged particle

is bound to the magnetic field, but it has excursions from a flux surface to another on the order of its gyro radius. Coulomb collisions between charge particles dominate their cross-field random walk with gyro radius as step size and the time for a 90° collision as characteristic time. Neoclassical transport is classical transport including the effects of toroidal geometry of magnetic field. The neoclassical transport is still driven purely by coulomb collisions. However, the radial excursions of particles due to ∇B and curvature drifts is much larger than a gyro radius, leading to an increase in the collisional step size, and a corresponding increase in the transport coefficients.

In a low collisionality regime, the diffusion coefficient predicted neoclassical (NC) theory is estimated to be q^2 times higher than classical coefficient (CL).

$$D^{(NC)} \sim 4q^2 D^{(CL)}, \chi^{(NC)} \sim q^2 \chi^{(CL)} \quad (1.23)$$

Where the q is the safety factor, D is the particle diffusion coefficient, and χ denotes the thermal diffusion coefficient.

It has since long been observed that rates of transport are several orders of magnitude larger than those expected from both classical and neoclassical prediction. Over the past decades, turbulent transport has been identified to plays an important role in degrading the confinement of fusion devices. Understanding turbulent transport in magnetically confined plasmas is a subject of utmost importance for optimizing performance in the fusion devices.

Turbulence is often characterized by broad fluctuation spectra. It originates from the abundant microscopic instabilities and their interactions in the plasma. The turbulent fluctuations manifest themselves as eddies which could be thought of as local disturbances of random sizes and life times. Under certain circumstances, the motions of eddies are reordered to coherent structures through self-organization process. In general, the motions of turbulent eddies can lead to a robust transport, which significantly reduces the confinement time of fusion plasmas. The nonlinear particle flux due to plasma fluctuations is given by $\Gamma = \tilde{n}\tilde{v}$, where $\tilde{n}$ and $\tilde{v}$ are the fluctuating plasma density and fluid velocity respectively. For electrostatic low-frequency fluctuations, we may approximate the radial velocity $\tilde{v}_r$ by the radial component of that **E×B** drift to estimate the turbulence induced radial transport.

The turbulent density radial transport by plasma fluctuations reads in the frequency domain as:

$$\Gamma_r = \tilde{n}\tilde{v}_r = \frac{<\tilde{n}\tilde{E}_\theta>}{B_\phi} = \frac{2}{B_\phi}\int_0^\infty k_\theta(\omega)\tilde{n}(\omega)\tilde{\phi}(\omega)\gamma_{\tilde{n}\tilde{\phi}}(\omega)\sin\delta_{\tilde{n}\tilde{\phi}}(\omega)\,\mathrm{d}\omega \quad (1.24)$$

Here, the $\gamma_{\tilde{n}\tilde{\phi}}$ and $\delta_{\tilde{n}\tilde{\phi}}$ denote the coherence and cross-phase between the density fluctuations $\tilde{n}$ and plasma potential fluctuations $\tilde{\phi}$, respectively. k_θ is the transverse wave-number of the plasma potential fluctuations. For a instance, the ideal drift wave does not promote the particle transport, of which the cross-phase $\delta_{\tilde{n}\tilde{\phi}}$ is

zero. On the contrary, the interchange instability strongly enhances the particle transport due to the high $\delta_{\tilde{n}\tilde{\phi}}$.

Analogously, the cross-field energy flux, due to electrostatic turbulence can be expressed without species indices as $Q_r = \tilde{p}\tilde{v}_r$ in terms of fluctuations in pressure $\tilde{p}$.

$$Q_r = \tilde{p}\tilde{v}_r \approx \frac{3}{2}\times\frac{2}{B_\phi}[T_0\int_0^\infty k_\perp(\omega)\tilde{n}(\omega)\tilde{\phi}(\omega)\gamma_{\tilde{n}\tilde{\phi}}(\omega)\sin\delta_{\tilde{n}\tilde{\phi}}(\omega)\,\mathrm{d}\omega$$
$$+ n_0\int_0^\infty k_\perp(\omega)\tilde{T}(\omega)\tilde{\phi}(\omega)\gamma_{\tilde{T}\tilde{\phi}}(\omega)\sin\delta_{\tilde{T}\tilde{\phi}}(\omega)\,\mathrm{d}\omega] \quad (1.25)$$

where $\gamma_{\tilde{T}\tilde{\phi}}$ and $\delta_{\tilde{T}\tilde{\phi}}$ denote the coherence and cross-phase between the temperature fluctuations $\tilde{T}$ and plasma potential fluctuations $\tilde{\phi}$, respectively. n_0 and T_0 signify the local stationary density and temperature of plasma.

At the L-H transition, it is widely observed that the turbulence transport is significantly reduced in boundary plasma. A large number of works have been carried out in many tokamaks to understand the mechanism behind the reduction in turbulence transport occurring in H-mode. **E×B** velocity shear in the edge region is recognized to play an important role in suppressing turbulence. It is generally accepted that the spontaneous **E×B** shear flows can break up the plasma eddies in turbulence and abate the cross-field turbulence transport, because shear flows advect different parts of the eddy at different speeds.

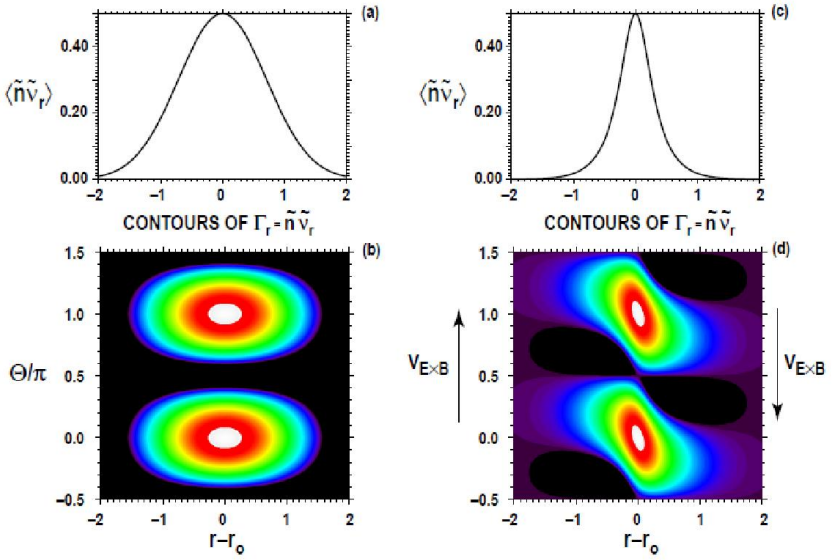

Figure 1.9. The radial fluctuation-driven particle flux $\Gamma_r = \tilde{n}\tilde{v}_r$. The (a) and (b) plots are for no shear in the average velocity while (c) and (d) are for the sheared case. The distortion of the eddies in (d) compared to (b) shows the effect of velocity shear on the radial flux [30].

Strength of the $\boldsymbol{E} \times \boldsymbol{B}$ shear effect is characterized by the shearing rate ω_s:

$$\omega_s = \left| \frac{dv_{E\times B}}{dr} \right| = \left| \frac{(RB_\theta)^2}{B} \frac{\partial}{\partial \psi} \frac{E_r}{RB_\theta} \right| \quad (1.26)$$

where R is the major radius, B_θ is the poloidal field, ψ is the poloidal flux and E_r is the radial electric field [31]. The turbulent eddy could be torn apart once the shearing rate ω_s exceed the decorrelation rate of the underlying turbulence $\omega_s \cdot \tau_e > 1$. Here, the τ_e is the life time of eddy. This criterion itself is essentially more complex in tokamaks [32] due to other physical effects (such as magnetic shear, etc). It has nevertheless been widely used as a rough estimation on the critical shear strength for the decorrelation of coherent structures in plasma turbulence.

As aforementioned, the regulation of turbulence transport can be achieved not only by the change in the turbulence intensity but also in the cross-phase and correlation time. Up to now, all three scenarios have been observed in the experiments. Although the amplitude of turbulent fluctuations are often detected to reduce at the L-H transitions in a wide range machines [33-39], there is growing evidence that the drop in the fluctuation level is not the only cause of the reduction in transport. The cross-phase of density and plasma potential have also been observed more strongly suppressed than turbulence intensity during L-H transitions in some tokamaks such as PBX-M [40] and DIII-D [41], as well as in the edge biasing experiments of RFX reversed field pinch[42] and TEXTOR-94[43]. It is still clouding on the issue of causality and the roles of the various terms in turbulence suppression during the L-H transitions.

1.4. Motivation

There is general consensus that both edge and SOL are of utmost importance to the overall performance of a working fusion machine. The plasma edge accompany with a transport barrier inside LCFS can effectively modify the turbulence transport. The SOL is, on the other hand, important for the exhaust of the lost plasma and impurity. The balanced plasma profile between edge and SOL plasma constitute the boundary condition for the core plasma confinement. Hence, the plasma transport in this region attracts a large attention.

Over several decades, the turbulence has been well identified as a major cause for the anomalous plasma transport. However, our understanding on the transport mechanism are still limited both in L-mode and H-mode regime. In recent years, with the application of fast cameras in fusion plasmas, as well as other diagnostics of spatial-temporal resolution such as Langmuir probes, it is generally clear that the

turbulent transport is mostly dominated by cross-field propagation of coherent structures in L-mode plasma. Such coherent structures are localized perpendicularly to magnetic field and extend along the magnetic field lines. The intermittent coherent structures contain a significant amount of particle and energy. They are ejected into the far SOL, which could lead to a erosion of the first wall.

In H-mode regime, a pronounced pedestal set up in the plasma edge. However, the sharp pressure gradient gives rise to a unstable structure name edge localized mode (ELM) with characteristic mode number (n~10-15). Using Langmuir probe and imaging measurements, it has been observed clearly that the ELM essentially composed a number of filamentary structures (ELM filaments), which extend along the magnetic field line. The periodic occurences of ELMs lead to the crash of edge pedestal and a robust transport of edge plasma into SOL divertor target, even the wall. The transient power load in the divertor target or the wall degrades the performance of fusion devices.

Some coherent modes are of great importance to the plasma edge plasma transport. Zonal flows (ZF) are time-varying poloidal E×B shear flows generated from turbulence, which are characterized by toroidally and poloidally symmetric potential structure with finite radial wavelength in tokamak plasmas. The radial shearing of zonal flows can break up the turbulence eddies and reduce the cross-field transport, thus it is of great interest in the fusion plasma, especially at the L-H transitions.

To contribute a better understanding on the plasma coherent structures, measurements using probe array were carried out in the boundary plasma of EAST tokamak. In the following chapter, the EAST tokamak and probe equipment system will be addressed. In the chapter three, the measurement in L-mode boundary plasma as well as a two-dimensional fluid code fluid simulation are documented, in which the statistical characterization of turbulence are presented. In chapter four, we present our observation associated with L-H transition in EAST tokamak. Chapter five shows the dynamic character and power deposition of different types of ELMs. In particular, the ability of current transport of ELM filaments are explored in Chapter five. A summary and outlook will be given in chapter six.

Chapter 2

Experimental Setup

2.1. EAST tokamak

The works presented in this thesis are mainly carried out in the Experimental Advanced Superconducting Tokamak (EAST). A brief introduction on EAST will be given in this section. EAST tokamak is located at the Institute of Plasma Physics, Chinese Academy of Sciences (ASIPP), in Hefei, China. It was constructed with plasma major radius R_0~1.88 m, minor radius a~0.45 m, and maximum toroidal field B_t=3.5T, plasma current I_p~1 MA. As the first fully superconducting fusion device with modern divertor configuration in the world, the EAST constitutes 16 toroidal magnetic field, 6 poloidal magnetic field and 6 central solenoid superconducting coils. With a flexible poloidal magnetic field control system, plasma elongation and triangularity could be accommodated easily [44]. The plasma discharge with different magnetic configurations, typically double null (DN) and upper/lower single null (USN/LSN) divertor configuration, could be achieved during one same shot. Auxiliary heating power on EAST is constituted by 6 MW lower hybrid current drive (LHCD) system, 12 WM ion cyclotron resonant heating (ICRH) system and 2-4 MW neutral Beam Injection (NBI) system [45]. To date, 60~70 plasma diagnostic systems have been set up on EAST. The diagnostics serve to provide physical information from the core plasma outwards to the SOL plasma, which greatly facilitate us to gain insight of plasma activities. The capabilities for scientific investigations on plasma physics has been significantly promoted in recent years.

Figure 2.1. General view of EAST tokamak.

The first plasma on EAST was obtained in 2006. The goal of EAST operation is to achieve long-pulse (60–1000 s) high-performance plasma. Up to now, EAST has achieved reproducible stationary H-mode plasmas of over 30 s and long-pulse diverted L-mode plasmas over 410 s in the latest 2012 experimental campaign, which set the new world records for the durations of H-mode and L-mode diverter discharge respectively [46]. The first H-mode plasma was produced by lower hybrid wave as the sole auxiliary power source on 7 November 2010.

2.2. Langmuir probe

Langmuir probe is a fundamental approach for the measurement on parameters such as plasma density, plasma potential, electron temperature of the boundary plasma. Probe tips are made from material of high conductivity, such as the graphite and tungsten, which are usually cast into cylinders with the size of several millimetres. The smaller size of probe tips can abate the disturbance of local plasmas and increase the spatial resolution of measurements. It works with high spatial-temporal resolution through the direct interaction with plasma as illustrated in figure 2.2.

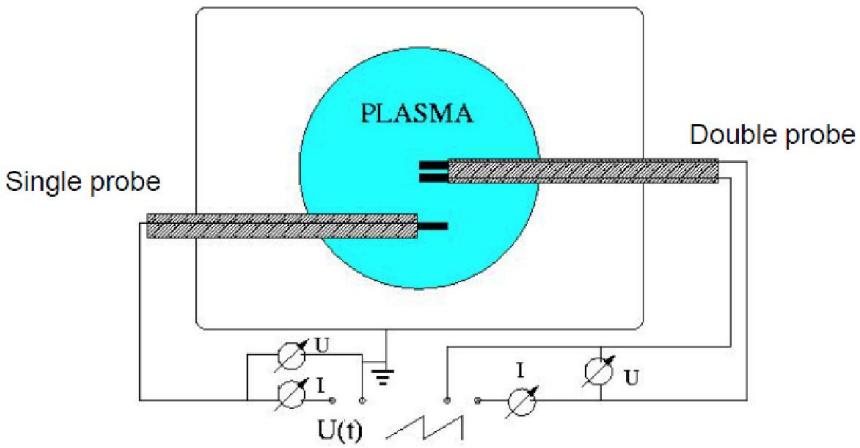

Figure 2.2. Diagrammatic sketch of probe measurements.

Up to now, there are only two diagnostics allowing the measurement of the plasma potential: heavy ion beam probe (HIBP) [47] and Langmuir Probe. Between them, the Langmuir probes are cheap and flexible to manufacture. Moreover, the dedicated arrangement of probe tips will enable us to obtain the crucial physical information. For instance, the radial electric field can be deduced from the difference of plasma potentials measured in two different radial locations. The correlation of plasma density fluctuations and potentials fluctuations can provide the insights on the turbulent particle transport (see equations (1.24,1.25)). By this fact, Langmuir probes are widely used in the investigations of SOL/Edge plasma. In this thesis, the

experimental results are mainly obtained via the measurements using probe diagnostic. Before we present the results in chapter 3-5, principle of Langmuir probe measurements are briefly reviewed in this section.

2.2.1 Single probe

Basic knowledge of Langmuir probe measurements has actually been mentioned in the context of SOL sheath. Assuming a isolated probe tip embedded in hot deuterium plasma, a plasma sheath are created at the surface of probe tip. The floating potential of probe tip is related to the plasma potential by the electron temperature as:

$$V_f = V_P - 3kT_e/e \qquad (2.1)$$

At the floating potential V_f, there is no current flow in to the surface of probe tips. For a complicate case, if the plasma tips are biased with imposed voltage V_{pr}, the balance between the plasma and probe tips will be interrupted, and the probe tips will immediately draw a current from collecting surplus ion flux or electron flux.

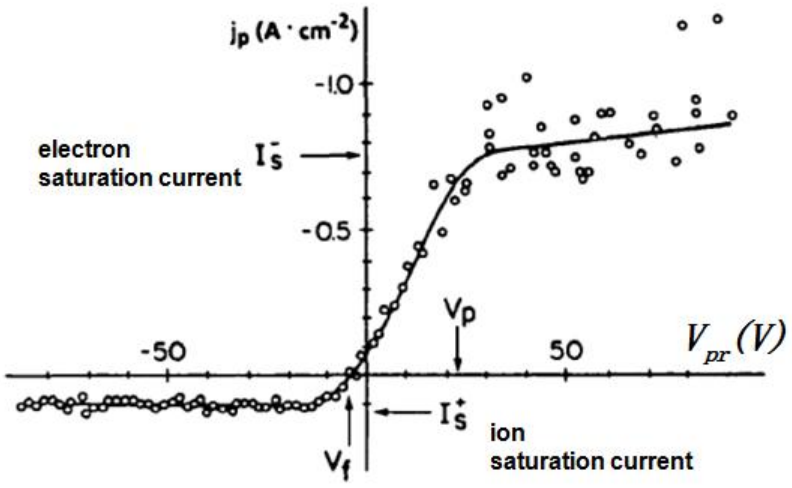

Figure 2.3. I-V characteristic curve of biased single Langmuir probe [48].

Scanning the biased voltage V_{pr} at the end of probe tips, one can obtain an I-V characteristic curve as indicated in the figure 2.3. At a voltage far below the floating potential, the electrons can't reach the probe tips due to a retarding electric force, and ion flux take over the solid surface of probe tips. At the plasma potential V_P, no electric field establish between the plasma and probe and thus no sheath arises at the probe. At a voltage far above the plasma potential, the probe tips readily collect the electrons, and the ions are repelled back to the plasma. The 'knee' of electron current

presents on a Langmuir probe I-V characteristic curve is identified as the plasma potential, since the collecting rate of electron flux changes abruptly there.

Electron current from a Maxwellian populations is expressed as:

$$I_e = -ne\sqrt{\frac{kT_e}{2\pi m_e}}e^{e(V_{pr}-V_p)/kT_e}\cdot A_{eff} = -I_s^- e^{e(V_{pr}-V_p)/kT_e}\cdot A_{eff} \quad (2.2)$$

According to the Bohm condition, ion ions enter the sheath edge with the ion acoustic velocity. The ion saturation current and electron saturation current from reads:

$$I_s^+ = nA_{eff}e\sqrt{k(ZT_e+T_i)/m_i} \qquad (2.3)$$

$$I_s^- = 1/4nA_{eff}e\sqrt{8kT_e/(\pi m_e)} \qquad (2.4)$$

Here, the A_{eff} denotes the effective collecting area for electrons and ions of probe tips. Z indicates the ion charge. n is the density at the edge of the probe sheath, which is half of the value upstream plasma density n_0 (see equation (1.13)). The electron current collected by probe tip at the plasma potential I_s^- is called electron saturation current. The electron saturation current is much larger than that of the ion saturation current due to the higher mobility of electrons.

Biased voltage between the V_f and V_P, the collect current by probe reads:

$$I = I_s^+ - I_s^- \exp[e(V_{pr}-V_p)/(kT_e)] \qquad (2.5)$$

It is the sum of the ion current and electron current at the floating potential V_f,

$$V_f = V_p - \frac{kT_e}{e}\ln R \qquad (2.6)$$

The quantity $R = \ln(I_s^-/I_s^+)$ is correlated to the ratio of the electron to the ion saturation currents. It is equal to the value Λ defined in the equation (1.12). When the ion saturation current balance with the electron saturation current, the R get towards to zero, and the plasma potential V_P can be directly inferred from V_f without the measurements of electron temperature T_e. Based on this conception, emissive probes [49, 50] are developed to measure the plasma potential directly by heating probe to strong thermionic electron emission, which can reduce the collected electron current and avoid the creation of a sheath in front of probe. Ball-pen probe [51, 52] is implemented to modify the collecting areas for electrons and ions, taking advantage of the fact that the Larmor radius of electrons and ions are rather different. The scientific philosophy of emissive probe and ball-pen probe is to balance the ion saturation current and electron saturation current at the solid surface of probe.

Figure 2.4 shows a floating potential signal measured by a cold Langmuir probe who was sent into the edge plasma. The radial position of probe are denoted by the dotted line in figure 2.4 (a) during a radial position-scan measurement. In the period 3.54s-3.6s, probe stay put at 3 cm inside the LCFS. A floating potential tip becomes emissive from the time 5.37s due to overheating from hot edge plasma on EAST. Plasma potential are determined by a triple probe when the probe tip keeps cold, whereas the triple probe measurement will be introduced in the following section 2.23. As observed in figure 2.4 (b), the potential of emissive probe is close to the plasma potential deduced from a standard Langmuir probe. Emissive probes are still under development on EAST. Our experimental results discussed in this thesis are mainly obtained by Langmuir probe measurements.

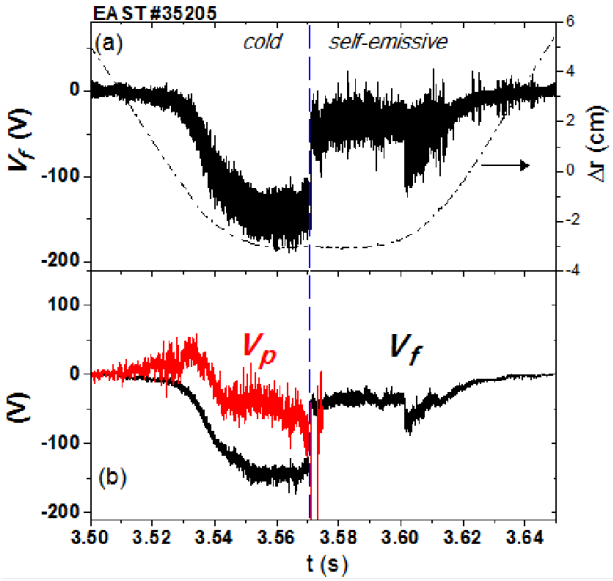

Figure 2.4. (a) Floating potential V_f measured by a cold Langmuir probe who becomes emissive from the time 5.37s (indicated by the blue dashed line) due to a overheat, and the radial location △r of probe with respect to the LCFS during a radial position-scan measurement, (b) The plasma potential V_P (3.5s-3.57s) evaluated from a triple probe and the low frequency component (<10*k*Hz) of floating potential V_f.

2.2.2 Double probe

Figure **2.5** shows the circuit of a double probe array, where a scan voltage V_D is biased voltage between a pair of identical floating probe tips. The potential of positively biased is V_+, and the potential of negatively biased is V- , i.e. V_D=V_+ - V-. The current flowing in the tips are noted as I_D here, which is same in the two tips.

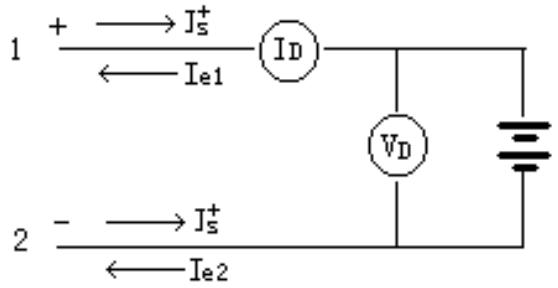

Figure 2.5. Circuit diagram a double probe array.

The current I_D is composed of ion saturation current and electron current.

$$I_D = I_{e1} - I_s^+ = I_s^+ - I_{e2} \qquad (2.7)$$

The electron current vary with the biased probe potential V_+ and V_-,

$$I_{e1} = I_s^- \exp[e(V_+ - V_p)/k_b T_e] \qquad (2.8)$$

$$I_{e2} = I_s^- \exp[e(V_- - V_p)/k_b T_e] \qquad (2.9)$$

$$I_{e1}/I_{e2} = \exp\{e[(V_+ - V_-) - (V_p - V_p)]/(k_b T_e)\} = \exp[eV_D/(k_b T_e)] \qquad (2.10)$$

$$(I_D + I_s^+)/(I_s^+ - I_D) = \exp[eV_D/(k_b T_e)] \qquad (2.11)$$

the relationship between V_D and I_D is obtained：

$$I_D = -I_s^+ \tan[eV_D/(2k_b T_e)] \qquad (2.12)$$

The derivative of I_D with V_D at the value V_D=0 gives the information of electron temperature.

$$dI_D/dV_D|_{V_D=0} = eI_s^+/(2k_b T_e) \qquad (2.13)$$

With the value of electron temperature T_e , plasma density n_0 can be deduced from ion saturation current as:

$$n_0 = I_s^+/(0.5 A_{eff} e\sqrt{k(T_e + T_i)/m_i}) \qquad (2.14)$$

2.2.3 Triple probe

To determine the plasma parameter with the single probe or double probe, one needs to get the characteristic I-V curve beforehand. The biased voltage on probe is difficult to be implemented with high scanning frequency. Hence, the resolution of measurements by single probe and double probe is limited. The triple probe is widely adopted in the boundary plasma measurements, as it works only with a fixed biased voltage. It combines a single floating potential probe V_f and a pair of double probe which is biased to the ion saturation regime.

$$I_{e1} + I_{e2} = 2I_s^+ \tag{2.15}$$

$$I_{e2} / I_{e1} = \exp[-eV_D / (kT_e)] \tag{2.16}$$

$$I_s^+ = I_s^- \exp[e(V_f - V_p) / (kT_e)] \tag{2.17}$$

when $V_D >> k_b T_e / e$， they give：

$$\exp[-eV_D / (k_b T_e)] \cong 0 \tag{2.18}$$

$$I_{e1} \approx 2I_s^+ \tag{2.19}$$

thus,

$$I_s^- \exp[e(V_+ - V_p) / (k_b T_e)] \cong 2I_s^- \exp[e(V_f - V_p) / (k_b T_e)] \tag{2.20}$$

$$e(V_+ - V_f) / (k_b T_e) \cong \ln 2 \tag{2.21}$$

The electron temperature T_e is expressed in the unite of eV:

$$T_e \cong (V_+ - V_f) / \ln 2 \tag{2.22}$$

Therefore, the electron temperature can be obtained by the direct measurements of potential of positive biased probe tips and the floating potential. With the electron temperature, we further derive the plasma density and plasma potential.

$$n_e = I_s^+ / [0.5 A_{eff} e\sqrt{2eT_e / m_i}] \tag{2.23}$$

$$V_p = V_f + \mu T_e \tag{2.24}$$

Here, the μ=$1/2\ln[m_i / 2\pi m_e]$.

2.2.4 Mach Probe

The Mach probe specifically allows the measures of the plasma flow velocity qualified by the Mach number. The Mach number M is defined as the ratio of plasma flow velocity u_0 and the ions sound speed C_s, i.e. $M= u_0/C_s$. As shown in figure 2.6, Mach probe usually consists of the two identical Langmuir probe pins, physically separated by an insulator such as boron nitride ceramics, which ensure the two pins do not communicate with each other. The basic philosophy of mach probe measurement is to deduce plasma flow velocity from observations of the upstream to downstream asymmetry of ion collection. Some modeling efforts [53-58] are made to fill the gap on the mach probe theory. However, the scaling of Mach number with plasma parameter is still not well understood yet.

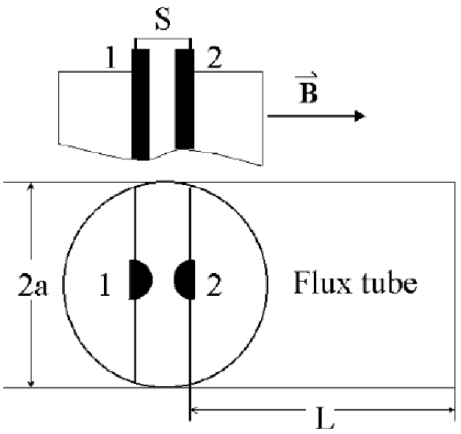

Figure 2.6. Construction of Mach probe array.

Assuming there is a Maxwellian population of ions with a superimposed drift u_0 along the magnetic field line in tokamak, and the ion temperature is T_i. The ion density is n_0 and the mass of ion is m_i. The velocity distribution function $f(v)$ of ions is written as

$$f(v) = n_0\sqrt{\frac{m_i}{2\pi kT_i}}\exp(-\frac{(v-u_0^2)}{2m_i kT_i}) \quad (2.25)$$

By integrating $v{\cdot}f(v)$ over the velocity space, the upstream ion currents J_u and downstream ion currents J_d are obtained. An emperical relationship beteween parallel Mach number $M_{//}$ and parallel ion velocity $u_{//}$ is suggested by Hutchinson [53] in magnetized plasmas.

$$M_{//} = u_{//}/c_s \approx 0.4\ln(\frac{J_u}{J_d}) \qquad (2.26)$$

The theory of Mach probe measurement is very complicated by the a variety of factors such as the strength of magnetic field, plasma parameter, flow direction relative to the magnetic field. No satisfactory model has been developed to cover the different physical situations.

2.2.5 Langmuir-Mach probe on EAST

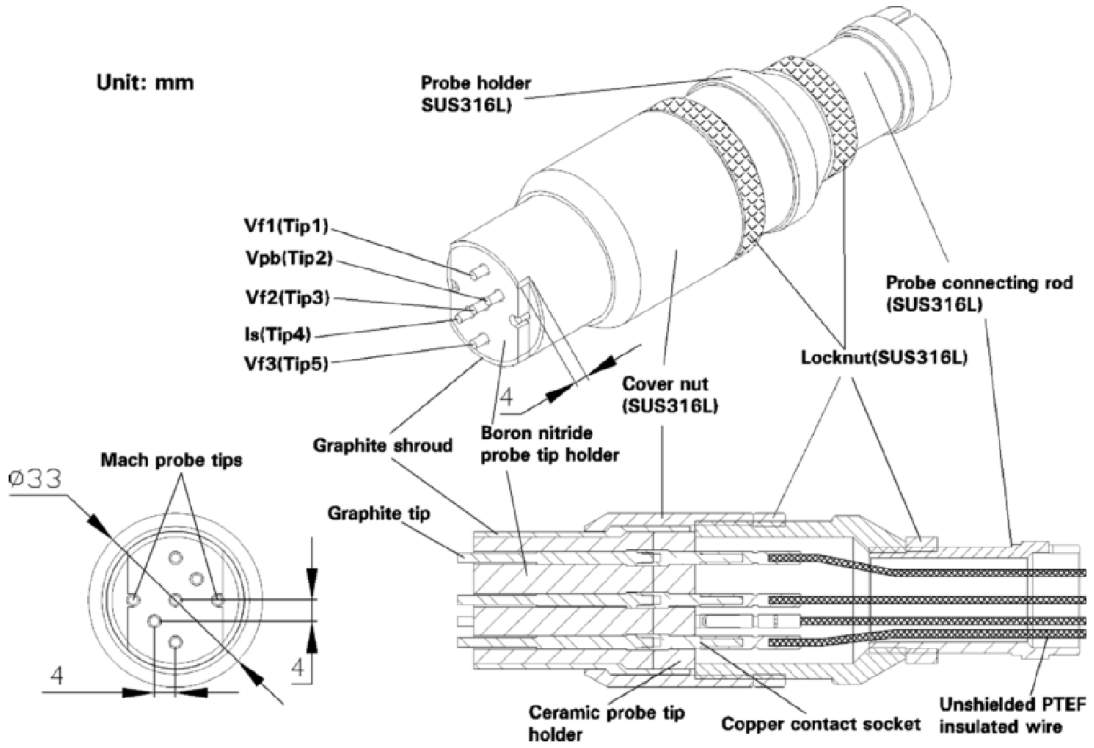

Figure 2.7. The prototype probe head with seven graphite tips on the EAST tokamak. The probe tips are 1.8 mm in diameter and 2 mm above the probe holder surface. Two of the tips are for a Mach probe on the opposite sides of probe head, and the rest five tips are for a triple probe [59].

As shown in figure 2.7, a combined Langmuir-Mach probe are used to provide simultaneous measurements of plasma profiles and ion parallel flows on EAST. The upstream and downstream graphite electrodes, which are embedded in a boron nitride ceramic body, sampled plasma from opposite directions along the same field line, forming a 'Mach probe pair'. The parallel Mach number is estimated from the ratio of ion saturation current signals, $M_{//} = 0.4\ ln\ (I_{up}/I_{down})$. The other five tips on top of the probe head were operated as triple probe, allowing simultaneous measurements of electron density n_e, electron temperature T_e, and plasma potential V_P , where I_s denotes ion saturation current measured by Tip 4. Floating potential V_f is measured by Tip1, Tip3 and Tip5, and V_{pb} is the potential on Tip2 which was positively biased at 250 V. The parallel flow velocity is then estimated as $V_{//} = M_{//}C_s$, where C_s is ion sound speed. All the probe tips are made of graphite with 1.8 mm in diameter and 2 mm in length. The probe data are simultaneously sampled at a rate of 2 MHz with 12-bit resolution using a multichannel digitizer. The high temporal and spatial resolution of probe measurements enables us to determine a equilibrium plasma profile and turbulent plasma fluctuations.

2.3. Probe arrangement on EAST

2.3.1 Reciprocating probe

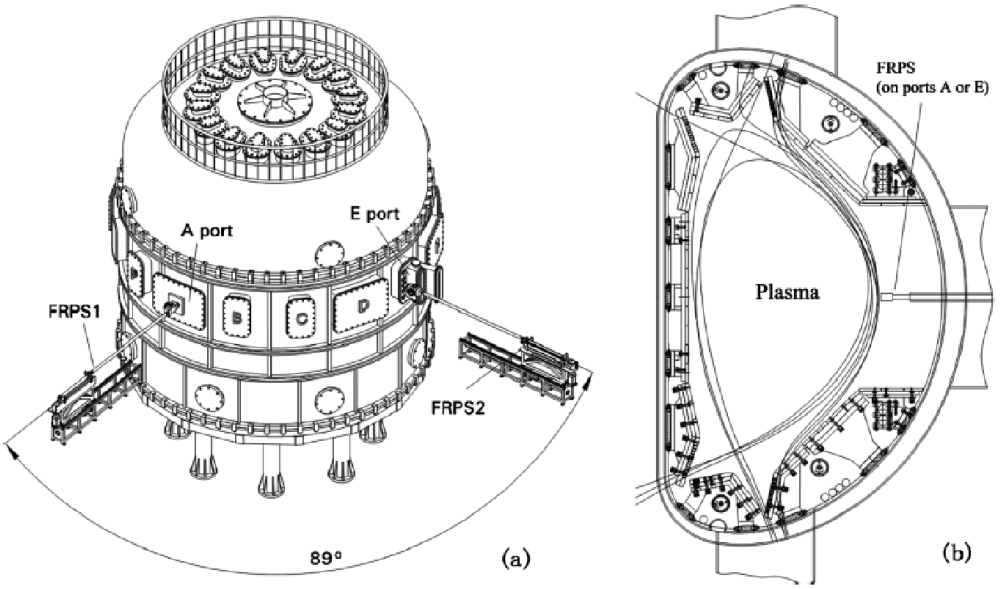

Figure 2.8. (a) Two FRPSs are installed in the horizontal ports A and E on EAST, separated 89° from each other in the toroidal direction. (b) The poloidal cross-section shows the probe on the out midplane of EAST.

Two fast reciprocating probe system (FRPS) are equipped respectively on diagnostic port A and diagnostic port E at the outer midplane of the EAST tokamak (see figure 2.8). The probe array can be translated by FRPS from the position behind the limiter towards the SOL plasma even edge plasma during the discharge. The FRPS can accomplish several reciprocating movements within one discharge of several seconds. The scanning range of FRPS is up to 50 cm, and the maximum acceleration and deceleration of probe shaft is about 30 m/s^2. Both the scanning range and velocities can be adjusted according to the experimental requirements. During one reciprocating movement, the radial profile of plasma parameter can be obtained by the data acquisition made along the radial radius. The feature of local plasma turbulent fluctuations can be captured by the probe measurements. These two FRPS are of same poloidal position, but separated by 89° in toroidal direction. Two probes could be located to a same radial location to perform long range cross-correlation measurements of turbulent fluctuations in one same magnetic flux surface. This facilitates the investigations of large scale coherent structures organized in tokamak. To minimize the probe interruption on background plasma, the probe head can be parked in one appointed radial location for several milliseconds. However, the long term duration of the probe stay will lead to overheat of the probe tips, and the sputtering of probe material will pollute the confined plasma.

2.3.2 Fixed divertor probe

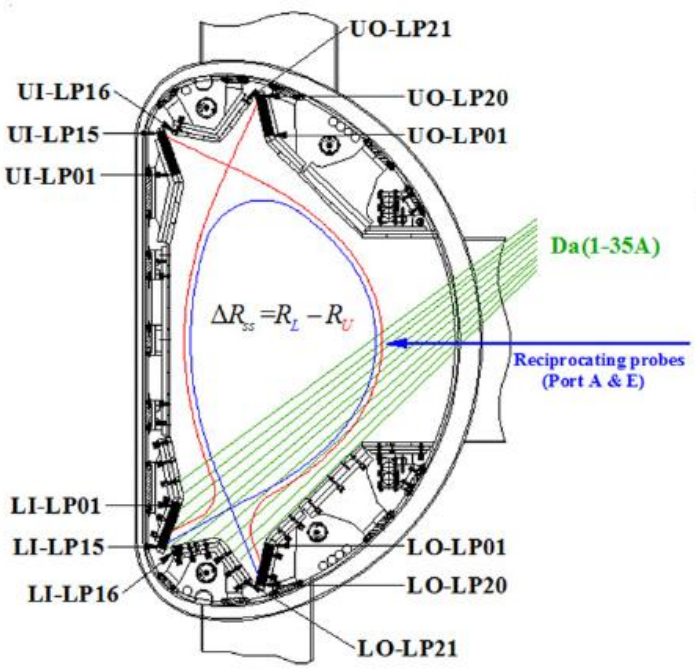

Figure 2.9. Poloidal layout of divertor triple Langmuir probes and Dα arrays viewing the lower target plates on EAST. UO(I)—upper outboard (inboard) divertor; LO(I)—lower outboard (inboard) divertor. The outer mid-plane reciprocating probes and a typical LSN divertor configuration with $\triangle R_{ss} < 0$ are also shown [60] .

There are 74 groups of graphite Langmuir triple probes, 222 pins in total embedded in the divertor targets (see figure 2.9). Specifically, 15 groups of probes are installed in the upper inner target (UI01-UI15) and lower inner divertor target (LI01-LI15) respectively; 20 groups of probes are installed in the upper outer target (UO01-UO15) and lower outer divertor target (LO01-LO20) respectively; LI16, UI16, LO21, UO21 is mounted at the dome. The pins are distributed in port D-G toroidally. The electron temperature T_e, and electron density n_e can be measured at the four divertor targets with a spatial resolution of 15mm at inner divertor targets and 10mm at outer divertor targets, respectively. The arrangement of divertor probe on EAST offers abilities for the study of divertor asymmetry in different plasma configurations. The measured parameters could also be mapped to the mid-plane using the EFIT magnetic equilibrium to compare with the profile obtained in the outer midplane using reciprocating probe. The time resolution of divertor probe measurements is about 0.2 ms, which is constrained by the sampling rate of data acquisition system. An array of 35-channal D_α system is used to view the inner target and dome from the outer board midplane. The divertor system is a very favorable diagnostic for the investigation of the particle flux and power load in the SOL region.

2.4. Magnetic probe

Magnetic probe is a prime candidate diagnostic on the magnetic fluctuations, specifically magnetohydrodynamic (MHD) modes in fusion plasma. As depicted in figure **2.10**, magnetic coils simply consist of a loop of wire in number of turns. Once the magnetic coils subject to a time varying magnetic flux, it will induce a voltage across the loop according to Faraday's law (see equation 2.27).

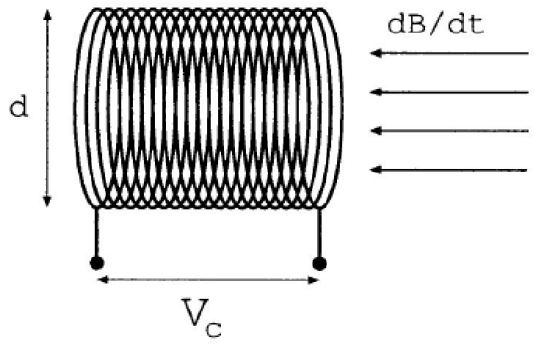

Figure 2.10. Wound magnetic coils to detect the magnetic variation.

$$V_c = -\frac{d\Phi}{dt} = -NA\frac{dB}{dt} \quad (2.27)$$

where Φ is the magnetic flux through the loop or coils, *B* is the magnetic field that lies along the axis of the coils and *A* is the effective area over the measured magnetic flux. The magnetic perturbations *B* can be obtained by integrating the *dB/dt* with time. The magnetic probe are not able to diagnostic the stationary magnetic field.

To obtain a large inductive signal, one has to increase the collecting area *A* or the number of turns *N*. However, the enlargement in volume will lead to a degradation on the spatial resolution of magnetic probe. On the other hand, sensitivity and response of magnetic probe, are determined by the probe's internal resistance, internal capacitance, self-inductance and so on. The increasing in turns will enhance the inductance *L*. The cut off frequency f_{co} of the coils of the coil vary inversely with the inductance *L*.

$$f_{co} = \frac{Z_0}{2\pi L} \quad (2.28)$$

Here, the Z_0 is load impedance of connecting sampling circuit. Therefore, a compromise point has to be accommodated carefully between the spatial resolution and time resolution. The magnetic coils is difficult to be implemented in the high temperature plasma, the heat load on the magnetic probe will melt the wires of the magnetic coils.

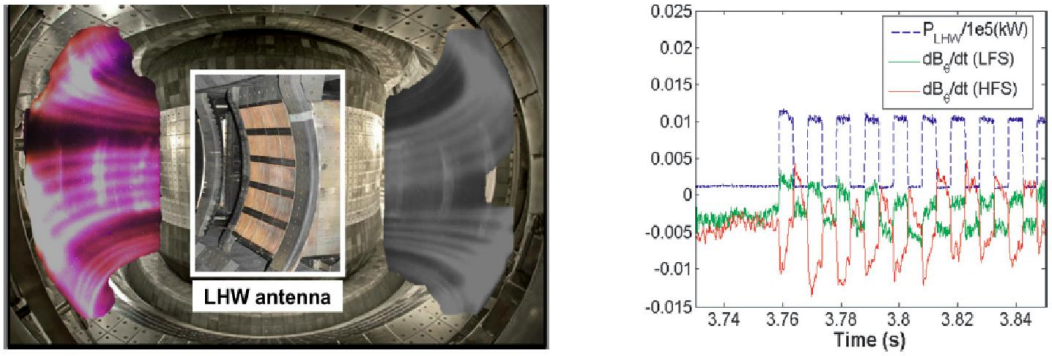

Figure 2.11. left panel: fast camera observation of five non-rotating helical radiating belts induced by LHCD driving currents in the SOL. right panel: magnetic fluctuations measured by pick-up magnetic coils during the LHCD modulations.

On EAST, magnetic probes are installed on the chamber wall both on high field side (HFS) and low field side (LFS), which is used to diagnostic the dynamic of plasma and feedback the information for the plasma control. The inductive loops are wound with enamel nonconductor coated copper wires 1 mm in diameter. The number of turns in the probe coils ranged from 20 to 60 in EAST. The calibrated average collection area of the magnetic probes is about 0.17 mm^2 . The cut off frequency f_{co} of magnetic coils is above 100kHz. To draw an example of magnetic probe implementation on EAST here, figure 2.11 (right panel) shows the magnetic perturbations induced by LHCD modulation. It is observed that the injection of LHCD drives five helical filamentary plasma structures in the SOL, which are clearly visible in the fast cameral on EAST. Meanwhile, strong poloidal magnetic perturbations dB_θ/dt are detected by the magnetic coils both in HFS and LFS during the LHCD modulation. It was found that the excitation of such global magnetic fluctuations strongly correlate with the appearance of filamentary structures. These observations provide a strong evidence that the helical plasma filaments driven by LHCD carry applicable current in the SOL of EAST.

2.5. GPI diagnostic

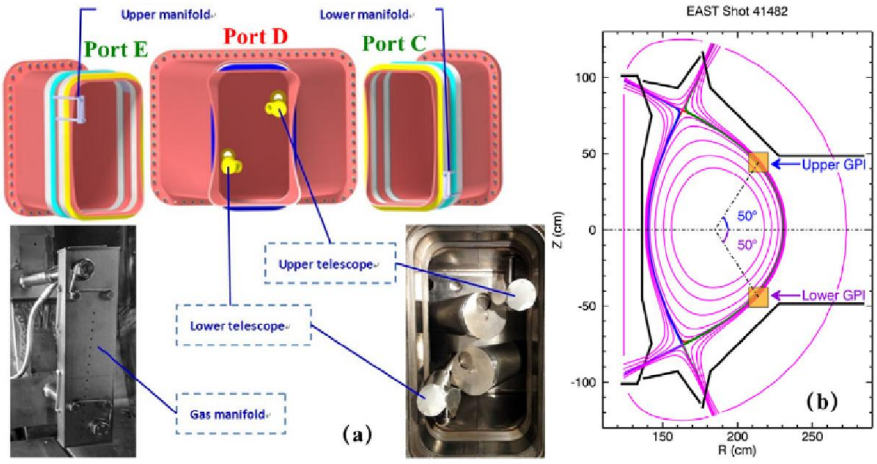

Figure 2.12. (a) Illustration of two GPI diagnostic systems on EAST. Gas manifold of upper GPI is located at top left side of port E and that of lower GPI is located at bottom right side of port C. The two telescopes are located in the center at port D. (b) Cross section of two GPI system poloidally separated by ~100° [61].

Most of our work in this thesis is carried out with probe measurements on EAST. A new dual gas puff imaging (GPI) system developed recently are briefly reviewed here. As shown in figure 2.12, two views of GPI are respectively directed to two domains on the outer board mid-plane. They are up-down symmetric with respect to the mid-plane and separated toroidally by 66.6°, poloidally by 100°. The working gas, deuterium or helium, is puffed into the objective plasma during the measurements. The ionized deuterium/helium in plasma radiate a atomic D_α line at 656.2 nm or HeI line at 587.6 nm. Light emission from the gas cloud is captured by two in-vessel telescopes installed on D port, and ultimately visualized by fast cameras outside of the vessel. The intensity of light emission I is correlated with the local electron density n_e and temperature T_e as:

$$I(photons/m^3) = n_0 f(n_e, T_e) A \qquad (2.29)$$

Here, n_0 is the local neutral density, A is the radiative decay rate for the observed line. $f(n_e, T_e)$ gives the density ratio of neutrals radiating D_α line at 656.2 nm or HeI line 587.6 nm, which depends on the local plasma density and temperature. The radial versus poloidal viewing area at the gas cloud plane is a 130×130 mm square, with 65 mm outside the LCFS and 65 mm inside the LCFS. The feature of local turbulent fluctuations in the boundary plasma is deduced from the distribution of light intensity in this 2D visual field. The spatial resolution of the optical system is 2 mm at the gas cloud plane, and the temporal resolution is 2.56 μs per frame and the exposure time is 2.156 μs. GPI is an effective diagnostic for tracing the dynamics of coherent plasma structures.

Chapter 3

Characteristics of turbulent fluctuations in L-mode plasma

3.1. Coherent turbulent structures

The transport of particles and energy in the plasma edge and SOL of todays magnetic-fusion devices in L-mode confinement regime is mostly non-diffusive and occurs in the form of the intermittent convection of coherent meso-scale plasma structures [62-65]. Such coherent plasma structures, extend along the magnetic field and localize in the perpendicular plane, known as blobs or filaments. They carry particles, momentum and energy into the far-SOL with their outward propagation. The associated intermittent transport has potentially significant impact on the particle recycling and power load on divertor plates, and it leads to high levels of impurity sputtering and erosion of the first wall.

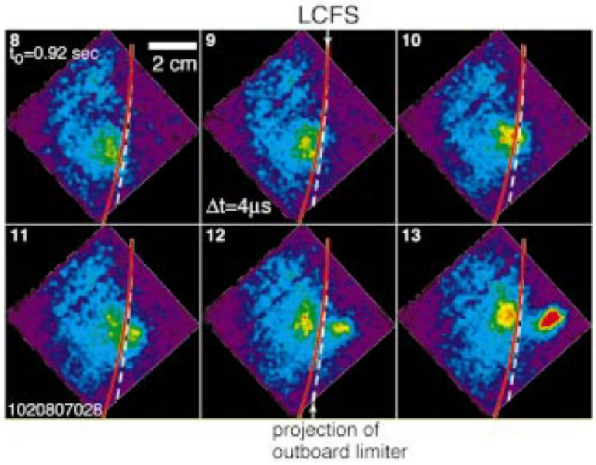

Figure 3.1. Sequences of six experimental images, showing space and time evolution of a blob originating inside the LCFS at the outboard SOL. The red line is the LCFS; the black–white line is the toroidal projection of the outboard limiter [66].

For last decades, blobs/filaments have been extensively investigated by Langmuir probe [67-69], gas puff imaging [66, 70, 71], and beam-emission spectroscopy measurements [72] in fusion plasma. Blobs/filaments manifest themselves as large amplitude events in multipoint probe or optical measurements. Figure 3.1 shows an instance of blob structures identified by the GPI diagnostic at the boundary of Alcator C-Mod [66]. The blob as a coherent structure propagates from the region inside the separatrix to the low-density region near the wall. Due to the emergence of coherent structures, the statistics of background turbulent density fluctuations are characterized in non-Gaussian probability distribution function (PDF) with positive skewness and kurtosis. Statistical features of blobs appear to be universal on many magnetized fusion device, regardless of the magnetic topology

(tokamaks, stellarators, reversed field pinches) or geometrical configuration (toroidal or linear devices) [73]. The remarkable self-similarity of turbulent intermittency suggests they possibly have the same nonlinear origin.

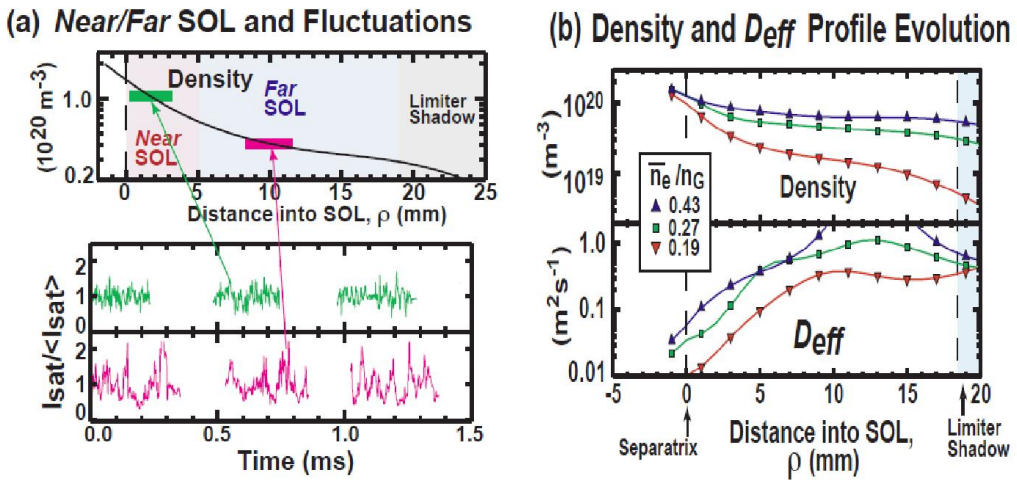

Figure 3.2. (a) near and far SOL zones with change in fluctuation character, (b) strong variation in effective cross-field particle diffusivity D_{eff} across the SOL and flattening of the SOL with increasing core density [74].

More importantly, the propagation of blobs/filaments with intensified plasma density and temperature is found to underlie a intermittent, convective particle transport in a location isolated from their birthplace. The cross-filed transport can compete or even dominate over the fast parallel plasma transport aiming at the divertor targets. This leads to the broad density and temperature profiles and enhanced density fluctuation levels, which has been observed in the SOL plasma of many devices [75-77]. A typical example on Alcator C-Mod is quoted here in the figure 3.2, showing that fluctuation level of ion saturation current or density enhanced outwards in the SOL. It is generally recognized that the blobs are responsible for large fractions of the cross-field particle and heat transport. The intermittent transport by blobs play a key role in setting the SOL width and impacting the discharge density limit. Hence, understanding the nature of the blob relevant transport is a crucial issue in fusion plasmas.

After the blobs are identified, their isolated structures could be extracted or traced in the background turbulence. Blobs show a mono-polar density with dipolar potential, moving both in radial and azimuthal direction. In the past years, the understanding on the ballistic dynamics of blobs has been significantly improved. A first qualitative model on the radial convective movements of blobs has been proposed by Krasheninnikov [62]. It suggested that the cross-field propagation of blobs is driven by the polarization-induced radial **E×B** drift which is associated with

charge separation by the grad-B drift and curvature drift in tokamak. The radial radial **E×B** convective velocity can be affected by the plasma resistivity. This qualitative picture has been supported by a great deal of numerical modeling and experimental observations [78-82].

Up to now, the generation mechanism of blobs is not universally understood in different devices. In the basic toroidal experiment TORPEX, without closed field lines, the interchange instability is found to be responsible for blob generation [83], while in the linear experiment VINETA, the blobs emerge out of quasi-coherent drift waves [84]. In the toroidally confined low-temperature plasma of TJ-K [85], blobs have been shown to be generated from drift-wave turbulence in the confinement region due to a change of turbulent characteristics across the separatrix. Using a fast camera on the high-temperature plasma of the NSTX tokamak, a blob birth zone is identified in the SOL around the steepest normalized pressure gradient [86]. Langmuir probe array measurements on JET [87], ASDEX Upgrade [88], HL-2A [89], indicate that blobs are generated inside the LCFS. GPI imaging on Alcator C-Mod clearly shows the blobs originate from a region inside the LCFS and propagate outwards into the far-SOL plasma [66]. Recently, the so-called cooperative elliptic instability is found to be responsible to the generation blobs using the fast camera diagnostic in the linear device CSDX [90]. The two-dimensional interchange turbulence code ESEL (Edge-SOL Electrostatic) has been developed to describe the generation process of intermittent events in the SOL plasma [65, 81]. It has demonstrated good agreement of the statistical characteristics of SOL turbulence comparing probe measurement on TCV and MAST to ESEL simulation [77, 82, 91].

To gain a better understanding on characteristics of boundary plasma, we carried out measurements in the boundary plasma using multi-pins Langmuir probes. The probes were inserted radially through the LCFS in Ohmic discharges at the outboard mid-plane on EAST. The statistic characteristics of boundary plasma turbulence are investigated in this chapter. Moreover, two–dimensional interchange turbulence simulations have been performed with the ESEL code in the SOL domain at the outer mid-plane on EAST. Good agreement is found for many aspects of experimental measurements and simulation outputs. The experimental results from EAST confirm the earlier observations from other toroidal magnetic confined devices [87-89].

3.2. Investigated plasma parameters

The experiments were performed in Deuterium Ohmic plasma on EAST with plasma current I_p=250kA, toriodal field B_0=1.8T on the magnetic axis, and line-averaged electron density n_{el} =1.5×10^{19} m^{-3}, more detailed information can be found in figure 3.3. The safety factor at the plasma edge is very high, q_{95} ~ 10, due to the low plasma current. The Ohmic heating power is ~200 kW. In such low power discharges, graphite probes can provide reliable measurements up to 4 cm in the confined region and in the SOL where electron temperature is usually less than 60 eV. The experiments are conduced in 'normal *B*' direction which is defined as B_t clockwise (***B***×∇*B* pointing down) and I_p counterclockwise, viewed from the top. The data presented below were obtained in double null（DN）magnetic configuration. The poloidal cross-section calculated by EFIT is shown in figure 3.4 (*a*).

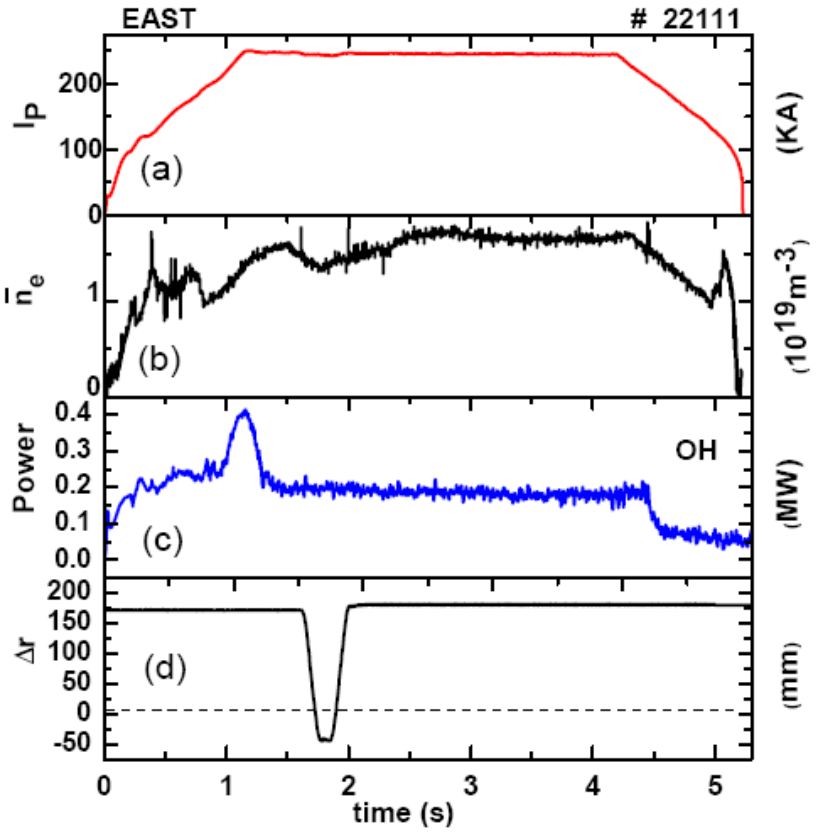

Figure 3.3. The discharge information for the experiment. (a) the plasma current. (b) the line averaged density (c) the input Ohmic heating power (d) the relative position of probe head with respect to the LCFS (dash line)

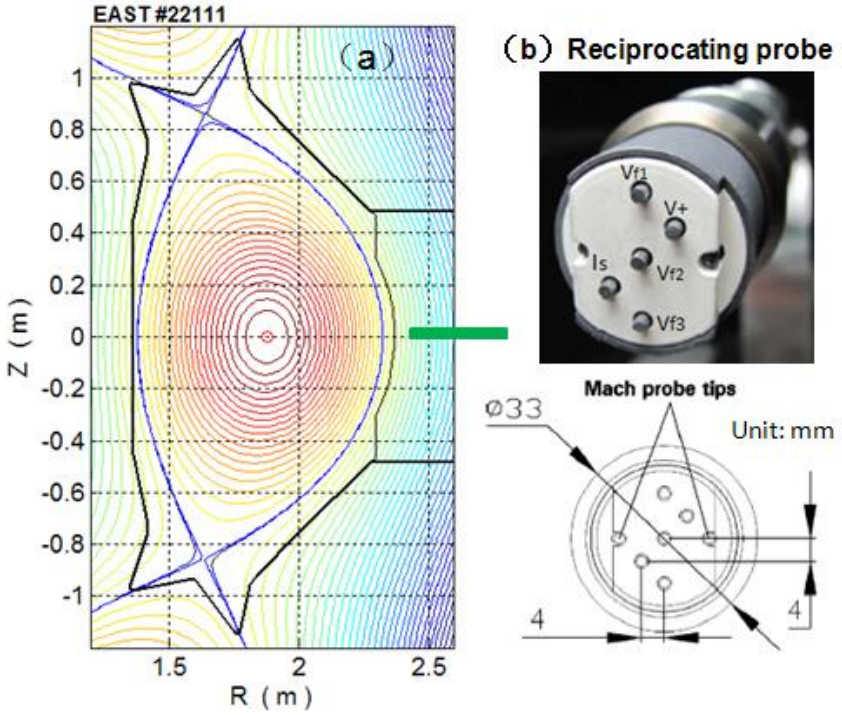

Figure 3.4. (a) Magnetic configuration of the discharge calculated by EFIT (b) Probe head arrangement in the EAST experiment. The probe tips are 1.8 mm in diameter and 2 mm above the probe holder surface.

Measurements of the edge plasma parameters are performed using reciprocating Langmuir probe at the outer mid-plane. The probe scans horizontally from the outside wall to the edge plasma. It is driven by an AC servo motor system capable of scanning a range of 50 cm at a speed up to 2 m/s. A typical position trace is shown in figure 3.3 (d). Here, △r is the radial distance with respect to the separatrix. Radial profiles of the plasma parameters measured by the probe are obtained by extracting the low frequency (<1kHz) component of data acquired in a probe stroke. To facilitate the investigation of the long-range correlations of edge turbulence, two identical probe head were installed in two reciprocating probe systems equipped at port A and port E, which separated toroidally by 89° on EAST. The two probe head were kept synchronously in the same radial position during the reciprocating measurements. The Probe array is divided into two groups according to their function. One group consists of five separated tips in the middle part of the probe array. They can detect floating potential V_f, ion saturation current I_s, which is proportional to local plasma density n_e, $I_s = 1/2 A_{eff}\, en_e C_s = 1/2 A_{eff}\, en_e (kT_e + kT_i/m_i)^{\frac{1}{2}}$, ($T_e$ and T_i are the electron and ion temperatures respectively, A_{eff} is the effective receiving area of tips and n_e is the electron density). The plasma temperature is estimated using $T_e \approx T_i \approx (V_+ - V_f)/\ln 2$, where V_+ is the floating potential of the biased double probe and V_f is taken as the average of V_{f1} and V_{f2} avoiding poloidal phase delay error. n_e is estimated directly

from the ion saturation current neglecting the electron temperature fluctuation effect, and the plasma potential is calculated as $V_p \approx 3T_e + V_f$, with $3T_e$ being the sheath potential drop for Deuterium plasmas. E_θ is deduced from the floating potentials measured with two tips separated by d_θ in the poloidal direction assuming that the temperatures and the sheath drops are identical in both the probe tips and that the plasma structures are larger than the separation between the probes (i.e. $E_{\theta 12} = \left(V_{f1} - V_{f2}\right)/d_\theta$ $E_{\theta 23} = \left(V_{f2} - V_{f3}\right)/d_\theta$) . Accordingly, the arrangement of the tips also allows the simultaneous measurements of the turbulent (electrostatic) particle flux Γ_r, heat flux Q_r, which reads respectively:

$$\Gamma_r = \frac{1}{B_\varphi} < n_e E_{\theta 23} > ; \quad Q_r = \frac{3}{2B_\varphi} < n_e T_e E_\theta > \qquad (3.1)$$

Here, $E_{\theta 23}$ (aligned with the I_s tip) is used to correlate with I_s to obtain the turbulent particle flux and convective heat flux, while $E_{\theta 12}$ (aligned with the T_e (V_+) tip) is used to correlate with T_e for the conductive heat flux measurements.

The other group of these tips located on the both sides of a ceramics podium constitutes the field aligned Mach probe pairs, which serves to observe the main ion motion in the boundary plasma. The measurements of the parallel SOL flow will be discussed in the end if this chapter. The experimental results present here are mainly from the measurements from E port, except for the long-range correlation analysis. The fluctuation data was digitized at 2 MHz with 12-bit resolution using a multi-channel digitizer.

The standard Langmuir probe technique and theory are challenged by several recent works. The measurements in the edge plasma of the CASTOR tokamak showed that effect of sheath expansion in the front of Langmuir probe can lead to an overestimation of plasma density n and electron temperature T_e [92]. Particularly, the assumption $T_e = T_i$ is rather extreme in the theory of Langmuir probe, since ions are observed naturally hotter than electrons in the SOL [93]. The detailed validity of the Langmuir probe technique and theory is complicated. For lack of better knowledge, we did not take the potential affects into account in analyzing the data unless otherwise noted in the context.

3.3. The edge pedestal in L-mode plasma of EAST

As aforementioned, the heating power is very low (~200 kW) during the discharge. The probe head can work well inside the separatrix and provide reliable measurements. In this experiment, the probe head reaches the deepest plasma at up to about 4 cm inside the LCFS. A clear structure of edge shear layer is observed inside the separatrix, where an uncertainty of the location of LCFS is about ±5 mm.

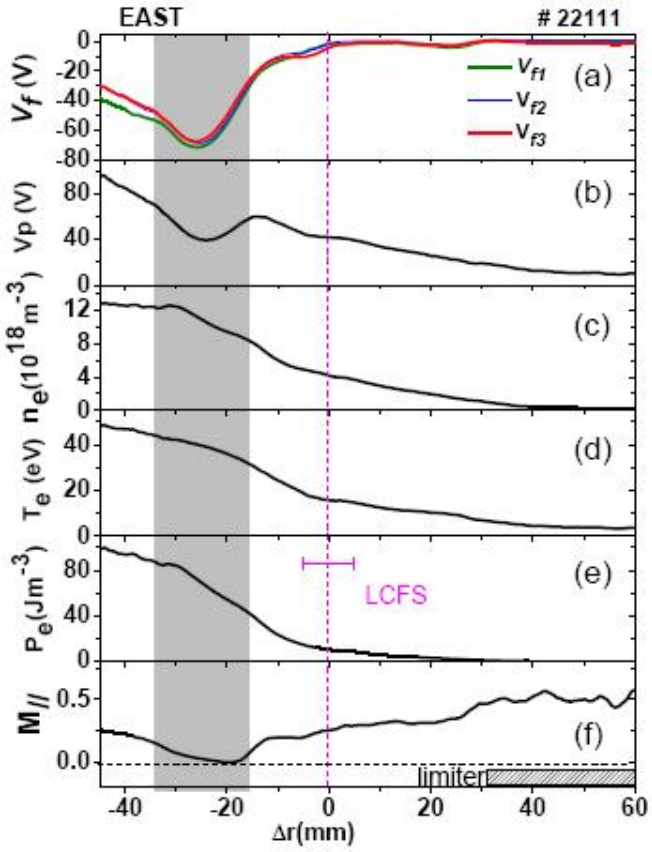

Figure 3.5. Equilibrium profiles measured by probe in the boundary of EAST tokamak during Ohmic discharge #22111 (*a*) floating potential (b) plasma potential (*c*) electron density (d) electron temperature (e) electron pressure (f) parallel Mach number.

Figure 3.5 shows equilibrium profiles measured by Langmuir probe in the boundary of EAST tokamak during Ohmic discharge #22111, which provides basic parameter of background plasma. The shear layer is located inside the LCFS with dip structure as presented in the floating potential as well as plasma potential signal (gray bar marks). As indicated in the figure 3.5 (e), a pedestal structure on the pressure (density) gets formed in the shear layer region. The dip structure is also observed in the parallel Mach number $M_{//}$, which can quantitatively denote the parallel velocity by $v_{\|} = M_{\|} c_s$. The toroidal rotation velocity is approximately equal to the parallel flow

velocity in a low-β tokamak, $v_t \cong v_{\parallel}$, since the toroidal field is much stronger than the poloidal field, $B_t \gg B_p$. Local minimum in $M_{//}$ is observed in valley bottom of the shear layer, from where a co-current rotation increased towards the plasma center and towards the separatrix. The parallel ion flows will be discussed in section 3.7.

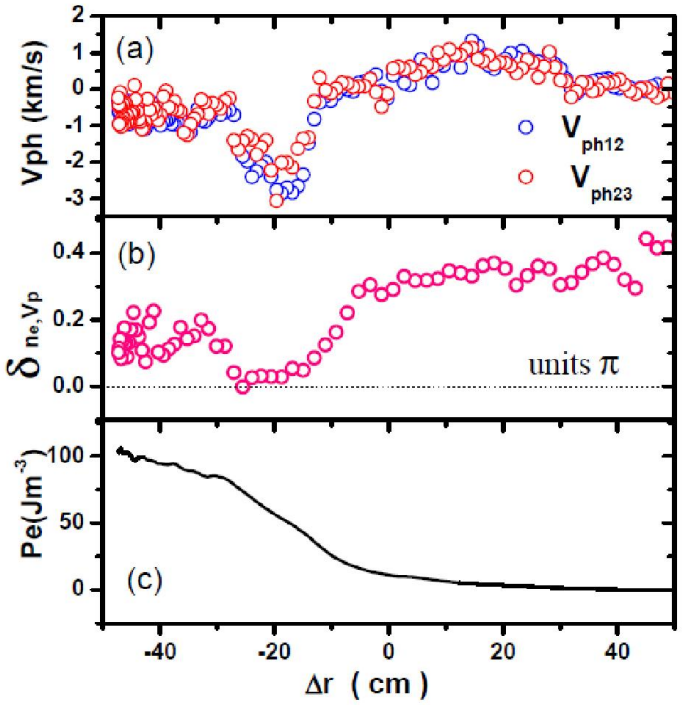

Figure 3.6. (a) Radial profile of background turbulence velocity V_{ph12} and V_{ph23}, flowing from V_{f1} to V_{f2}, V_{f2} to V_{f3}, respectively, (b) Radial profile of $\delta_{ne,vp}$ between the density and plasma potential, (c) Radial profile of electron pressure.

The phase velocity of background turbulence was inferred from the time-delay of the eddies embedded in local turbulence. The time delay estimation is based on the cross-correlation of fluctuation signals measured at two spatially separated channels. Two floating potential signals V_{f1} and V_{f2} (V_{f2} and V_{f3}) are used to determine the poloidal velocity fields of local turbulence in our measurements. Figure 3.6 shows the poloidal phase velocity V_{ph12} from V_{f1} to V_{f2}, V_{ph23} from V_{f2} to V_{f3}. As can be seen in figure 3.6 (a), V_{ph12} and V_{ph23} agree well to each other. Outside the LCFS, the turbulence propagates in the ion diamagnetic direction. Inside the LCFS, the turbulence propagates in the electron diamagnetic direction. Particularly, a remarkable velocity shear layer exhibits in the steep pressure pedestal region. In the edge velocity shear layer, the cross-phase angle $\delta_{ne,vp}$ between the density and plasma potential decrease to zero. It is seems that the $\delta_{ne,vp}$ is modified to zero by the shear flows. The cross-phase angle $\delta_{ne,vp}$ increase to 0.4 π in the SOL, which suggests the interchange

driven turbulence prevailing in the SOL.

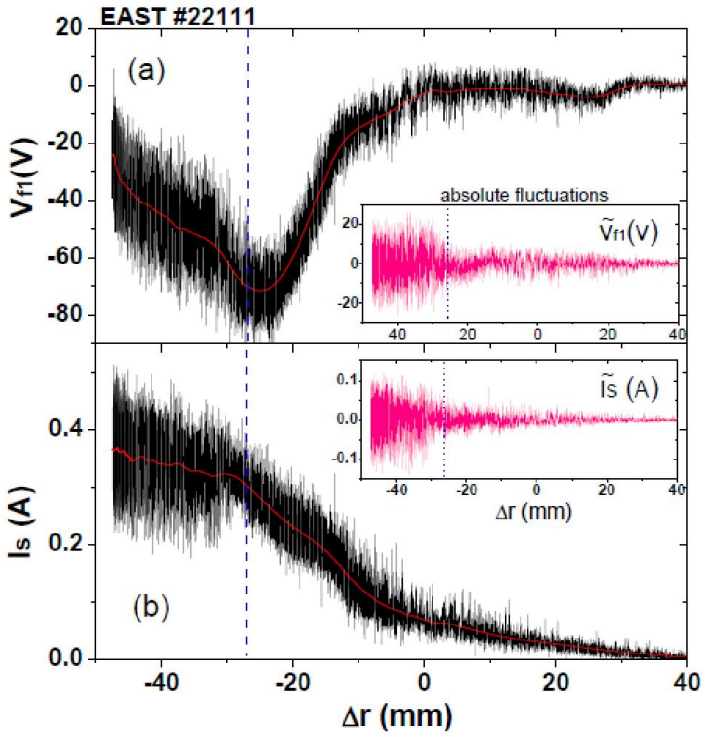

Figure 3.7. (a) Floating potential V_{fl} signals measured along the radial radius, red curve indicates the mean value, (b) Ion saturation current signal I_s measured along the radial radius, red curve indicates the mean value. Pink signals present the absolute fluctuations of signals.

Radial spreading of turbulence in the plasma context was firstly proposed by Mattor and Diamond [94]. It suggested that the radial nonlocal transport of core fluctuation can serve as a possible source of edge plasma turbulence. However, experimental evidence supporting plasma turbulence spreading are very limited [95]. Recently, signatures of spatial spreading of the turbulence are identified by asymmetry of density fluctuations on both sides of edge shear layers at the H–L back-transition in TJ-II plasmas [96]. In our measurements, as shown in the figure 3.7, the turbulence intensity on the inner side of shear layer is distinctly higher than it outside of the shear layer, even though the gradients outside the shear later is much steeper. It may suggest the turbulence presenting in the inner side of shear layer are not generated on site. The radial propagation of turbulence is potentially blocked by the edge shear layer, leading to a robust quenching of turbulence observed outside the shear layer.

3.4. Characteristic of density fluctuations of boundary plasma

3.4.1 Statistical properties of the density fluctuations across the separatrix

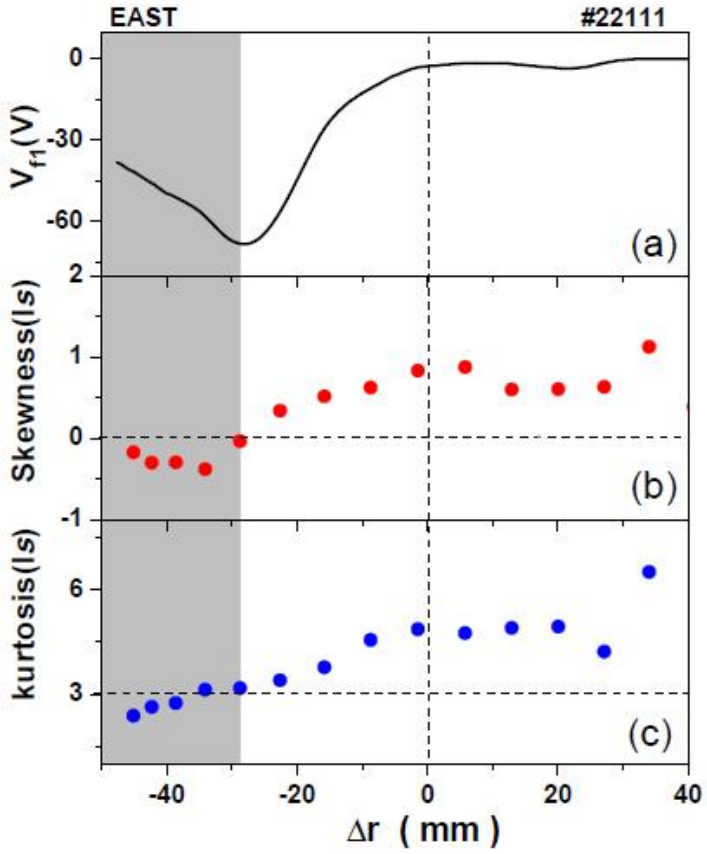

Figure 3.8. (a) Radial profiles of floating potential signal V_{fl} , (b) Radial profile of skewness of ion saturation current fluctuation signal , (c) Radial profile of kurtosis of ion saturation current fluctuation signal.

The statistical properties of the density fluctuations are investigated with the ion saturation current signal across the separatrix. In order to ensure the statistics to be reliable, the Ohmic heating power needs to be kept at the low value during the discharge to prevent plasma arcing on the tips of ion saturation current. The probability distribution function (PDF) of density fluctuations is used to investigate the deviation from the Gaussian distribution. The deviation from the Gaussian distribution can be characterized by skewness (S) and kurtosis (K) [97]. The skewness $S=\langle(x-\langle x\rangle)^3\rangle/\langle(x-\langle x\rangle)^2\rangle^{3/2}$ describes the asymmetry of the PDF, while the kurtosis $K=\langle(x-\langle x\rangle)^4\rangle/\langle(x-\langle x\rangle)^2\rangle^2$ quantifies the tail weight with respect to the central distribution, where x is the statistical quantity (ion saturation current here). If the left tail is more pronounced than the right tail, the PDF has negative skewness and when the reverse is true, it has positive skewness. In particular, for the Gaussian distribution function: S=0, K=3.

As is shown in figure 3.8, the profiles of skewness and kurtosis of density

fluctuations are estimated with ion saturation current ($I_s \propto n_e$) measured in the boundary plasma. The probability distribution function of the turbulent density fluctuations is less skewed where both floating potential and plasma potential have a dip well, with positive skewed events ("blobs") prevailing in the outer side of shear layer and SOL region (Δr >-28 mm) and negative skewed events ("holes") propagating in the inner side of shear layer (Δr <-28 mm). Our observations suggest that plasma coherent structures (blobs/holes) originate from the bottom of edge shear layer on EAST. These results coincide with previous observations from the JET tokamak [87], ASDEX Upgrade [88] and HL-2A [89], where it was reported that the generation regions of coherent structures were located within the shear layer.

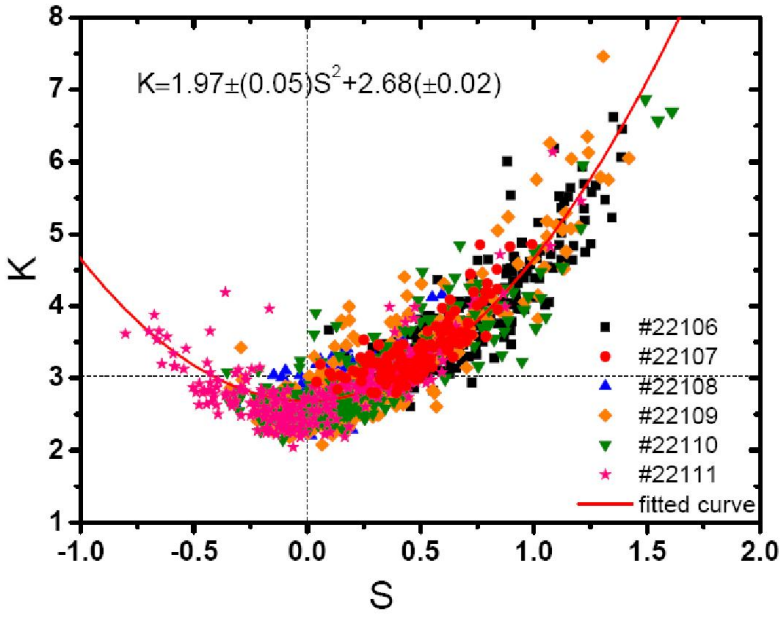

Figure 3.9. Parabolic relationship between kurtosis and skewness of ion saturation current fluctuation signals. For the Gaussian distribution function: S=0, K=3.

The statistical properties are collected from the boundary plasma (-4cm<△r<3cm) in several similar discharges (#22106 - #22111). As is shown in figure 3.9, the S and K are found to obey a parabolic relationship ($K = 1.97S^2 + 2.68$). The positive S is dominated by density enhancement events (blobs), and negative S is related to density depletion events (holes). They demonstrate symmetric distribution around zero. A similar relation between S and K has been reported recently in ASDEX Upgrade [88] and HL-2A [89]. An extensive comparison of edge turbulence data taken from multiple machines proves this parabolic curve between S^2 and K universally exists in different configurations [98] as well as in hydrodynamical and astrophysical systems dominated by intermittent fluctuations [99, 100]. The coefficient in front of the S^2 might be related to a drift-interchange turbulence physical process, which is investigated on TORPEX [101]. Recently, many statistical models are developed to

interpret such parabolic relationship [98, 102-107]. Some of them point out that the parabolic relation between S and K encountered in the statistical treatment of data from turbulent systems is not likely to provide relevant information about the underlying instability [103, 104]. Interestingly, when the intermittent burst events with a fixed wave form occur in accordance to a Poisson process, a parabolic relation between the skewness and kurtosis moments of the plasma fluctuations can be reproduced [104]. In Ref. [103], it is argued that the parabolic scaling between the skewness and kurtosis stems from the convective motion of turbulent elements.

Large amplitude density structures could be selected by imposing a threshold (Th) in density or ion saturation current. The threshold usually is several time root mean square of density fluctuations σ. Candidate events above a certain density threshold are supposed to be caused by the coherent structures propagating in the turbulence. The numbers of the candidate events with different density threshold is estimated over density fluctuations (~2ms) measured at the different radial positions. As is shown in the figure 3.10, the density fluctuations above 0.5 σ, σ, 1.5 σ, are almost equal with the density fluctuations below -0.5 σ, -σ, -1.5 σ. However, the density fluctuations above 2 σ, 2.5σ, 3σ is dominating over the density fluctuations below -2 σ, -2.5σ, -3σ at the region -28 mm< Δr < 30mm, and the density fluctuations above 2 σ, 2.5σ, 3σ is less than the density fluctuations below -0.5 σ, -σ, -1.5 σ at the region -40mm< Δr < -28 mm. We did not detect the burst events below -3.5 σ in the density fluctuations. This observation is consistent with our conclusion from the radial profile of S and K. The distribution of amplitude of density fluctuations provide a approach to distinguish the isolated coherent structures from the background turbulence.

Density holes or blobs are very well embedded in the ambient turbulence. Once they are identified, the properties can be appreciated. Conditional average [108, 109], is a good method to extract coherent blob structures. The conditional average is obtained by recording limit time evolution data points around the maximum of each burst event and then accumulating and averaging the selected events. If the selection by the condition and the average are performed for the same signal, it is called an auto-conditional average (ACA). If the former and the latter are done for two different signals, it is called a cross-conditional average (CCA). The fluctuations over a specified amplitude threshold are recorded as candidate events. The burst events in the ion saturation current signal are used as the condition to select time slices of the other signals. In our analysis, we set the ion saturation current as a condition to investigate the averaged radial drift velocity, which essentially reflected the poloidal electric field inside or nearby the blobs/holes.

The blobs/holes has been universally observed in many devices with a monopolar density pulse prominently higher than the surrounding density fluctuations of background plasma [73]. The electrostatic potential perturbations associated with

propagation of blobs have been measured using Langmuir probes in many tokamaks [110]. Two dimensional spatial maps of the vortex-like potential structure of blobs have been revealed in TORPEX[67], LAPD [111], which clearly reveals that the coherent structures (blobs/holes) are of a monopolar density topology yet dipolar potential geometry.

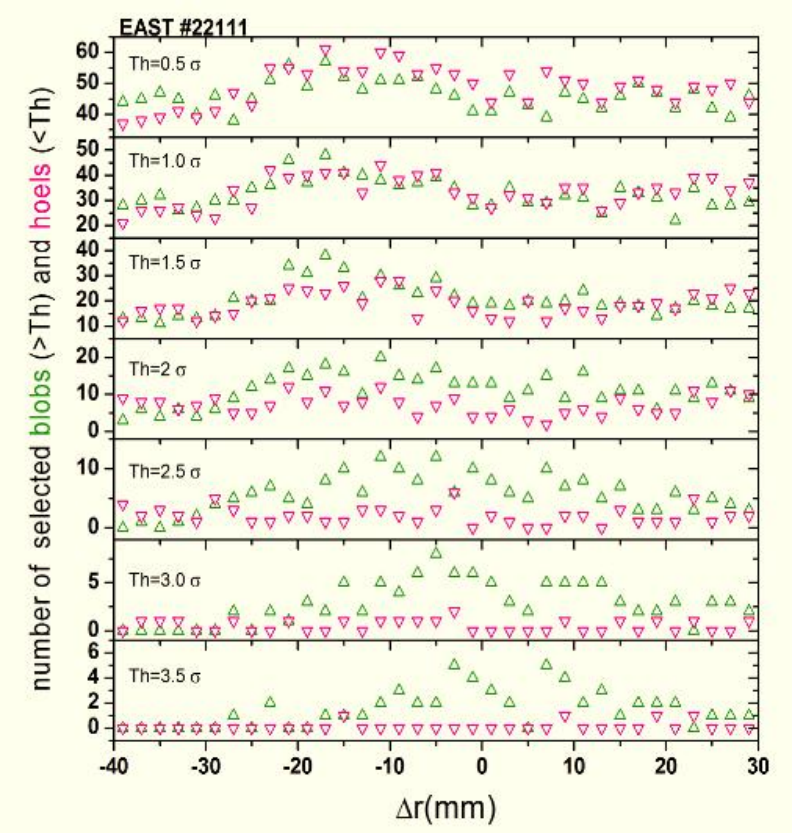

Figure 3.10. Statistical numbers of burst events above/below a given density threshold.

In figure 3.11, the ±2 σ (room mean square of density fluctuations) thresholds are used to detect the blobs and holes within 2.0 ms time series of ion saturation current signal measured at different position Δr≈-30, -15, 15mm. It is found that radial drift velocity V_r presents a distinct pattern at the position Δr≈-15mm. the single spike structures of V_r are revealed by CCA around the position Δr≈-30, 15mm. However, a sinusoidal oscillation pattern is detected in V_r around the position Δr≈ -15mm. As indicated in the figure 3.6, the background flows speed up to 3km/s in the shear layer but decline to ~0.5km/s in the near SOL and on the top of edge pedestal. It is evident in our measurements that the poloidal velocity of shear flows significantly influence our observation on potential structure of blobs. The fast poloidal movement of blobs enable the probe array to resolve poloidal distribution of potential structure before the blobs pass the probe head radially. Therefore, it is more convincible for us

that sinusoidal V_r detected at position $\Delta r \approx -15$mm implies a dipolar structure of plasma potential in the poloidal direction. The topology of blobs potential will be demonstrated in the ESEL simulation in the following section, which is consistent will our conjecture here.

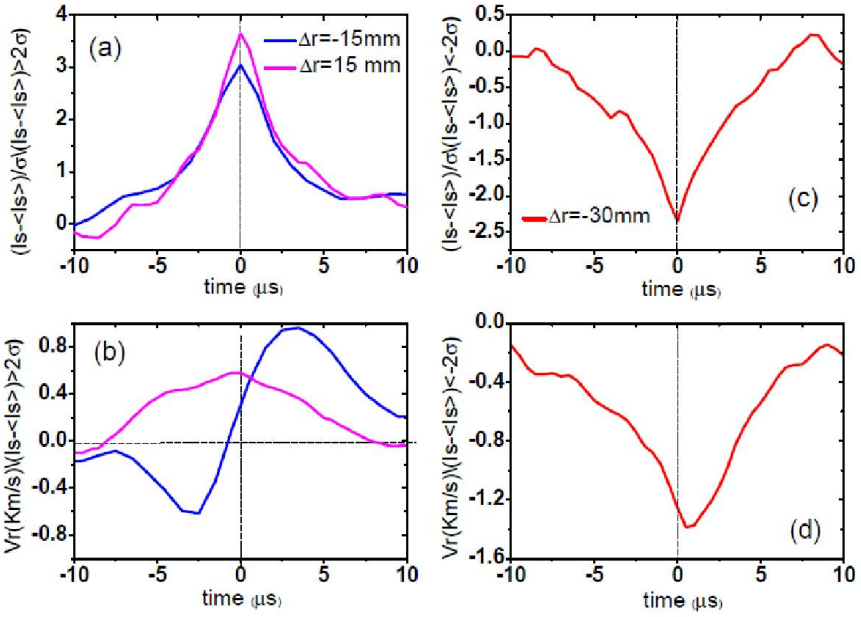

Figure 3.11. (a) (c), CA of ion saturation current and (b) (d) ,CCA between ion saturation current (served as threshold) and radial velocity V_r at three different position $\Delta r \sim -30$mm, $\Delta r \sim 15$ mm, $\Delta r \sim -15$mm respectively.

3.4.2 ESEL simulations on density fluctuations

Governing equations of the ESEL code

Motivated by the success of ESEL code in reproducing the characteristic of SOL plasma in TCV and MAST tokamak, we implement a ESEL simulation with EAST parameter to promote our understanding on the blobs. As a two-dimensional reduced fluid model for low-frequency (far below the ion gyration frequency) plasma dynamics, ESEL uses a set of fluid equations appropriate for the boundary region on the out-board mid-plane of a toroidally magnetized plasma. Emphasis has been put on the nonlinear collective dynamics due to non-uniform magnetic field while neglecting parallel currents in the plasma edge region and invoking linear damping terms in order to describe parallel loss of plasma, heat and electric charge in the SOL [82]. Presuming the cold ions, the ESEL equations govern the self-consistent evolution of particle density n, electron temperature T_e and electric drift vorticity Ω,

$$\frac{\mathrm{d}n}{dt} + nC(\phi) - C(nT_{\mathrm{e}}) = \Lambda_{\mathrm{n}} n, \tag{3.2a}$$

$$\frac{\mathrm{d}T_{\mathrm{e}}}{dt} + \frac{2T_{\mathrm{e}}}{3}C(\phi) - \frac{7T_{\mathrm{e}}}{3}C(T_e) - \frac{2T_{\mathrm{e}}^2}{3n}C(n) = \Lambda_T T_e, \tag{3.2b}$$

$$\frac{\mathrm{d}\Omega}{dt} - C(nT_e) = \Lambda_{\Omega}\Omega, \tag{3.2c}$$

where the vorticity, the advective derivative, the curvature operator are defined, respectively, by

$$\Omega = \nabla_{\perp}^2 \phi, \quad \frac{\mathrm{d}}{\mathrm{d}t} = \frac{\partial}{\partial t} + \frac{1}{B}\vec{b} \times \nabla\phi \cdot \nabla, \quad C = -\frac{\rho_s}{R_0}\frac{\partial}{\partial y} \tag{3.3}$$

The ϕ is a normalized plasma potential φ as $\phi \approx \mathrm{e}\varphi / T_{e0}$. Above equations are dimensionless which are normalized using the Borm normalized scheme. Temporal scale t is normalized by the ion gyration frequency $\omega_{ci0} = eB_0 / m_i$ and spatial scales (x, y) are normalized by the hybrid thermal gyration radius $\rho_{s0} = c_{s0} / \omega_{ci0}$, respectively. Here $c_{s0} = \sqrt{T_{e0}/m_i}$ is the cold ion sound speed, B_0 is the magnetic field line strength and the zero subscript indicates nominal (dimensional) values, typically chosen at the separatrix location on the outboard mid-plane of the tokamak. The particle density n and electron temperature T_e are normalized by characteristic values n_0 and T_{e0} at the separatrix respectively. The right hand of ESEL equations signify the combined perpendicular diffusion and parallel loss along the magnetic field line, which is expressed as follows:

$$\Lambda_{(n,\,T_e,\Omega)} = D_{(n,\,T_e,\Omega)}\nabla_{\perp}^2 - \frac{1}{\tau_{//(n,\,T_e,\Omega)}} \tag{3.4}$$

Where $D_{(n,\,T_e,\Omega)}$ is perpendicular diffusion coefficient normalized by $\rho_{s0}^2 \omega_{ci0}$, and $\tau_{//(n,\,T_e,\Omega)}$ is parallel loss time normalized by $1/\omega_{ci0}$. The former is taken to be spatially uniform while the latter changes with radius in steps according to

$$\frac{1}{\tau_{//(n,\,T_e,\Omega)}} = \begin{cases} 0 \ \ for\ x < x_l \\ \sigma_{l(n,\,T_e,\Omega)}\ for\ x_l < x < x_w \\ \sigma_{w(n,\,T_e,\Omega)}\ for\ x > x_w \end{cases} \tag{3.5}$$

Here, x_l and x_w denote the radial position of LCFS and limiter walls, respectively. σ_l and σ_w are constants representing the strength of the parallel loss. The absence of parallel losses for $x < x_l$ simulates the region of closed magnetic field lines. Finite values for $\tau_{//}$ correspond the SOL and wall shadow regions. The model comprises distinct forcing and damping regions, corresponding to the edge region and

SOL of magnetized plasmas, and governs the evolution of the particle density, the electron temperature and vorticity of the electric drift.

For the EAST discharges considered here, the parameters are given by B_0=1.8T, R_0=1.88m，a=0.45m. At the separatrix, the electron density and temperature are 5×10^{18} m^{-3} and 20 eV, respectively. The near SOL has parallel connection length $L_{//}\sim 1/2\pi qR_0$ and moderate collisionality $\nu_e^*\equiv L_{//}/\lambda_{ei}\sim30$, where λ_{ei} is the mean free path of collisional electrons-ions. The SOL plasma tends to be appropriately modeled by ESEL at high collisionality on TCV [77, 82]. In far SOL, plasma is in the shadow region of the limiter, which defines the wall radius.

The transport coefficients implemented in the ESEL simulation are estimated using the experimental measured plasma parameter at the LCFS on EAST. They read as follows:

$$\begin{aligned} &D_n \approx 1.8\times10^{-3},\ D_T \approx 1.0\times10^{-2},\ D_\Omega \approx 3.5\times10^{-2},\\ &\sigma_{l,n} \approx 1\times10^{-4},\quad \sigma_{l,T} \approx 2\times10^{-4},\quad \sigma_{l,\Omega} \approx 1\times10^{-4}, \end{aligned} \tag{3.6}$$

In the wall shadow region, the linear damping term is increased by a factor of 20 to owing to the prescribed shorter connection length in our simulation.

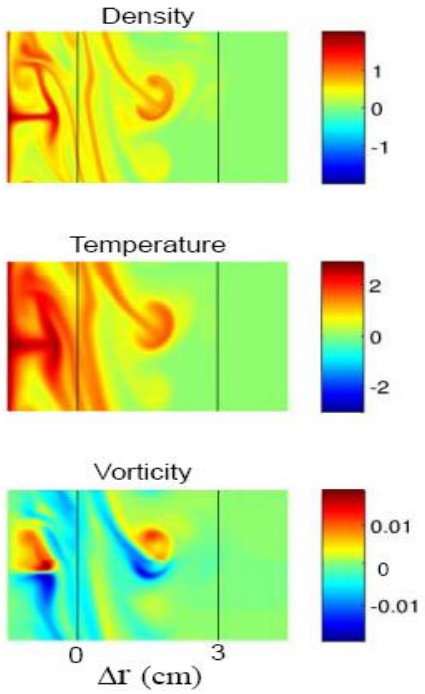

Figure 3.12. Snapshot from ESEL simulation benchmarked with plasma parameters on EAST, which shows the structure of blob Density, Temperature and Vorticity respectively. The separatrix is signified as △r=0 cm, and the limiter shadow located △r>3 cm.

As is shown in figure 3.12, a clear blob-like coherent structure is observed in the SOL region with higher density and temperature than the background plasma. Distinct from the monopolar distribution of density and temperature, the vorticity exhibits a pronounced dipolar pattern inside the structure.

Comparison of experimental measurements and ESEL simulations

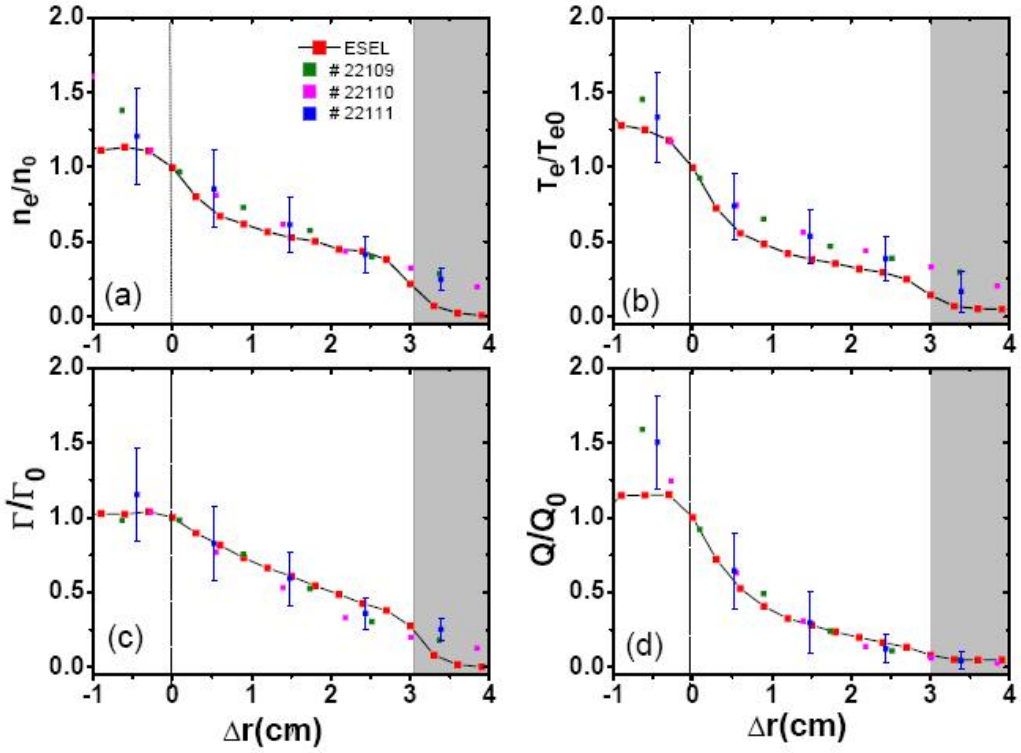

Figure 3.13. Radial profiles of experiment results and simulation normalized to their value at the LCFS (a) averaged density (b) averaged Temperature (c) averaged particle flux (d) averaged heat flux. The error bars represent one standard deviation of the experimental data.

For further verifying the accuracy of the ESEL model, the comparisons between the ESEL outcomes and probe experiments are performed**.** The figure 3.13 shows the normalized profiles from EAST measurement and ESEL simulation. The error bars represent one standard deviation of the experimental data acquired in similar discharges, among which the well repeated shots (#22109-#22111) are adopted for the data analysis in this section. Remarkably, a plateau-like structure has been developed both for the density and temperature profile in the SOL. This kind of non-exponential profile may suggest the existence of robust enhanced cross-field transport, which leads to an increase of the particle and energy flux far away from the last closed flux surface, exceeding what would be expected in the case of a diffusive local transport process. As is well known, the SOL width is determined by the competition of parallel loss along the magnetic field line and perpendicular transport. The broad particle and temperature profile are potentially suggestive of radial turbulence driven transport dominating over parallel losses, which may accumulate the particle and energy and lead to the broad profile at mid-plane. A similar enhanced cross-field transport was also identified in the outboard mid-plane of Alcator C-Mod, which drive a significant

flow along magnetic field lines from the low- to high-field SOL [78]. In both the wall shadow region and inside the separatrix, the agreement between experiment and simulation becomes worse, since the ESEL code are not able to describe fully the physics in that domain. The useful information produced in the ESEL simulation essentially lie in the SOL region, i.e. 0 cm <△r < 3 cm in this section.

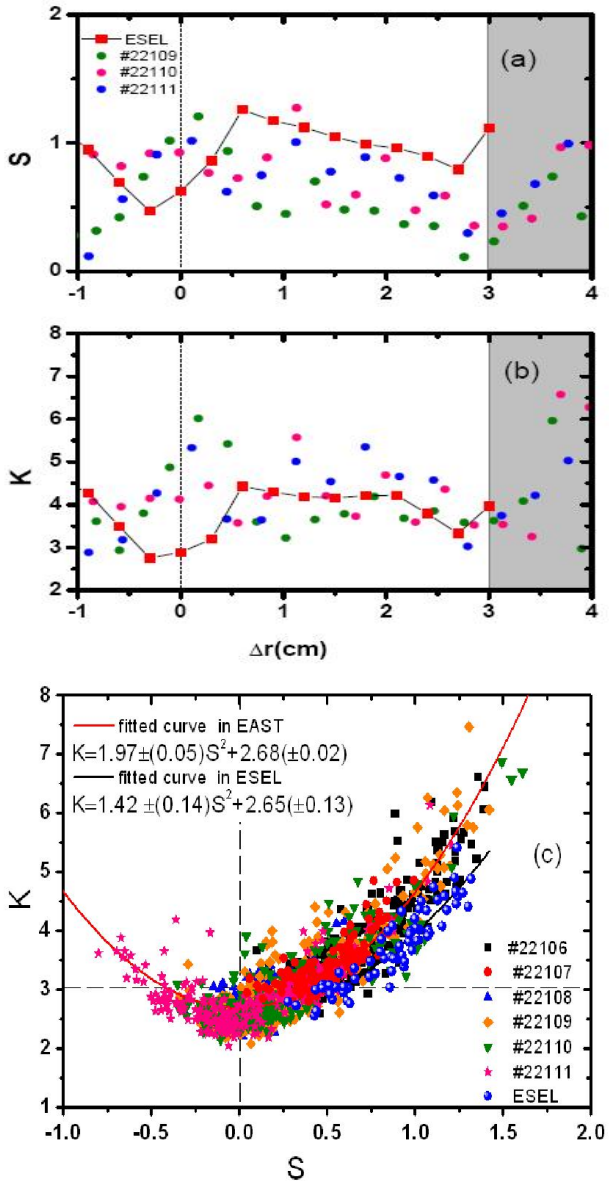

Figure 3.14. Radial profile of experiment results and simulation (a) skewness of density fluctuations (b) kurtosis of density fluctuations (c) Parabolic relationship between skewness and kurtosis of the density fluctuations in ESEL simulation together with parabolic relationship between skewness and kurtosis of the density fluctuations in ESAT measurements.

In figure 3.14, the statistical characteristics are further compared between the

experimental measurements and the ESEL simulation. As manifested in the ESEL simulation, the skewness and kurtosis of the electron density fluctuations increase outwards in the vicinity of separatrix. Taking the uncertainty (±5 mm) of location of LCFS on EAST into account, the ESEL prediction is generally consistent with the experiment measurements in the vicinity of LCFS on EAST. The skewness shows a decreasing tendency while the kurtosis keeps almost constant in the remaining SOL ($\Delta r > 0.8$ mm) in the ESEL simulation, which qualitatively agrees with the property of SOL turbulence on EAST. Specifically, the predicted value of kurtosis of the electron density fluctuations in ESEL is well located in the scope of the values estimated from the experimental measurements on EAST, but the predicted kurtosis of the electron density fluctuations in ESEL is slightly beyond the variation range of the values estimated from the experimental measurements on EAST. The skewness and kurtosis of the electron density fluctuations deviated significantly from the measured values in the limiter shadow region, which are thus not demonstrated here. Figure 3.14 (c) shows that a parabolic relationship between S and K of density fluctuations in the simulation, which is quite similar with our experimental observation. The coefficient b of the fitting function ($K=aS^2+b$) shows an excellent match between measurement and simulation. It is worthwhile to note that the both coefficients for experiment and simulation quantitatively reach an agreement with the scaling of multiple devices, where available statistical data in L-mode plasma shows:$1<a<2$, $2<b<3$ [97].

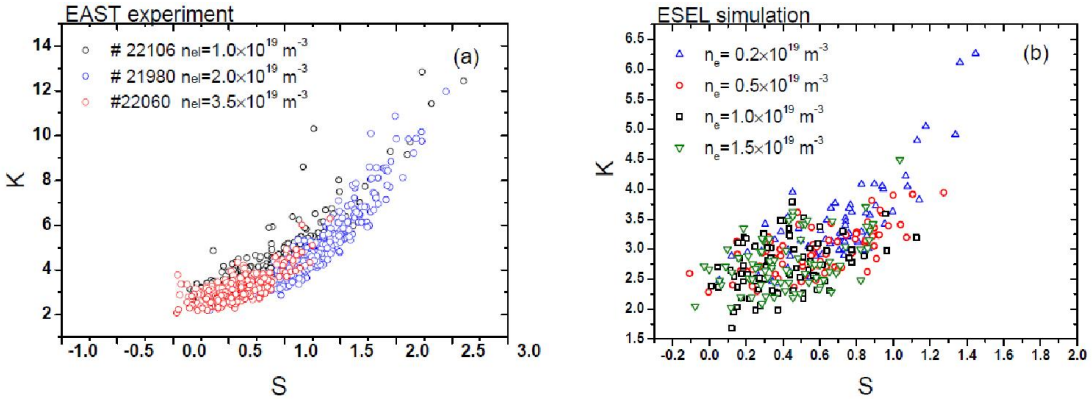

Figure 3.15. (a) Skewness and kurtosis of density fluctuations in discharges with different density on EAST, (b) Skewness and kurtosis of density fluctuations in ESEL simulations with different density.

The dependence skewness and kurtosis of density fluctuations on density are investigated both in EAST and ESEL simulations. As is shown in the figure 3.15 (a), the skewness and kurtosis of density fluctuations obtained in the discharges with different density agree well with each other. The same case are observed in the

ESEL simulations (figure 3.15 (b)). This suggest that the density is not the key factor for the regulation of parabolic relationship of skewness and kurtosis. The hidden variable responsible for the parabolic curve is not clear yet.

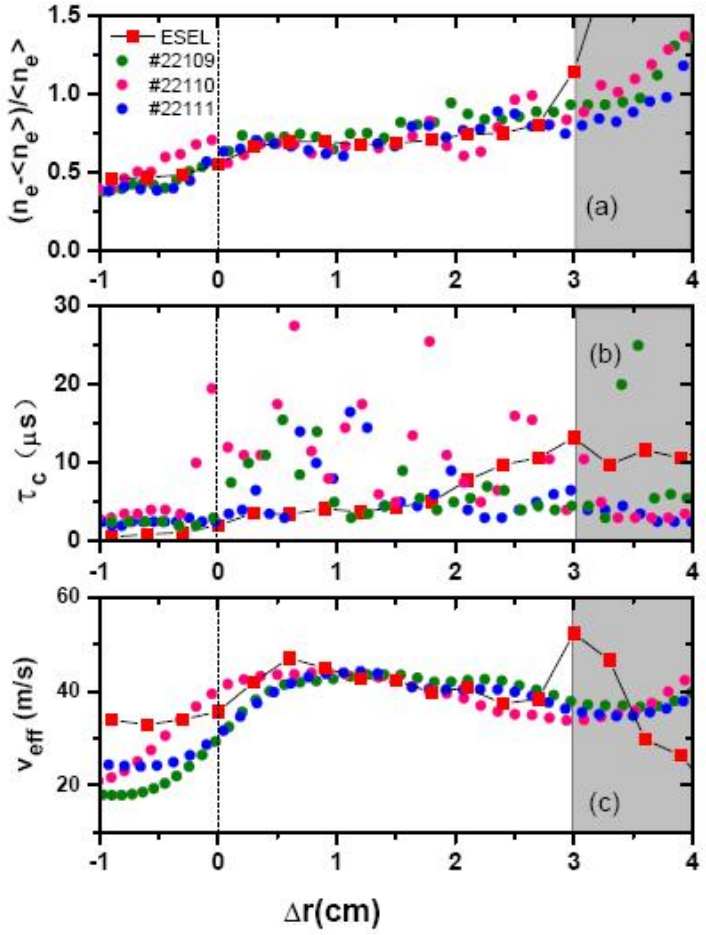

Figure 3.16. Radial variation of experimental results and simulation results (a) relative density fluctuation level (b) auto correlation time of local turbulence (c) effective radial velocity.

As is shown in the figure 3.16, the relative fluctuation levels of density increase from the closed field line edge region towards open field line SOL regime in the experiment. It increase to 1 in the limiter shadow region. The relative fluctuation levels in ESEL are close to the measurement in the SOL. The auto correlation time τ_c of electron density fluctuations is much higher in the SOL than it is in the edge and wall shadow on EAST. Compared to the experimental measurement, the ESEL simulation predicts a lower auto correlation time for the turbulence plasma in the SOL. The effective radial velocity is defined as $V_{eff}=\Gamma/<n_e>$. It significantly depends on the the turbulent particle flux Γ. The V_{eff} estimated from the simulation is comparable with it in measurements. Similar with the evolution with S and K, the V_{eff} increases in the vicinity of LCFS, and decreases outwards in the remaining part of SOL on

EAST. It suggests that the transport in the SOL is strongly correlated with the appearance of coherent structures, which leads the density fluctuations to deviate from Gaussian distribution.

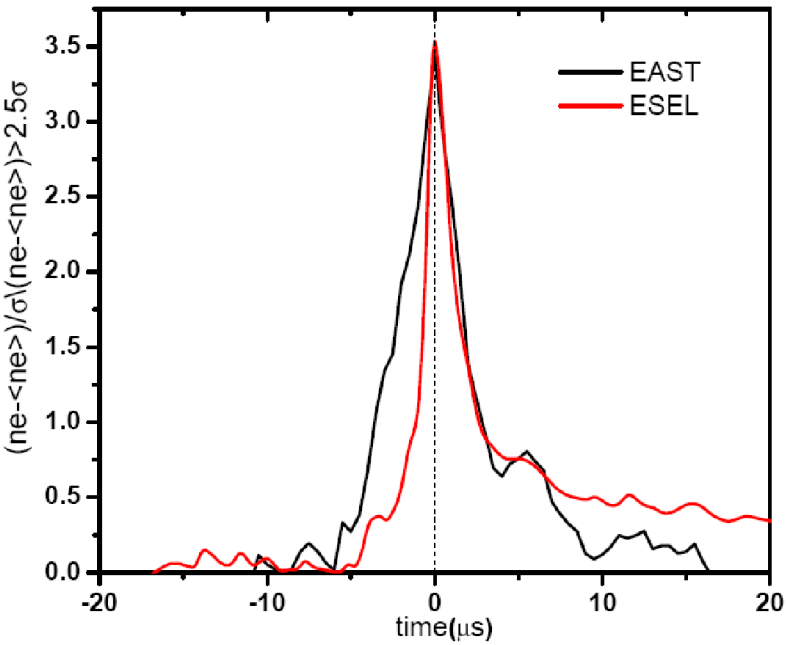

Figure 3.17. Comparison of the conditionally averaged waveforms of density signal from experiment and simulation data at the radial SOL position △r ~2.5 cm.

Conditional average is applied to the density signal of probe measurement on EAST and simulation data, respectively. The conditional average is taken over all density bursts exceeding 2.5 times the standard deviation of density fluctuations. As can be seen in figure 3.17, the amplitude of the burst is almost equal for experimental observation and simulation results. A pronounced asymmetric feature is presented on the density burst structure on ESEL results, which is characterized by a steep front and trailing wake as reported on TCV [82]. This kind of asymmetric structure has been widely realized on other machines [80, 87, 89, 111]. However, asymmetry is less pronounced for the coherent plasma structure in EAST. The rising time of the burst is found to be comparable to the decaying time. In HL-2A [89], it is found that ratio between raising time and decay time of blobs linearly depend on the total bicoherence of local turbulence. The bicoherence of turbulence are not fully described in ESEL code, which could be a reason that the ratio between raising time and decay time of blobs is underestimated here in the simulation.

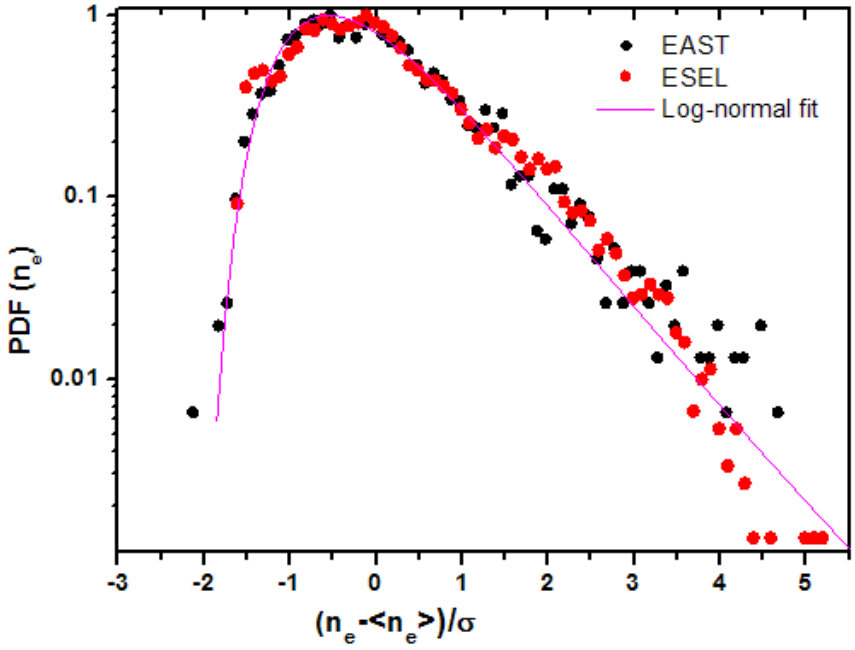

Figure 3.18. Comparison of the PDF of density fluctuations signal from experiment and simulation results at the radial position △r ~2.5 cm.

The rescaled PDF of normalized particle density fluctuations in figure 3.18 demonstrates an excellent agreement with experimental measurements. Both of the PDFs exhibit an asymmetric wing with large positive amplitudes events, which significantly indicate the dominance of bursts/blobs in the density fluctuations. The pink line in figure 3.18 is a Log-normal fit on the PDF of density fluctuations, which match well with the experimental and simulation results. Such log-normal distribution has also recently been reported to be a typical representation of the PDF of density fluctuations in the SOL of the RFX device [106] and TCV [105]. It indicates that the coherent structures are striking in the background density fluctuations. As depicted in figure 3.7, the turbulence intensity is significantly reduced in the SOL, which directly leads the isolated blobs to become more distinguishable in the background turbulence.

3.5. Investigation on temperature fluctuations

3.5.1 Experimental observations on temperature of blobs

It has been widely observed that the temperature inside the blobs is in phase with the density topology of blobs [108]. However, the recent measurements in the SOL of ASDEX Upgrade show that there is a remarkable drop of temperature in the blob center [51]. A anti-phase between the density and temperature inside the blobs was also observed in the reversed field pinch RFX-mod [112]. Their observations blur the cognition on the energy distribution in the blobs. To improve the understanding on the temperature topology of blobs, we carried out the Langmuir probe measurements in the limiter and divertor plasma respectively.

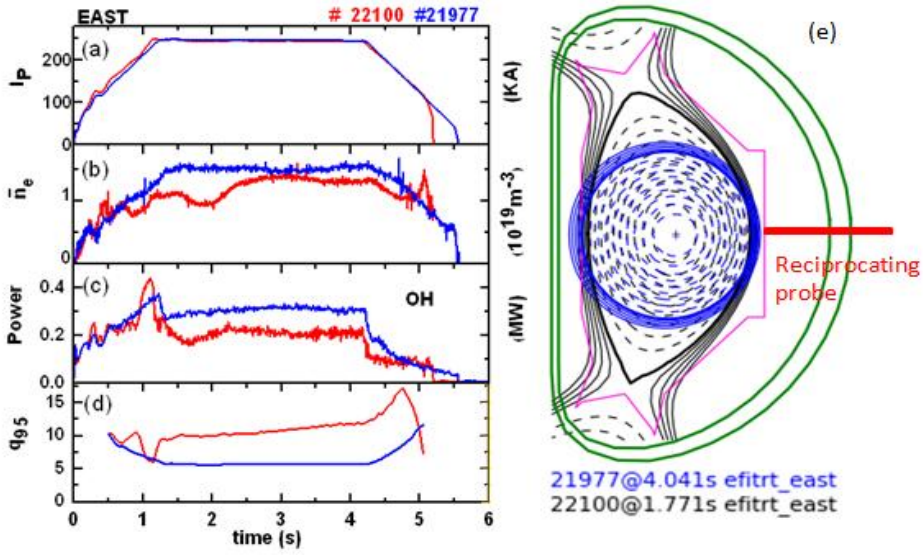

Figure 3.19. (a) the plasma current, (b) the line averaged density, (c) the input Ohmic heating power , (d) safety factor at the 95% of the normalized magnetic flux surface, (e) magnetic configuration calculated by the EFIT.

Figure 3.19 shows the discharge condition for our experiment. #22100 is a double null divertor discharge, and the #21977 is a typical limier discharge. Two discharges are of the same plasma current I_p, and similar plasma density $\overline{n}_e$. The edge safety factor q_{95} is about 10 in #22100, which is twice as large as it in #21977. The SOL connection length ($\pi q_{95} R$) in the limiter discharge #21977 is almost equal to the SOL connection length ($0.5\pi q_{95} R$) in the divertor discharge #22110. The Ohmic heating power is 0.3MW in #21977, 0.2MW in #22110. The temperature fluctuations are investigated by reciprocating probe measurements in these two different scenarios. For convenience, the parameters described below only refer to the fluctuation components of the signal, and they have been normalized by their own stand deviation.

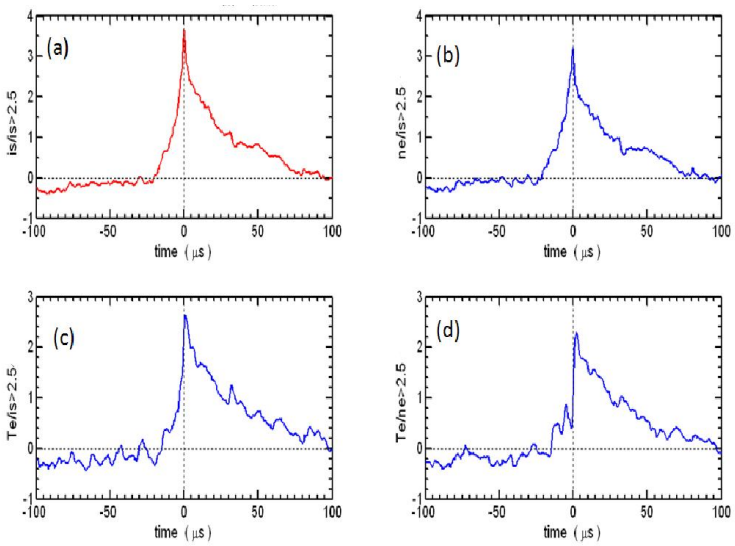

Figure 3.20. Conditionally averaged waveforms of (a) ion saturation current fluctuations triggered by the Is peak, (b) Electron density fluctuations triggered by the Is peak, (c) electron temperature fluctuations triggered by the Is peak, (d) electron temperature fluctuations triggered by the n_e peak. The data are acquired at the middle SOL during limiter discharge #21977.

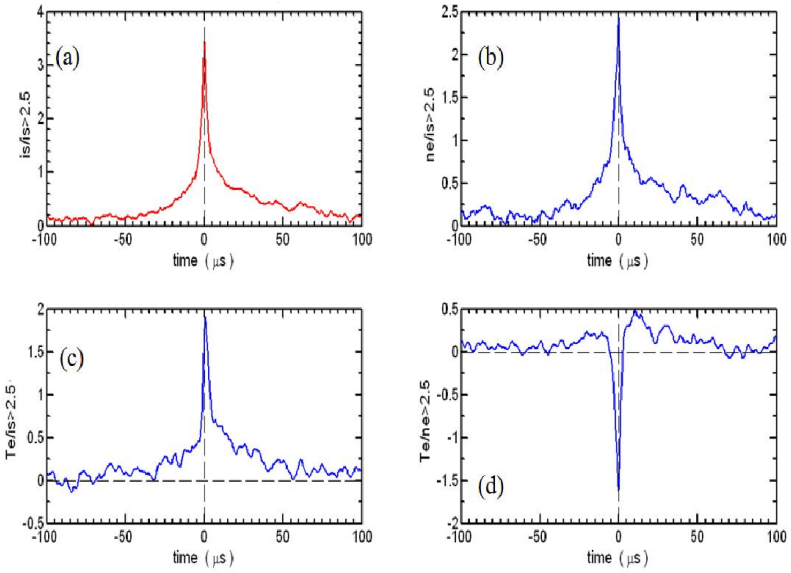

Figure 3.21. Conditionally averaged waveforms of (a) ion saturation current fluctuations triggered by the Is peak, (b) Electron density fluctuations triggered by the Is peak, (c) electron temperature fluctuations triggered by the Is peak, (d) electron temperature fluctuations triggered by the n_e peak. The data are acquired at the middle SOL during divertor discharge #22100.

As shown in the figure 3.21, it is detected that the temperature fluctuations are in phase with the density fluctuations during a blob events in the limiter SOL plasma. However, in the divertor discharge, the temperature fluctuations are observed to anti-phase with the density fluctuations at the blob center. The selected ion saturation current burst are of exceeded density and temperature both in limiter and divertor SOL plasma. Since $I_s \propto n_e\sqrt{T_e}$, the positive I_s spike is mainly contributed by a bulk in plasma density and electron temperature. The ion saturation current are directly measured from the biased double probe, which is of high credibility. As aforementioned, we preliminarily derive the electron temperature T_e as $T_e \approx T_i \approx (V_+ - V_f)/\ln 2$, where V_+ is the floating potential of the biased double probe and V_f is the floating potential. Then, the plasma density could be obtained as $n_e \propto I_s/\sqrt{T_e}$. The electron temperature is a key parameter for estimating plasma density. According to the observations in figure 3.21 (d), it seems that the coherent subjects with intensified density but lower temperature than background turbulence are the dominating populations in the divertor SOL plasma. It should be stressed here, if the decrease of the electron temperature is a false impression from a technical error, the enhancement in plasma density do correspondingly originate from an overestimation.

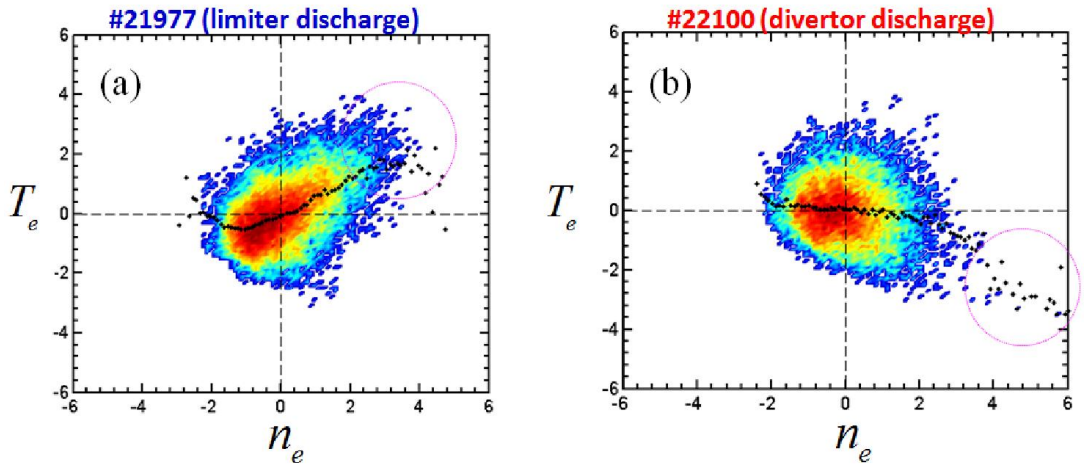

Figure 3.22. (a) The combined PDF of electron density fluctuations and electron temperature fluctuations in middle SOL of limiter plasma. (b) The combined PDF of electron density fluctuations and electron temperature fluctuations in middle SOL of divertor plasma. The black dots demonstrates the statistical average of the PDF of electron density fluctuations and electron temperature fluctuations.

The combined PDF of electron density fluctuations and electron temperature fluctuations is depicted in the figure 3.22. As indicated by statistical average of the

PDF, the temperature fluctuations show a linear dependence on density fluctuations in the limiter SOL plasma. However, the there seems no causal relation between the density fluctuations and temperatures fluctuations in the divertor SOL plasma. The density fluctuations with large amplitude (above 2σ) are preferably of lower temperature than the background plasma. The remarkable difference of plasma behaviour are inquired in these two discharges.

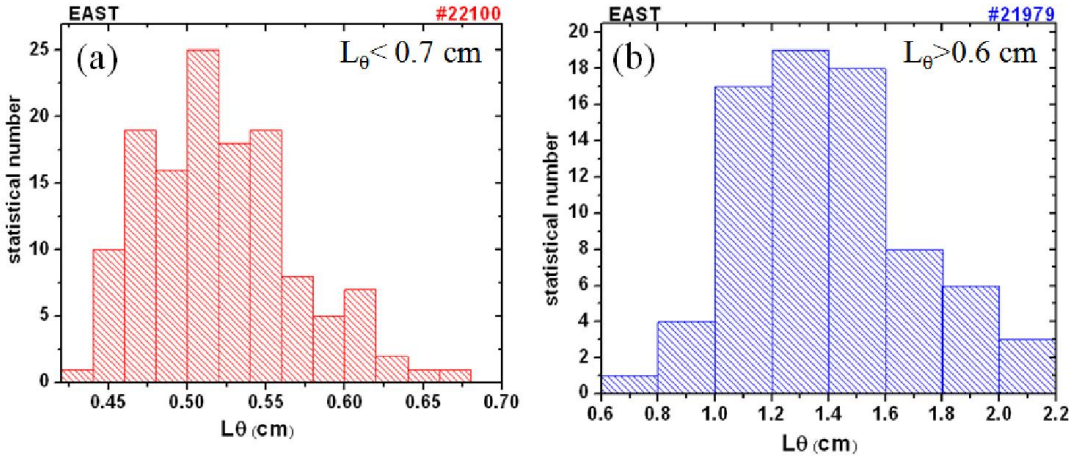

Figure 3.23. (a) Probability distributions of the poloidal connection length of SOL plasma turbulence in the divertor discharge. (b) Probability distributions of the poloidal connection length of SOL plasma turbulence in the limiter discharge.

Poloidal connection length L_θ of plasma turbulence are investigated in the middle SOL using the two-point correlation technique on floating potential signals V_{f1} and V_{f2} (V_{f2} and V_{f3}). As shown in the figure 3.23, the L_θ in divertor plasma are estimated to be smaller than 0.7 cm, and L_θ in limiter plasma are larger than 0.7 cm. This means that spatial scale of SOL turbulence is smaller than the distance (8mm) between two probe tips in divertor discharge. On the contrary, the spatial scale of SOL turbulence is larger than the typical distance (8mm) between two probe tips in limiter discharge. The disinct difference of temperature distribution in blobs may result from the spatial size of turbulence eddies. In the triple probe theory, the probe tips are supposed to locate in the same position. In the practical measurements here, the triple probe tips are separated in space. The Langmuir probe measurements will not be valid if the plasma parameter surrounding the one tips significantly deviate from it surrounding another tips in a triple probe array. The emergence of blobs are not able to cover the probe head in divertor plasma reported here, which is equivalent to impose a inhomogeneous plasma around the Langmuir pins. Therefore, the temperature measurement of blobs in the limiter plasma are more credible.

3.5.2 Temperature fluctuations in ESEL simulations

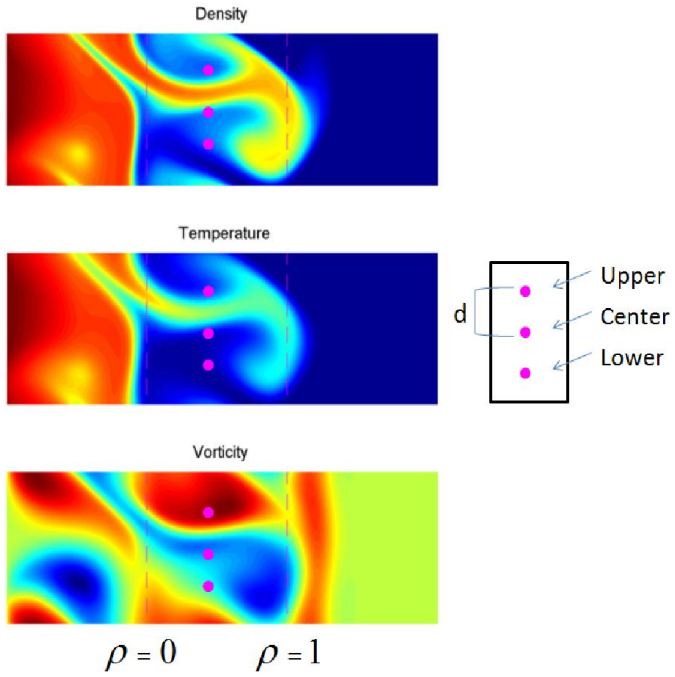

Figure 3.24. Snapshot from ESEL simulation benchmarked with plasma parameters on EAST, which shows the structure of blob Density, Temperature and Vorticity respectively. The separatrix is signified as ρ=0, and the limiter shadow located ρ=1. The pink dots denote the artificial probes separated poloidally by a distance d.

In ESEL simulation, we set up three imitated pins in the middle SOL. It is flexible to change the distance between the tips, which facilitates our study on the sensitivity of temperature measurements to the probe separation. Here, we use the subscript c to indicate the measurements on the center probe, u to signify measurements on the upper probe and l to signify measurements on the lower probe (see figure 3.24). The temperature determined from such probe array could be expressed $T_{ed} = (v_+ - (v_{fu}+v_{fl})/2)/\ln 2$, where $v_+ = v_{fc} + \ln 2 \cdot T_{ec}$ are acquired from the center probe. Ion saturation current is estimated as $I_{sc}=n_{ec}C_{sc}$. The plasma density are calculated as $n_{ed} = I_{sc}./C_{sd}$, where $C_{sd} = \sqrt{T_{ed}/m_i}$. Thus, the imitation of probe measurement can be accomplished in the ESEL simulations. To simplify our discussion here, the two tips of double probe are still located in the same position, i.e. v_+ tip and I_s tip are incorporated in the center probe tip, but they are separated poloidally from floating potential tips. The electron temperature measured at a single point and the electron temperature determined from artificial triple probe array are demonstrated in the figure 3.25. The radial profile of electron temperature deduced from these two different approaches are equal to each other. The fluctuation level of electron temperature determined from artificial triple probe array is smaller than the electron temperature acquired directly at a single point in the ESEL simulation.

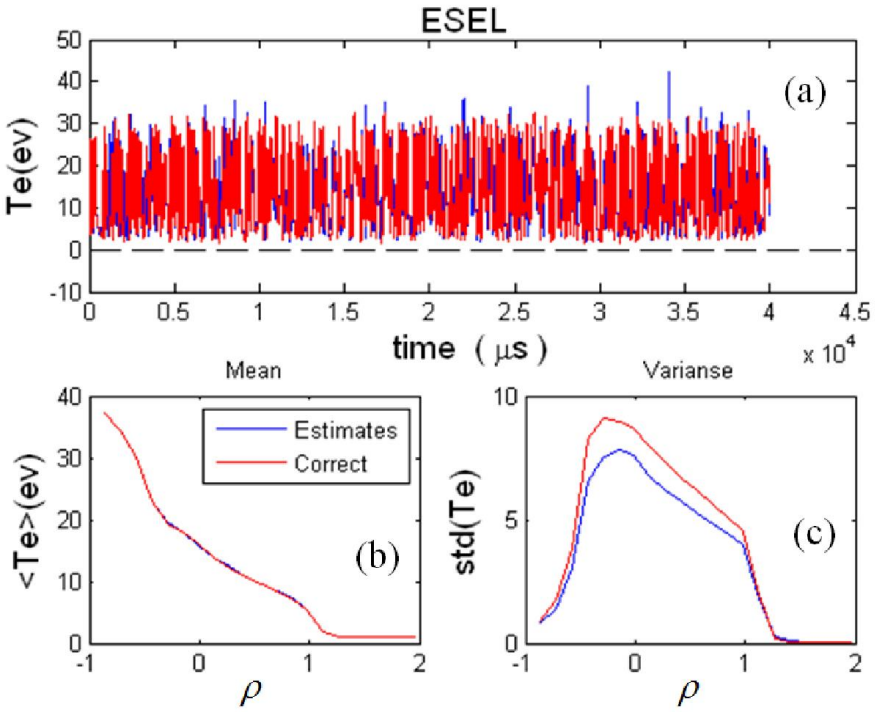

Figure 3.25. (a) The time trace of electron temperature measured at a single point (red) and the time trace of electron temperature deduced electron temperature (blue) from a triple probe array, (b) The radial profile of electron temperature measured using two different approaches, (c) The fluctuation level of electron temperature determined using two different approaches.

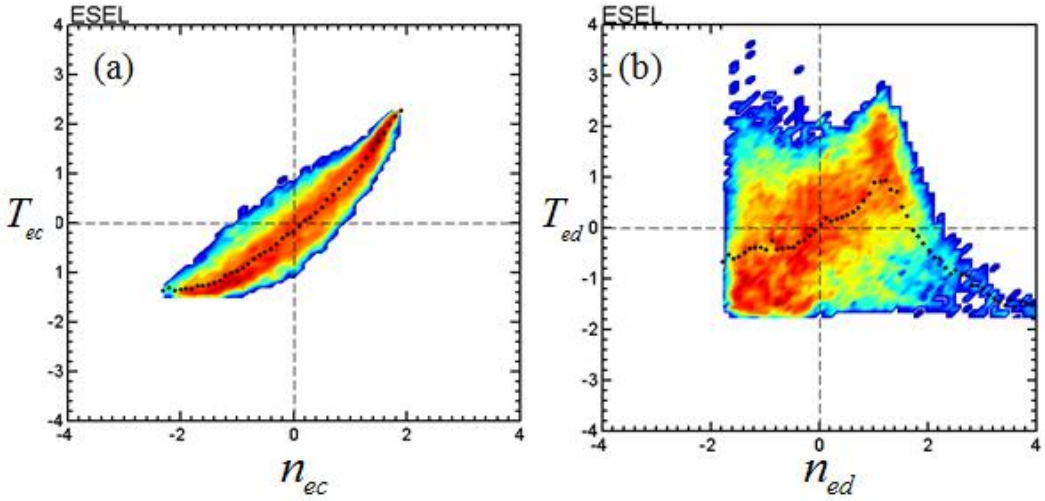

Figure 3.26. (a) The combined PDF of electron density fluctuations and electron temperature fluctuations in middle SOL plasma measured by a single probe in ESEL simulation, (b) The combined PDF of electron density fluctuations and electron temperature fluctuations in middle SOL plasma determined by the dedicated probe array in ESEL simulation. The black dots demonstrates the statistical average of the PDF of electron density fluctuations and electron temperature fluctuations.

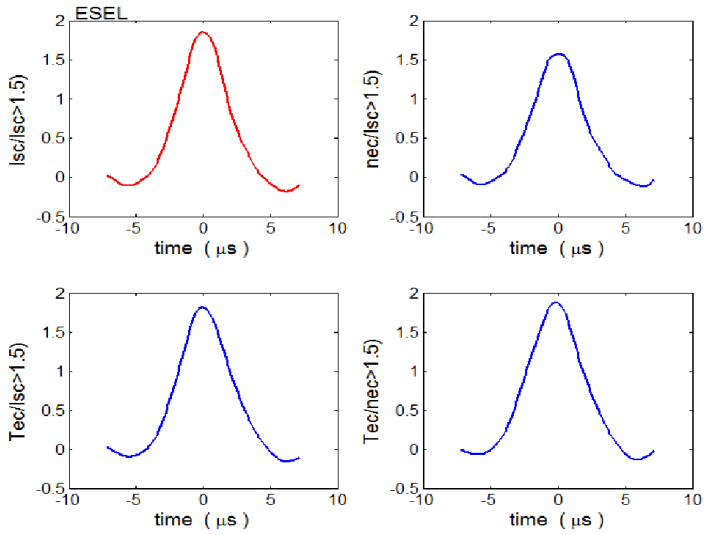

Figure 3.27. Conditionally averaged waveforms of (a) I_{sc} fluctuations triggered by the I_{sc} peak, (b) n_{ec} fluctuations triggered by the I_{sc} peak, (c) T_{ec} fluctuations triggered by the I_{sc} peak, (d) T_{ec} fluctuations triggered by the n_{ec} peak. The data are acquired at the middle SOL in ESEL simulation.

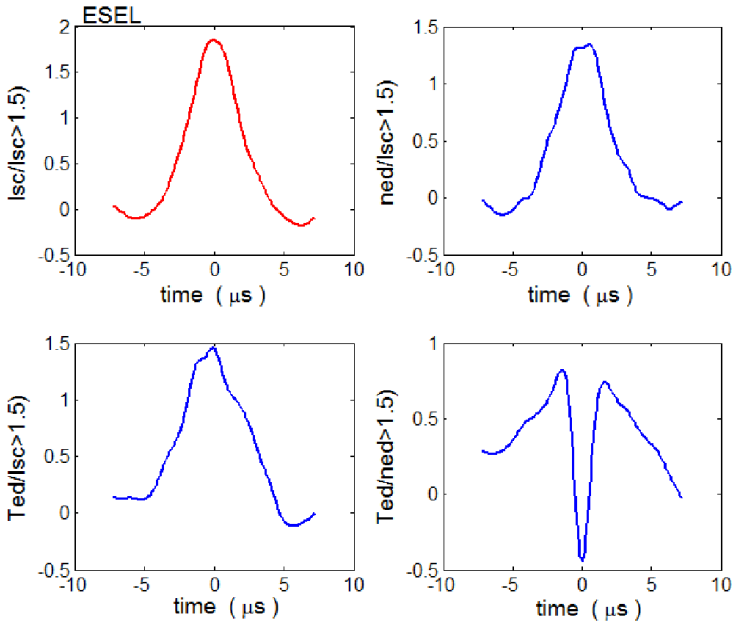

Figure 3.28. Conditionally averaged waveforms of (a) I_{sc} fluctuations triggered by the I_{sc} peak, (b) n_{ed} fluctuations triggered by the I_{sc} peak, (c) T_{ed} fluctuations triggered by the I_{sc} peak, (d) T_{ed} fluctuations triggered by the n_{ed} peak. The data are acquired at the middle SOL in ESEL simulation.

As shown in figure 3.26, the combined PDF of actual electron density fluctuations and electron temperature fluctuations in ESEL simulation show a strong linear dependence. It occupies mainly the first and the third quadrants. The

intermittent density bursts are supposed to possess higher electron temperature. However, the combined PDF of electron density fluctuations and electron temperature fluctuations measured by artificial probes are more dispersive in all the four quadrants. The intermittent density coherent structures with high amplitude ($n_{ed}>2\sigma$) are of depletive temperature than the surrounding plasma. The conditionally averaged waveforms of electron temperature triggering by the density threshold can explicitly demonstrate the topology of electron temperature inside the blobs. As shown in the figure 3.27, the ESEL simulation predicate that the intermittent density bursts (blobs) are of higher temperature than the background turbulence. Nevertheless, indicated by figure 3.28, the measurements using the artificial probe array show that the temperature of blobs is much lower than the background turbulence. It contradicts the direct observation of coherent structures in ESEL simulations. The separation of the probe tips result in technical error during the measurements of Langmuir probe array. The poloidal correlation coefficients of a plasma parameter (density, electron temperature, floating potential, plasma potential) estimated in the ESEL simulation are shown in figure 3.29 . It is found that the spatial scale size of the turbulence is larger than the probe separation (4mm). This doesn't agree with our conjecture from the experimental measurements, where the measuring error take place when the spatial size of blobs is smaller than the probe separation. The detailed mechanism for the effecting probe measurement is not clear here yet. However, both the experiment and simulation show that the probe separation definitely gives their influence to the probe measurements.

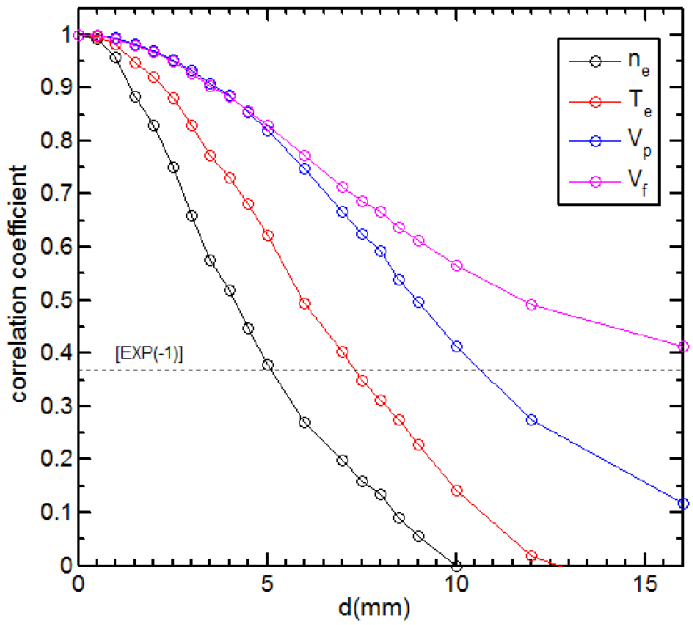

Figure 3.29. The variation of correlation coefficient with the distance of poloidal separation between two identical probes detecting same plasma parameters, plasma density n_e, electron temperature T_e, plasma potential V_p and floating potential V_f.

3.6. Geodesic acoustic mode

Turbulence shear suppression by E × B flows at the edge is believed to be the leading mechanism responsible for the confinement improvement of fusion plasmas L-H transitions. Spontaneous E × B shear flows are widely recognized recently in the fusion devices. They are generated from ambient plasma turbulence through energy transfer due to nonlinear coupling of turbulence. The process is analogous to the generation of large scale zonal flows which have been ubiquitously observed in the nature. zonal flows has attracted great interest owing to their essential role in the turbulent transport in the magnetically confined plasma.

Specifically, zonal flows (ZF) in plasma are time-varying poloidal E × B shear flows generated from turbulence, which are characterized by toroidally and poloidally symmetric potential structure with finite radial wavelength in tokamak plasmas [113, 114]. The radial shearing of zonal flows can break up the turbulence eddies and reduce the cross-field transport, thus it is of great interest in the fusion plasma. Two kinds of zonal flows have been identified so far in magnetically confined plasmas: the near zero low-frequency ZF and the oscillatory flows termed geodesic acoustic mode (GAM). Besides the axisymmetric ($m = n = 0$) potential structure as in low-frequency ZF, the GAM oscillations are expected to have a ($m = 1$, $n = 0$) density structure due to the pressure asymmetries on a flux surface induced by nonuniform E × B flows in tokamak. The GAM induced density and the radial electric field fluctuations have been identified widely in the edge plasma of tokamaks [114-122]. GAMs are not typically observed in H-mode plasma but are nearly always present in Ohmic and L-mode plasmas.

In detail, ZF is faster on the outboard side of the torus and slower on the inside due to the asymmetries of the toroidal magnetic field. The divergence of zonal flows create a pressure source and sink on the top and bottom of the torus. The coupling local compressible E×B flows and pressure sidebands leads to the GAM oscillation varying with poloidal angle. The GAM generation can be depicted in a fluid model with the following equations:

$$\begin{cases} \dfrac{\partial \tilde{\rho}}{\partial t} = \nabla \cdot [-\rho \dfrac{\tilde{E}}{B}] + \nabla \cdot [\rho \tilde{\mathrm{V}}_{//}] & (3.7a) \\ \rho \dfrac{\partial \tilde{V}}{\partial t} = -\nabla \tilde{P} + J \times B & (3.7b) \\ \nabla \cdot J = 0 & (3.7c) \\ \rho \dfrac{\partial \tilde{V}_{//}}{\partial t} = -\nabla \tilde{P}_{//} & (3.7d) \end{cases}$$

The plasma mass density perturbations are denoted with $\tilde{\rho}$, and pressure perturbation $\tilde{P}$, velocity perturbation $\tilde{\mathrm{V}}$, plasma current J, magnetic field B. The pressure perturbations and mass density perturbations are related by ion sound speed C_s. Perpendicular current $J_\perp$ is composed of the polarized current and diamagnetic current.

$$\begin{cases} \dfrac{\nabla\tilde{P}}{\nabla\tilde{\rho}} \approx C_s^2 & \text{(3.8a)} \\ J_\perp = \dfrac{\partial}{\partial t}[-\rho\dfrac{\tilde{E}}{B}] + \dfrac{\nabla_\perp \tilde{P}}{B} & \text{(3.8b)} \end{cases}$$

In order to satisfy the quasi-neutrality of plasma, a radial current will be exited to balance the perpendicular current. Thus, GAM generation process essentially undergo a oscillating perturbation of the radial electric field. The frequency of GAM oscillation ω_{GAM} derived from above equations is,

$$\omega_{GAM} = \sqrt{\frac{C_s^2}{R^2}(2+\frac{1}{q^2})} \qquad (3.9)$$

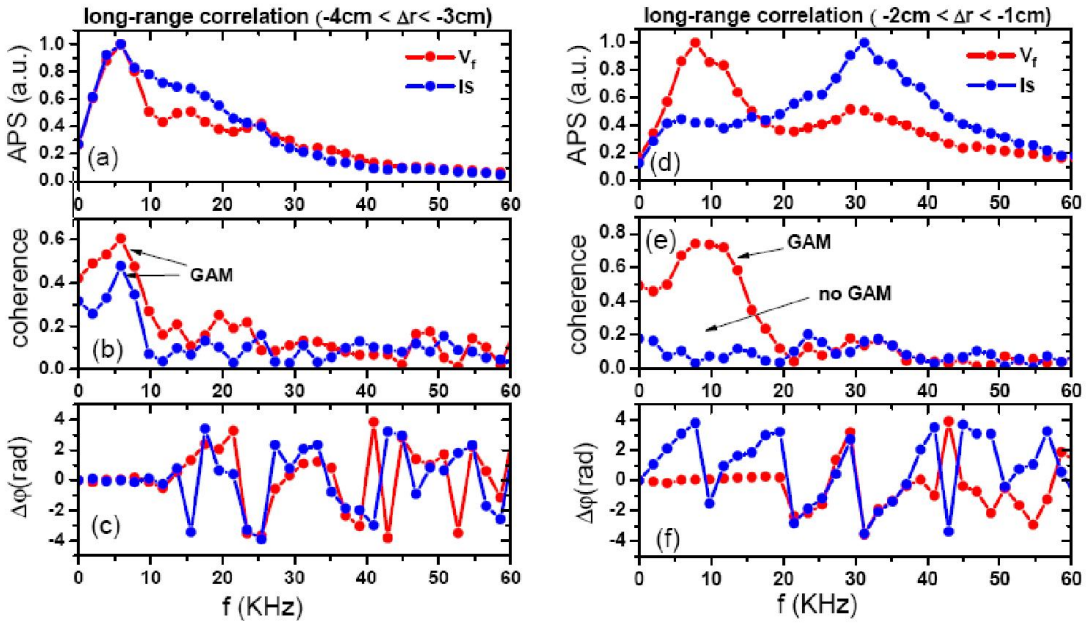

Figure 3.30. Long-range correlation analysis at the region (left panels: -4cm <△r <— 3cm) and (right panels: -2cm <△r <— 1cm). (a) (d) Auto Power Spectra (APS) of the floating potential V_f, ion saturation current Is. (b) (e) Long-range coherence between V_f, as well as Is measured by the probes toroidally separated by 89°. (c) (f) Phase difference between the V_f, as well as Is measured by the probes toroidally separated by 89°.

On EAST, synchronous probe measurements at port A and port E provide unique capabilities in allowing the investigation of a large scale zonal/GAM flows. Figure 3.30 shows the Long-range correlations of edge turbulent plasma fluctuations respectively in V_f and I_s signals obtained in discharge #22111. The Long-range correlations are applied here in two different region of edge plasma which locate inner side of the edge shear layer (left panels of figure 3.30: -4cm <△r <-3cm) and outer side of the edge shear layer (right panels of figure 3.30: -2cm <△r <-1cm), respectively.

As shown in figure 3.30 (a), a dominant frequency f_{peak}~5-7kHz can be identified in the power spectrum of floating potential V_f and ion saturation current Is signals. It is well consistent with the theoretical predicted GAM frequency, f_{GAM}~$C_S/2\pi R$~4-7 kHz, where the C_S and R resents the ion sound speed and major radius of the device, respectively [113, 114]. Furthermore, the long-range correlations analysis depicted in figure 3.30 (b) shows that both the plasma potential V_f and ion saturation current I_s exhibit a pronounced long-range coherence around above mentioned dominant frequency f_{peak}, which strongly indicate a characteristic of GAM. Moreover, as can be seen in figure 3.30 (c), the phase difference between plasma potentials V_f as well as ion saturation currents I_s are zero around f_{peak},. Thus, all the above observations indicate a signature of GAM in the edge plasma of EAST. The eigenfrequency of GAM locate nearby f_{peak}. In figure 3.30 (d) (e) (f), the same long-range analysis is applied to the turbulent fluctuations outside of the edge shear layer (-2cm <Δr <-1cm) . The dominant frequency of floating potential f_{peak} shifts to 5-10 kHz due to the lower plasma temperature in this region. The long-range coherence and zero phase delay between floating potentials measured at the two toroidal locations manifest the underlying activity of GAM. Interestingly, the GAM are not detected in the I_s fluctuations in this region (-2cm <Δr <-1cm). Different to the turbulence inside the shear layer, a dominant frequency f_{peak} ~30kHz becomes remarkable in I_s fluctuations as well as in V_f fluctuations, which was suspected as the local drift wave turbulence, since the plasma profile show a steep gradient in this region. The reason for the absence of density sidebands of GAM oscillations outside the edge shear layer of EAST is still not clear in this work. The scaling of the GAM frequency on the term $C_S/2\pi R$ are made in our measurements. As shown in the figure 3.31, the GAM frequency increased monotonically with $C_S/2\pi R$. The linear coefficient of the scaling was estimated to be 1.8, which is very close to the theory predicted coefficient.

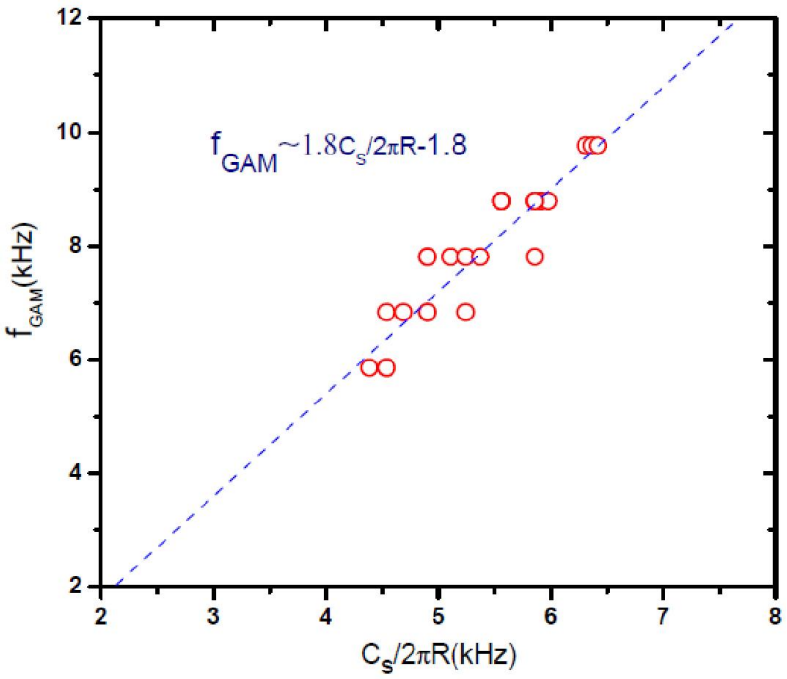

Figure 3.31. Scaling of the GAM frequencies in the experiment

3.7. Parallel SOL flows on EAST

Plasma flows plays an important role in the plasma transport and significantly influence the particle and energy exhaustion in the SOL. Particle drift is believed to be a basic contributor for the plasma flows. The stream of classical E×B and ▽B drifts depends on the direction of toroidal magnetic field, which offers the fundamental explanations for poloidal up-down asymmetry. E×B drifts are stronger than the ▽B drifts since the former scales inversely with the SOL plasma scale length *L* while the later scales inversely with major radius *R*. The E×B and diamagnetic flow drifts cross the magnetic field and the isopressure surfaces, the plasma will be supplemented by Pfirsch-Schliiter (P-S) flow [123] parallel to magnetic field to satisfy the continuity equation. Besides, poloidal transport asymmetries will pose a ballooning flow along the magnetic field. A sharp density gradients are created at the surface of divertor plate due to plasma-neutral interaction and impurity ionization. It turns to provide a large particle sources for the sink flow to the divertor, impacting the in-out asymmetry.

The SOL flow at various poloidal locations has been measured in many divertor tokamaks [76, 124-127]. Most of the experimental results are obtained by Mach probes. A number of possible mechanisms to drive the parallel SOL flow have been suggested, including ion Pfirsch-Schlüter flow, ballooning transport, flow reversal driven by localized ionization, momentum transfer, and co-current toroidal momentum generated in the SOL by ion ▽B and centrifugal drifts [78]. There are

some experimental evidences that the Pfirsch-Schlüter flow appears to make an important contribution to the observed parallel flow, because the direction of the parallel flow is reversed when the magnetic field is reversed [128, 129]. Meanwhile, it has been demonstrated by the measurements of the SOL flow in different divertor configurations at both HFS and LFS in Alcator C-Mod tokamak [78, 126] that a ballooning-like transport is the most important contributing mechanism to the asymmetry in the HFS-LFS SOL flow, albeit some other mechanisms, including toroidal plasma rotation and Pfirsch-Schlüter ion currents. Additionally, drift flow in the private flux region is identified to be a important mechanism that produces in–out asymmetry in the divertor particle flux [130, 131]. A variety of flows and their dependence on the direction of toroidal magnetic field are illustrated in the figure 3.32.

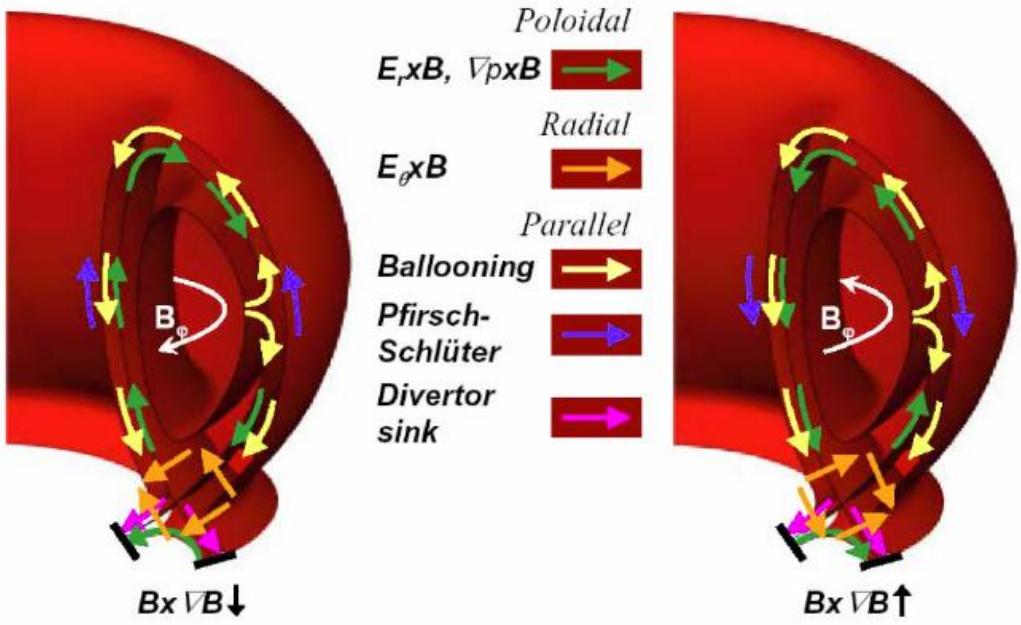

Figure 3.32. Various flows present in tokamak with normal magnetic field (ion ▽B drift towards the X-point and reversed magnetic field (ion ▽B drift away from the X-point).

The parallel SOL flows are investigated at the mid-plane by the Mach-probe array in EAST tokamak. The measurements are obtained with different magnetic configuration, including double null divertor configuration and limiter configuration along with normal toroidal field at varying line averaged density n_{el}, from 0.5×10^{19} m^{-3} to 3.5×10^{19} m^{-3}. As can be seen in figure 3.33, it is found that the SOL parallel flow at the position ($\Delta r = 10mm$) has a strong dependence on the plasma density. There is a clear decrease in the flow magnitude as the plasma density increase. Furthermore, the parallel flow has the flow direction against ion B ×▽B direction in

the experiment. From the evidence above, Pfirsch-Schlüter flow could potentially be a candidate to explain the SOL flow near the outboard mid-plane of EAST.

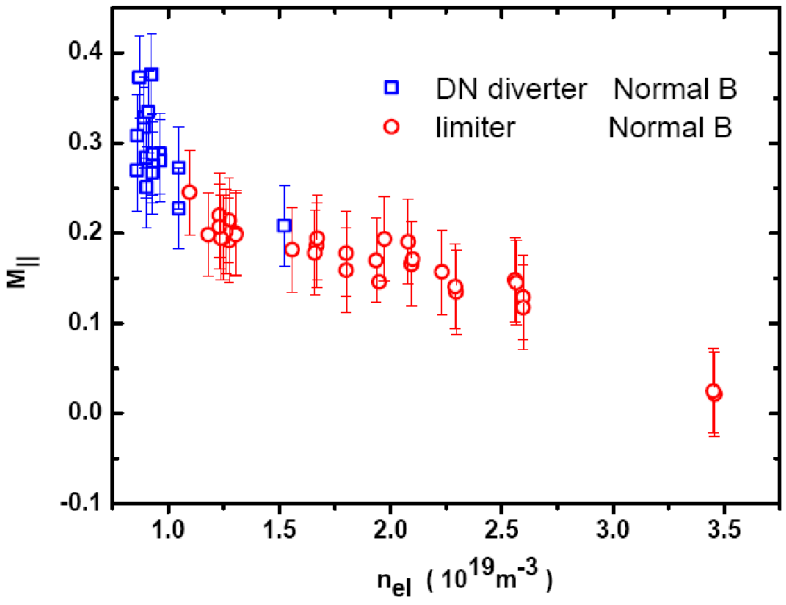

Figure 3.33. Dependence of parallel Mach number magnitude on the line averaged density, measured at the position ($\Delta r = 10mm$).The error bars represent one standard deviation of the experimental data.

From a theoretical point of view, a simple analytic approximation does exist for SOL P-S flows in the large aspect ratio, cylindrical approximation [129]:

$$\mathrm{M}_{//}^{PS} = \frac{2q\cos\theta}{C_s}(E_r - \frac{\nabla p_i}{en}) \times \frac{\vec{B}}{B^2} \qquad (3.10)$$

Here, q is the safety factor. E_r and ∇p_i are the radial electric field and ion pressure gradient, which can be derived from the profile of plasma potential and ion pressure, assuming $p_i \approx p_e$. P–S currents in the edge plasma are usually smaller than in the SOL, since radial gradients of plasma potential and pressure are larger in the SOL. On the other hand, the E_r and ∇p_i cancel each other in the edge plasma but reinforce each other in the SOL.

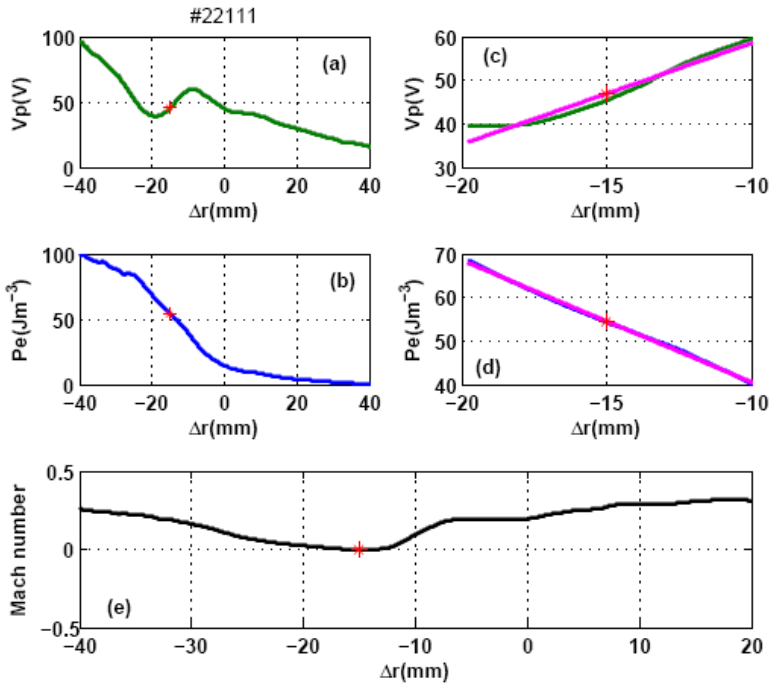

Figure 3.34. Original profile of (a) plasma potential and (b) plasma pressure, linear fitted profile (pink line) of (c) plasma potential and (d) plasma pressure; (e) Experimental measured parallel Mach number profile (red mark at $\Delta r = -15mm$).

As is shown in the figure 3.34 (c) and (d), we fit the profile of plasma potential and pressure with linear function y=*ax*+*b* (pink line). In this way, the terms E_r ~-2.4kV/m and - $\nabla p/en_e$ ~ 1.8 kV/m could be obtained, as well as local ion sound speed. It is worth commenting the nearly zero parallel flow appear in the range -20mm<Δr < -10mm , where the E_r and - ∇p are in the opposite directions. Out of this region, the parallel flows arise when E_r and - ∇p point to the same direction. Empirically, the fading of parallel flow components may ascribe to the cancellation between the ion diamagnetic flow and E×B drift. Thus, we believe the P-S flow significant affect the parallel flow pattern in the EAST edge. As the data inside the separatrix is limit in the experiment, further statistical results are obtained in the SOL.

It is well known the ions is significant hotter than electrons in the SOL plasma (i.e. $T_i > T_e$), and the SOL ion temperature decay length tends to be larger than the electron temperature decay length (i.e. $\lambda_{Ti} > \lambda_{Ti}$, where the $\lambda_{Ti,e}=T_{i,e}/|\nabla T_{i,e}|$) [132]. Since the ion temperature can't be measured by Langmuir probe, we simply assume here that the $T_i \approx 2T_e$ and $\lambda_{Ti} \approx 1.5\lambda_{Te.}$ according to the knowledge obtained in other tokamaks [93, 132-136]. θ is the poloidal angle. In this work, these values are available in outboard mid-plane by probe measurements on EAST, i.e. the measurements in this section are considered as θ≈0. The comparison between the SOL parallel flows and predicted P-S flows are demonstrated in figure 3.35 .

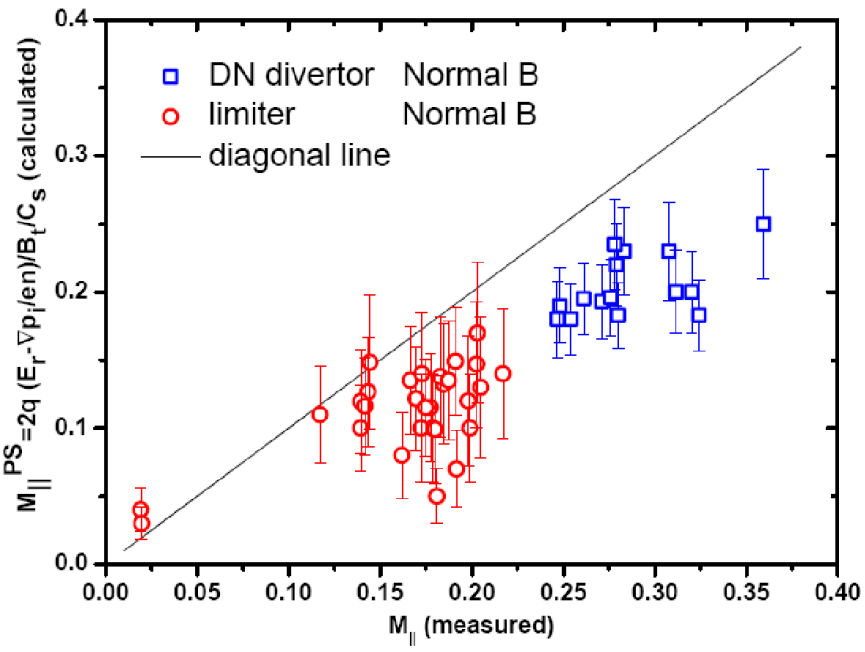

Figure 3.35. Comparison between the theory predication and the experimental measurement at the radial position ($\Delta r = 10mm$).The error bars represent one standard deviation of the experimental data.

As is shown in the figure 3.35, the magnitude of parallel flow $M_{//}$ measured from different plasma discharges are about 30%-50% larger than the theoretical predicted P-S flows $M_{//}^{PS}$. It should be stressed here the invalid assumption $T_i \approx T_e$ and $\lambda_{Ti} \approx \lambda_{Te}$ can lead to an overestimation of $M_{//}^{PS}$ which are comparable with $M_{//}$ on EAST. To the contrary, the estimated $M_{//}^{PS}$ could be even lower with a larger prescribed T_i and λ_{Ti}. Therefore, even though there are some uncertainties on the ion temperature profile in the SOL plasma of EAST, it could be qualitatively recognized that Pfirsch-Schlüter flow is potentially an important components but can't be fully responsible for the parallel plasma flow at the outer mid-plane in the Ohmic discharge of EAST.

Chapter 4

H-mode physics

4.1. outline of H-mode plasma in EAST

In 1982, the first H-mode plasma was achieved with neutral beam injection (NBI) heating in divertor discharge of the ASDEX tokamak [137]. Afterwards, the H-mode was frequently reproduced in other tokamaks, as well as stellarators [138]. It is characterized by a sudden drop of $H_\alpha(D_\alpha)$ signal in the SOL divertor, signifying the degraded transport and improved confinement. The confinement time of H-mode plasma is usually higher than it of L-mode plasma by a factor of 2. The most remarkable feature of H-mode plasma is the formation of edge pedestal which exhibits a sharp steep plasma gradient. Edge turbulence and resultant transport are found significantly depressed in the pedestal region. The stationary H-mode is a attractive regime for fusion energy.

Figure 4.1 shows the initial the H-mode obtained on EAST. In the H-mode, the confined density and stored energy are suddenly enhanced. The radiation energy loss of plasma strengthen correspondingly. Neutron product become more active due to the elevated plasma temperature. The primary indicator for the improved confinement in H-mode is the drop of $H_\alpha(D_\alpha)$ signal, which directly results from the reduction of plasma outflow into the SOL.

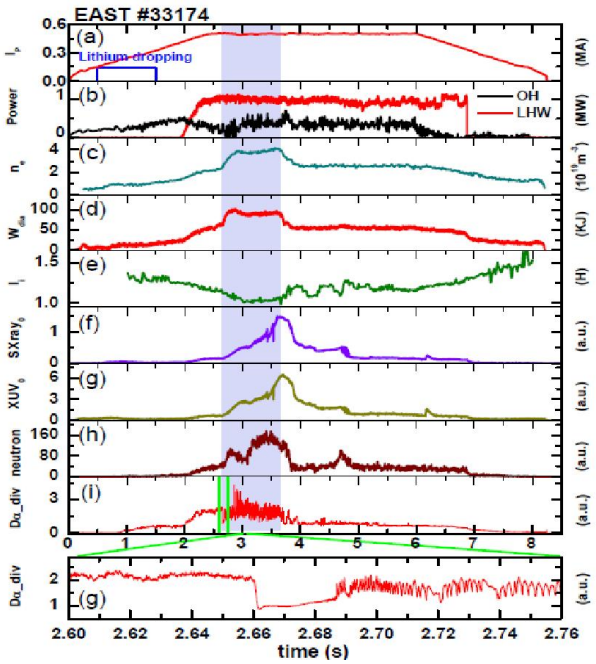

Figure 4.1. Time evolution of a H-mode shot: (a) plasma current I_p, (b) LHCD injection power P_{LHW}, Ohmic heating power P_{OH}, (c) central-line-average density n_e, (d) stored energy W_{dia}, (e) internal inductance l_i, (f) soft x-ray radiations at core plasma, (g) XUV radiations at core plasma, (h) neutron flux, (i) Divertor D_α emission and its zoom plot (g).

The H-mode are commonly attainable when the heating power into plasma exceeds a certain threshold P_{th} irrespective of the magnetic configuration, size of the devices and the heating schemes. The remarkable universality of such phenomena in toroidal plasma devices suggests a unified theory explanation behind. Understanding of the H-mode might provide a key to utilizing the fusion reactor. Regrettably, the mechanism that trigger H-mode is still not fully understood over past three decades. However, Increasing empirical insight have been gained in the H-mode experiments of multiple machines. Some important features are indicated below:

1) The H-mode transition take place at a minimal heating power P_{th}.

2) The power threshold of L-H transition is higher than it in H-L transition, i.e. $P_{L\text{-}H}>P_{H\text{-}L}$. The forward transition to H-mode and the back transition to L-mode in tokamaks exhibits hysteresis in the heating power.

3) The power threshold for L-H transition in limiter configuration is higher than in divertor configuration.

4) In divertor plasma, the P_{th} depends on the direction of $B\times\nabla B$. The divertor plasma with $B\times\nabla B$ direction away from the X-point require higher heating power to trigger the H-mode than with $B\times\nabla B$ direction pointing to the X-point.

5) P_{th} depends on the isotopic mix of working gas.

6) The clear plasma will lower the P_{th}.

Detailed dependence of P_{th} are explored in a variety of plasma parameter. Among them, plasma density, strength of toroidal magnetic field, and plasma surface area are primary factor for the H-mode triggering. A empirical scaling on P_{th} are derived from multiple devices [139]. It reads

$$P_{th} = 0.0488 n_{e20}^{0.72} B_t^{0.8} S_A^{0.94} \qquad (4.1)$$

where n_{e20} is the line-averaged electron density at the L-H transition in $10^{20}\,m^{-3}$, B_t is the magnetic field in Tesla and S_A is the plasma surface area in m^2. However, the power threshold does not linearly depend on the plasma density. This international scaling is only valid above a threshold density n_{min}. Magnitudes of P_{th} are found to increase when the density below the n_{min} [140, 141]. The scaling of P_{th} and density shows a U-like shape. The P_{th} exhibits a local minimum at density n_{min}. This phenomenon is termed density rollover. The low density regime is a big concern for ITER, since ITER will be operated in the low-density range.

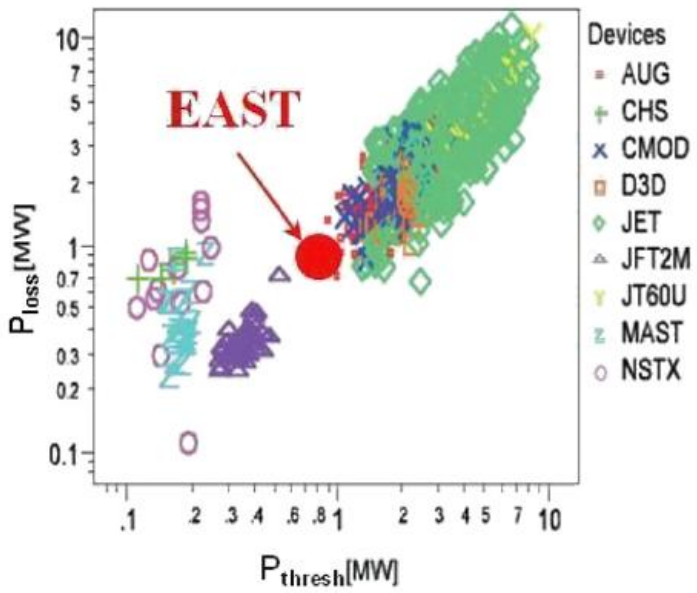

Figure 4.2. Threshold power for the EAST LHCD H-modes, which agree well with the predictions of the international tokamak scaling.

The initial H-mode is achieved by LHCD heating alone on EAST. The heating power across the separatrix are estimated as $P_{loss}=P_{OH}+P_{LHW}-P_{rad}-dW_{dia}/dt$, where P_{OH} presents the Ohmic heating power, P_{LHW} the lower hybrid wave heating power during the measurements. P_{rad} is the radiation power, dW_{dia}/dt denotes the time variation of stored plasma energy confined in the tokamak. As indicated in figure 4.2, the P_{loss} at the L-H transition is agree well with the power threshold predicted by the international tokamak scaling. Extrapolation of the energy requirement for L-H transitions based on the present experiments provide a crucial implication for operation of future reactor. The L–H transition physics has attracted substantial interest in fusion research. Some theoretical works and numerical simulations devote their efforts to shed lights on the understanding of H-mode transition [142-145]. Great steps forward has been made on different aspects to interpret H-mode triggering and the power threshold scaling. However, the comprehensive explanation are still not in place due to many sophisticated factors behind L-H transitions.

The transition were observed to be affected by many factors—edge E_r shear layer [20], zonal flow [146], neutral particles [147, 148], X-point height [149, 150], wall effect [151, 152], ion mass number [153] and so on. Decisive variables responsible for L-H transition are still elusive in the existing database. An impressive 'wall effect' are worth mentioned here as a milestone of H-mode achievement on EAST. To access the H-mode, extensive lithium wall coating was employed to reduce recycling and suppress oxygen impurities in EAST [154]. With the increasing

deposition of lithium on the vessel walls, the duration of the H-mode was progressively prolonged to the entire duration of the plasma current flat top. Simultaneously, the neutral density near the lower x-point was reduced by a factor of 4 with increasing Li accumulation. The neutral density was suggested as the dominant 'hidden variables' behind the L-H transition on EAST, since the radial electric field at the plasma edge are possiblely modified via neutral-ion charge-exchange momentum losses. With the increase of lithium deposition, the H/(D+H) ratio was gradually reduced from ~50 to ~7% in deuterium plasma. The lower H/(D+H) ratio could also lower the power threshold and optimize ICRF heating efficiency.

Figure 4.3 shows the variation tendency of plasma stored energy, and required heating power for H-mode transition, D_α/H_α emission along with the Li accumulation. A clear drop in the D_α/H_α emission suggests a improved confinement with the application of lithium coating. The intensive use of lithium directly reduced the heating power for H-mode triggering and enhanced energy confinement in plasma.

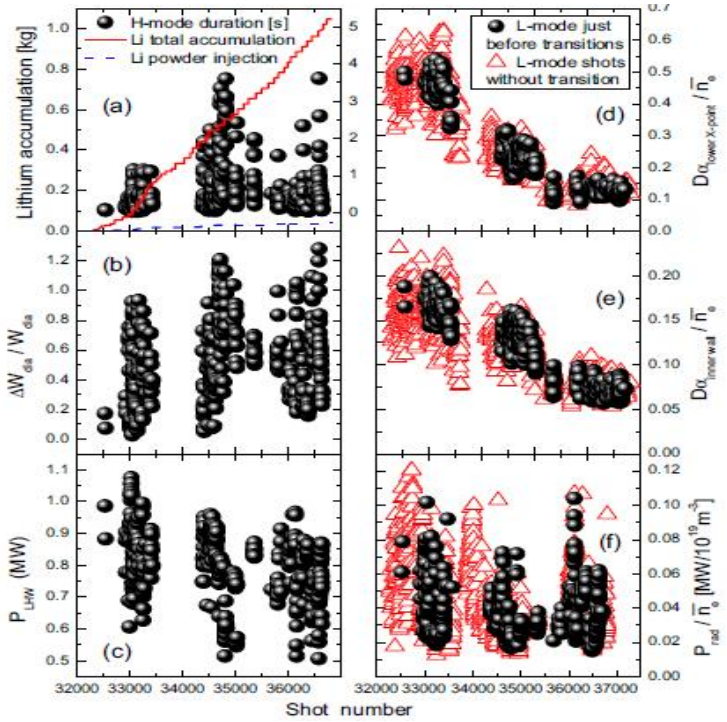

Figure 4.3. (*a*) Li total accumulation (solid line), Li power injection amount (dashed line), H-mode durations (points), (*b*) relative increment of stored energy during *H* phase, (*c*) injected LHW power at L–H transitions in the H-mode shots with I_p = 0.5–0.6 MA, (*d*) D_α/H_α emission near the lower X-point, (*e*) D_α/H_α emission near the inner wall, (*f*) total radiation power, divided by central-line-average electron density on EAST tokamak, with points for L-mode periods just before L–H transitions, and triangles for L-mode shots without L–H transition[154].

4.2. Signature of Zonal flows at L-H transition

The H mode is one of the most promising regimes of enhanced confinement for future fusion devices. However, the mechanism of L-H transition is a big mystery since the discovery of H-mode. To minimize the uncertainty in the threshold power prediction for ITER, the improved understanding of L-H transition is derisible.

Among many alternative explanations, E×B flow shearing at the plasma edge are believed to play a key role to eliminate the turbulence and trigger the H-mode. This shear suppression can occur by mean E×B flows and/or by zonal flows. Mean E×B flows are driven by mean pressure gradient and poloidal and toroidal flows, whereas zonal flow arises from the turbulence by extracting free energy there. At the marginal input power, the mean E×B flow is most likely not sufficiently strong for a transient L-H transition. In this case, zonal flow are of great importance to reinforce the E_r shear. A predator-prey-type competition between turbulence and zonal flows leads to limit-cycle oscillation form of L-H transitions, which have been predicated in the simulations [146] . In this section, we present our observations on the zonal flows at the L-H transitions by probing inside the edge plasma on EAST.

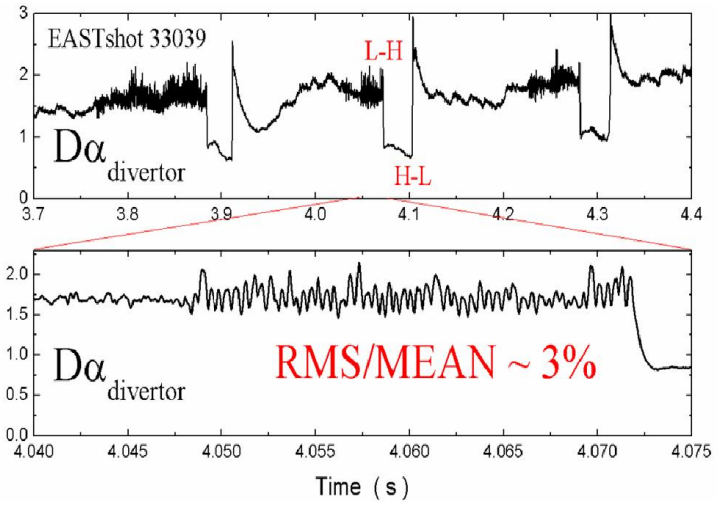

Figure 4.4. Oscillation in divertor D_α emission which is frequently observed just before the L-H transition or sometimes in the L mode (a) Multiple L-H-L transitions in one shot, (b) Zoom-in plot of dithering in (a).

Figure 4.4 show the time trace of divertor D_α emission signal, which indicates a sequence of three L-H transitions. A clear oscillation in D_α at a frequency ~2kHz were uniformly observed just before these transitions. It initializes several tens of milliseconds before the L-H transitions, and the oscillation amplitude slowly increases when approaching the transition. The relative fluctuation level of the D_α oscillating is about 3%. Since this phenomenon take place just preceding the L-H transition. it may

provide a key information for our understanding on L-H transitions.

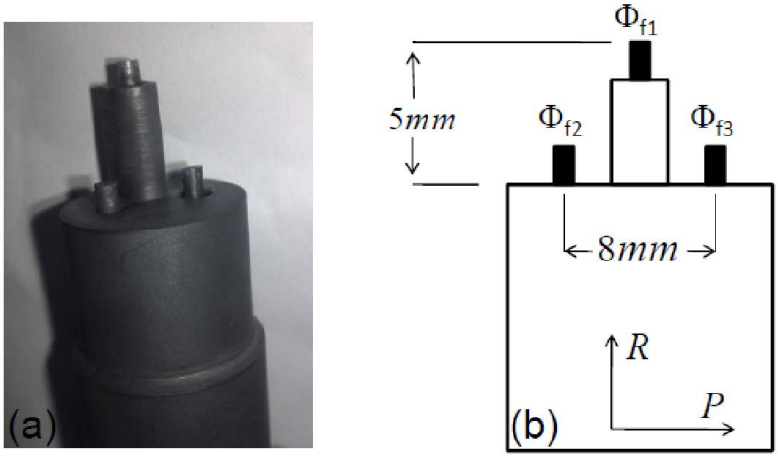

Figure 4.5. (a) Picture of the Reynolds stress probe array, which consisted by pins measuring floating potential Φ_{f1}, Φ_{f2} , Φ_{f3}. (b) Side view of Reynolds stress probe array.

To understand the underlying physics behind the D_α oscillating, a Reynolds stress probe head were used to make a measurement inside the separatrix (~1cm) during the L-H transitions. The Reynolds stress probe array (figure 4.5) is consisted by pins measuring floating potential Φ_{f1}, Φ_{f2} , Φ_{f3}. The two tips Φ_{f2} , Φ_{f3} are poloidally separated by dp=8 mm. The third tip (Φ_{f1}) radially stick out by dr = 5 mm than Φ_{f2} and Φ_{f3}, and it locate 5mm away from the middle of Φ_{f2} and Φ_{f3} in toroidal direction to avoid the shield on Φ_{f2} and Φ_{f3}. Neglecting the temperature fluctuations, the radial electric field are calculated as E_r=(Φ_{f1}-(Φ_{f2} + Φ_{f3})/2)/dr. Poloidal electric field are deduced as E_p= (Φ_{f2} - Φ_{f3})/dp. The radial E×B drift velocity V_r and poloidal E×B drift velocity V_p can be determined simultaneously with Reynolds stress probe.

The Reynolds stress is defined as [155]:

$$\mathrm{R}s = \left\langle V_r V_p \right\rangle \qquad (4.2)$$

Where sharp brackets < > denote an ensemble average. Reynolds stress is a measure of the anisotropy of the turbulent velocity fluctuations, since it is generated solely from inhomogeneous correlations between V_r and V_p. It is a driving term in the momentum equation of shear flow [113].

$$\frac{\partial V_p}{\partial t} = -\frac{\partial}{\partial r}\left\langle V_r V_p \right\rangle - \mu V_p \qquad (4.3)$$

The first term on the right-hand side of above equation is identified as the divergence of the Reynolds stress and it can generate the poloidal flow. Anisotropic

velocity fluctuations produce a stress on the mean flow. It will cause an acceleration of the flow in the plasma and transform the moment into the poloidal flow. A self-consistent explanation of the flow generation is that the divergence of the Reynolds stress can be seen as a flux of charge due to the nonlinear polarization drift this creates a radial electric field which combined with toroidal magnetic field generates a poloidal flow.

Figure 4.6 (a) shows the raw signal of floating potential measured during the D_α oscillating phase before L-H transition. As indicated by the floating potential Φ_{fl}, a quasi-periodic suppression of turbulent fluctuations take place accompany with the D_α oscillation. The envelope of the turbulent fluctuations ϕ_f^{flu} is calculated using the Hilbert transform of the high-pass-filtered potential fluctuations at a frequency over 10 kHz [156, 157], where turbulence dominates the spectral. It drops when the radial electric field E_r and poloidal E×B flow shear rate ω_{shear} rise. In particular, the time variation of E_r is well correlated with the evolution of turbulence-driven Reynolds stress. It is suspected that the enhanced E×B flow shear suppress the local turbulence and abate the turbulence transport, which could be responsible for the D_α drop. Remarkably, the local turbulence decorrelating rate τ_c^{-1} is at marginal balance with the E×B flow shear rate ω_{shear} when the turbulence suppression occurs, where τ_c is defined as turn over time of local turbulent eddy. Thus, the behavior of observed E_r modulation well coincide with the appearance of turbulence-driven zonal flow.

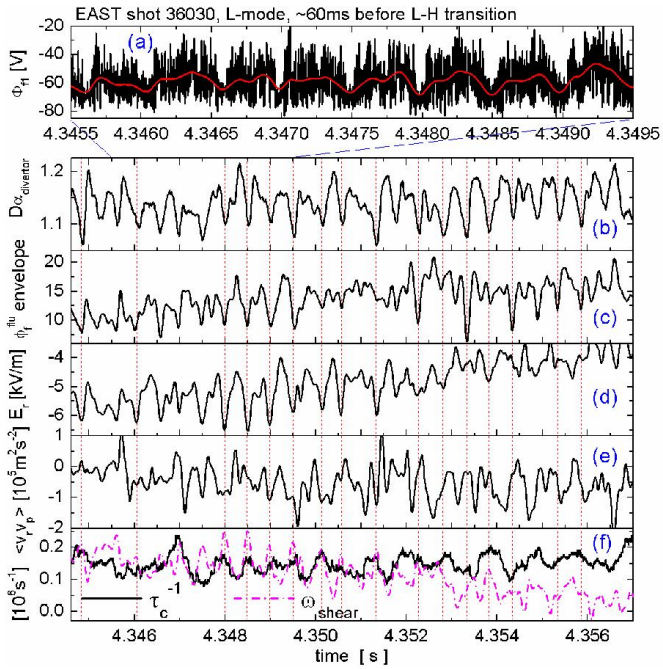

Figure 4.6. (a) Raw data of the floating potential ϕ_{fl} and its low-frequency component, <5 kHz, (b) The D_α emission near the inner target, (c) The ϕ_{fl} fluctuation envelope, (d) The radial electric field, (e) The turbulent Reynolds stress, (f) The turbulence decorrelation rate τ_c^{-1} and the local $E_r \times B$ shearing rate ω_{shear}.

From our observations, a signature of zonal flow is identified preceding the L-H transitions in our measurements. The turbulent fluctuations and transport in the pedestal are regulated by such zonal flow-like E_r oscillation at a frequency of 2 kHz.

4.3. Multiple transient L-H-L transitions

Some transient L-H transitions are frequently observed far before plasma enter into a stable H-mode on EAST. As shown in the figure 4.7, a prominent L-H transition take place at 5.48s indicated by the vertical red line. It is characterized by a abrupt drop of D_α emission level and better confinement of particle and energy. A remarkable edge pedestal established in the radial position ρ==0.92, which is manifested by the enhanced extreme ultra-violet (XUV) radiation there. The effective input power of LHCD decrease in the H-mode plasma due to the reinforced reflection power. Before this prominent L-H transition, nine scattered transient L-H-L transitions are observed before the time 5.48s. They appear irregularly before the confinement get improved. The dynamics of these transient L-H-L transitions may carry important implication for the understanding on the mechanism of L-H transitions.

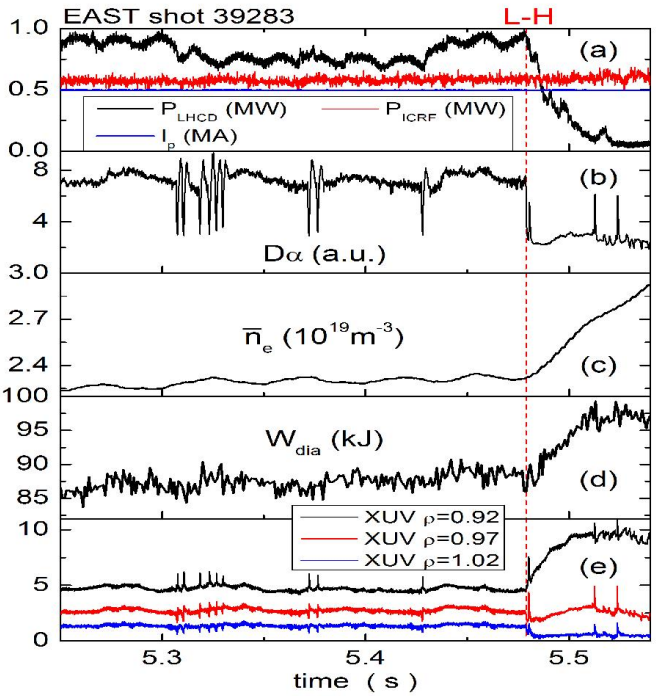

Figure 4.7. The time trace of (a) LHCD, ICRF input power and plasma current, (b) divertor D_α emission, (c) central-line-averaged density, (d) plasma stored energy, (e) XUV radiations at different location in the plasma edge.

To investigate the dynamics of multiple transient L-H-L transitions, a two steps probe array are used here to catch the evolution of edge turbulence 0.5cm inside the separatrix. The Reynolds stress probe array is consisted by two pins measuring floating potential ϕ_{f1}, ϕ_{f2}. The tip ϕ_{f1} is mounted radially inward than tip ϕ_{f2} by a distance dr=5 mm.

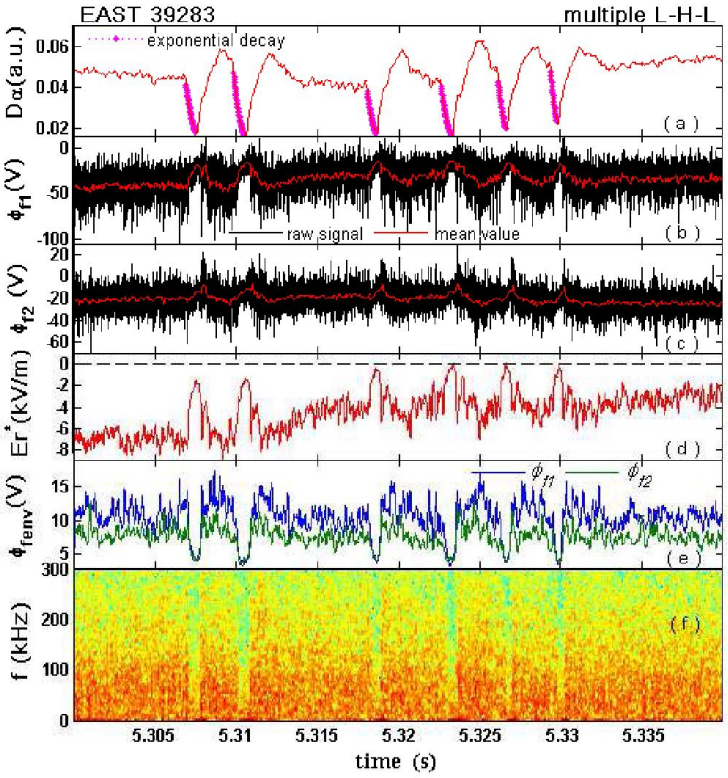

Figure 4.8. Signal evolution in multiple L-H-L transitions. (a) D_α signal at lower outer divertor, the decay at the L-H transition is fitted by an exponential curve, (b) floating potential on inner tip ϕ_{f1}, (c) floating potential on outer tip ϕ_{f2}, (d) approximate radial electric field E_r^*, (f) the envelope of high-frequency (f>10 kHz) turbulence amplitude ϕ_{fenv}, (g) power spectrum of ϕ_{f1}.

Figure 4.8 shows the time evolution of the D_α signal together with the approximate radial electric field E_r^*. E_r^* is derived from the difference of low pass (f < 2 kHz) filtered floating potential fluctuations, i.e. $E_r^*=(\phi_{f1}-\phi_{f2})/dr$. The E_r^* are postulated as the main contributor of poloidal E×B shear flow. The D_α evolution at L-H transitions show an exponential decay rather than the sharp phase change, which indicates that a damping dissipation dominate over the particle recycling process in the SOL. The transition time is $\tau_{L\text{-}H}$~0.5-1ms. The H-L back transitions take a duration as $\tau_{H\text{-}L}$~1.5-2ms, which is about two times longer than the period of L-H transitions. H-L back transitions leads the D_α signal to significantly higher radiation level than in the regular L phase. It is attributed to the crash of edge pedestal at H-L

back transition. It is worth commenting here that the L-H transition can take over immediately even if the radiation level of D_α has not returned to its initial level in L mode (before the first transient L-H transition). The E_r^* near the separatrix significantly weakens after L-H transition. It indicates the E×B flow drops in this edge region during this period.

As is shown in figure 4.8 (e) and (f), the envelope of the turbulent fluctuations is significantly reduced in the H-mode phase. The interplay between the shear flow and turbulence are investigated in figure 4.9. A limit-cycle state is developed in the phase delay between E_r^* and the turbulence intensity ϕ_{fenv} in L-H-L transitions. As can be inferred from the tracing direction of the limit-cycle, it seems that the decay of turbulence lead to a reduction on the amplitude of E_r^* at L-H transition. On the other hand, E_r^* reinforce with increase of the turbulence intensity at H-L transition. Thus, the evolution of the turbulence amplitude leads the E_r^* evolution slightly at L-H-L transitions. Our observation may indicate that turbulence driven zonal flow is responsible for a significant fraction of E×B shear flows during L-H transitions.

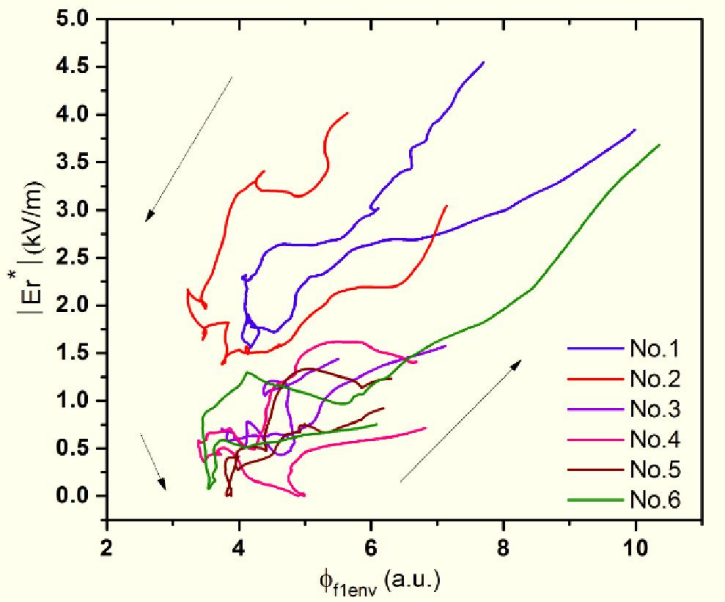

Figure 4.9. Relation between $|E_r^*|$ and fluctuation level of ϕ_{f1}, the No.1…6 is corresponding to the index of sequence of H-phase in the time slice of figure 4.8. Black arrows denote the sequence of L-H-L transitions.

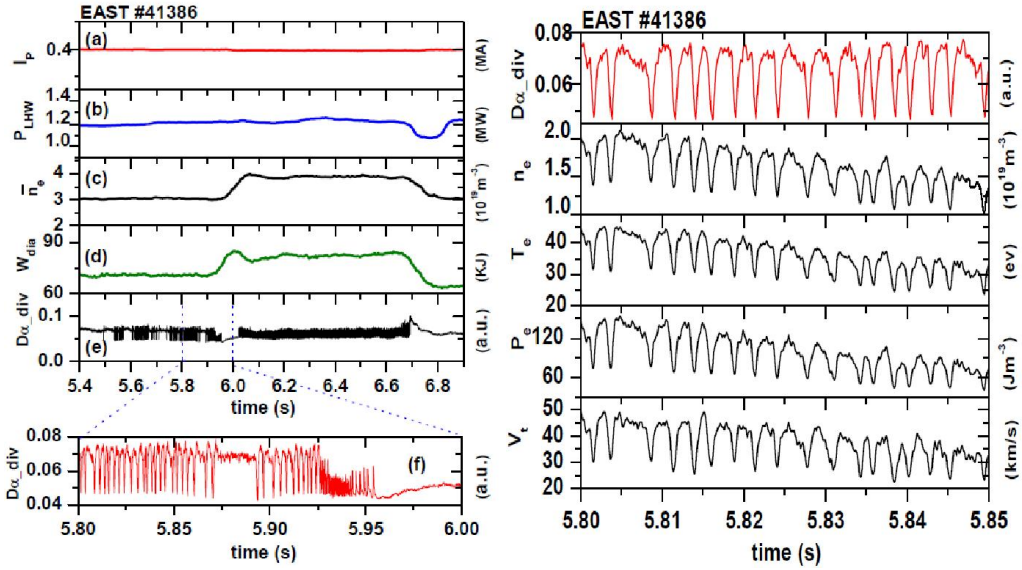

Figure 4.10. left panel: the discharge parameter of #41386 on EAST (a) plasma current, (b) low hybrid wave input power, (c) line-averaged density, (d) plasma stored energy, (e) divertor D_α emission, (f) zoom-in plot of dithering H-mode in (e); right panel: Langmuir probe measurement of SOL plasma parameter during dithering H-mode, plasma density n_e, plasma temperature T_e, plasma pressure P_e, toroidal velocity V_t.

In the vicinity of power threshold of L-H transition, the plasma are observed to undergo a dithering H-mode on EAST. As shown in the left panel of figure 4.10, a Divertor D_α emission show a sequence of transient drop and jump before the plasma eventually enter into a stable H-mode at 5.96s. Indicated by the line-averaged plasma density and stored energy, it seems that dithering H-mode does not enhance the confinement significantly as regular H-mode transition.

To characterize the dithering H-mode, a Langmuir triple probe measurements are made in the near SOL region on EAST. The evolution of plasma parameter are presented in n_e the right panel of figure 4.10. It is found that the plasma density, temperature and pressure in the SOL drop simultaneously with the divertor D_α , which indicate a suppression of edge transport during these transient dithering H-mode. The toroidal rotation of SOL plasma also decrease in the dithering H-mode. It could be attributed to the reduction of population of energetic ions into SOL. From 5.8s to 5.85s, the plasma keeps in a dithering phase where the discharge remains stable and the probe are located in a fixed radial position. However, the SOL parameter gradually decline with the extending of the dithering time during our measurement. Our observation shows that the dithering phase indeed regulate the edge transport and incrementally cooling down the SOL.

Chapter 5

5.1.Edge localized modes

Edge localized modes (ELMs) are observed in tokamak H-mode discharges. They stem from the periodical crash of edge pedestal. The occurring of ELMs produce recurrent losses of particles and energy from the edge region of the confined plasma. On the other hand, ELMs are efficient to eliminate the impurities and helium ash accumulated in the core plasma due to higher confinement in H-mode. ELMs provide a means for particle inventory control at acceptable expense of global confinement. By this fact, the H-mode with ELMs is so far envisaged as the standard operational scenario for ITER [158]. Understanding of ELMs dynamics and transport are urgently desirable for optimizing the performance of fusion plasma.

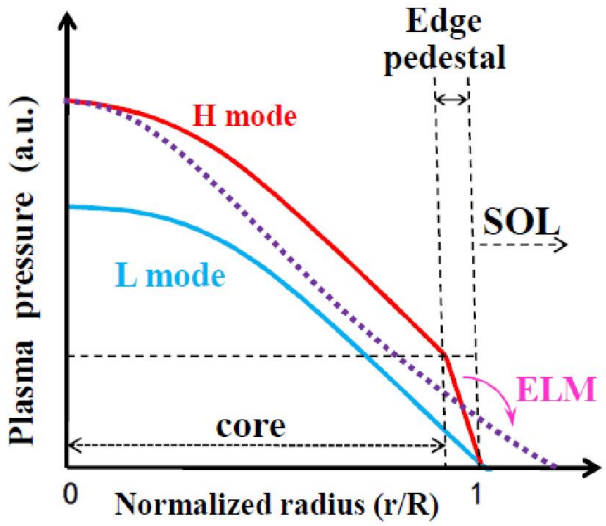

Figure 5.1. Schematic pressure profile in L-mode and H-mode before and after ELM crash

Figure 5.1 illustrates schematic profiles of plasma pressure in L-mode and H-mode plasma. Edge transport barrier with steep pressure gradient forms in the plasma edge region at around normalized radius of $r/a \sim 0.9–1.0$ in H-mode. The deformation of H-mode pedestal/profile take place during ELM crash, which has been detected experimentally by edge Thomson scattering system [159-161] and reflectometer [161, 162]. Each individual ELM pulse carries substantial particle and energy to the SOL region within a few hundred μs or less. It not only impose transient and intolerable power loads on the divertor plates but also increase sputtering of first-wall materials. Extrapolating the energy loss by ELMs, as observed on present day tokamaks to ITER implies that plasma facing wall materials will suffer from fast

erosion or even melting [163]. Control and mitigation of the high heat loads to plasma facing components caused by ELMs is a key issue for the next generation fusion devices such as ITER and even more for DEMO.

The ejection of ELMs are usually manifested by the isolated spikes in Hα(Dα) emission signal. Different types of ELMs have been categorized according to their experimental characteristics [164]. Type-I ELMs and Type-III ELMs are routinely observed in today's tokamak. Figure 5.2 demonstrates a typical observation of type-III ELMs and type-I ELMs on DIII-D with increasing the input power. They usually can be distinguished in detail by the dependence of the ELM repetition frequency ν_{ELM} on the heating power P, the occurrence of magnetic precursors preceding the ELM events, the underlying MHD instability origin.

- Type-I ELMs. the ELM repetition frequency ν_{ELM} increases with heating power P. There is no detectable magnetic precursor oscillation. ELM events emerge at heating power well above the threshold power P_{th} for L-H transition. The pressure gradient of edge pedestal suffer ideal ballooning instability .
- Type-III ELMs. The ELM repetition frequency decreases ν_{ELM} with heating power P close to P_{th}. A coherent magnetic precursor oscillation usually appear before the ELM crash. ELM generation is connected to resistive ballooning instability

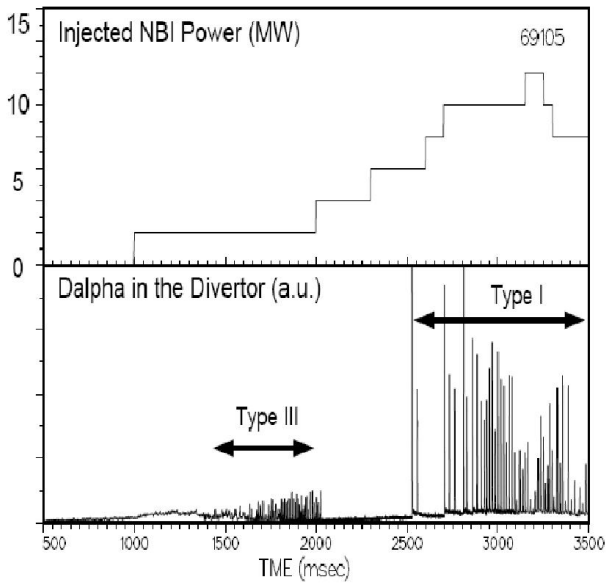

Figure 5.2. Typical sequence of ELMs during a power ramp in DIII-D: type III ELMs are found at threshold power P_{th} for L-H transition, type I ELMs appear at higher input power [164].

Besides the type-I ELMs and type-III ELMs, some small ELM regimes are

recognized in H-mode, such as type-II ELMs on DIII-D [165], grassy ELMs [166, 167] on JT-60 and type-V ELMs on NSTX [168]. They are benign at maintaining the edge pedestal and of a good capability for the impurities exhaust. They are deemed beneficial for the stationary H-mode operation. However, the operational space of these small ELMs are not clear at present, and it is beyond the scope of this thesis.

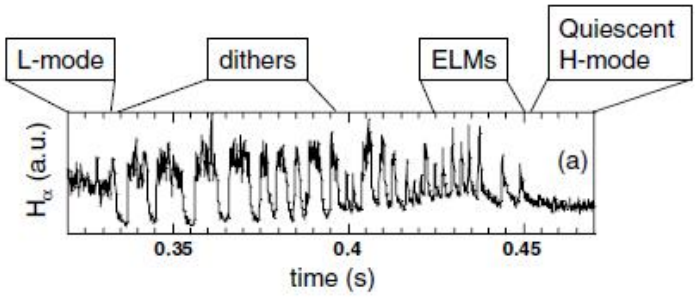

Figure 5.3. Dithering cycle of a slow L–H transition shown by Hα radiation on W7-AS[138].

At L-H transitions just above threshold power P_{th}, the plasma will undergo a dithering phase where plasma jump between the L-mode and H-mode before it produces type-III ELMs. Figure 5.3 shows a typical case of dithering H-mode measured in W7-AS, whereas the transition firstly experience some dithers, then gradually transmute to ELMs. Dithering cycles is often alternatively termed dithering ELMs, since it is difficult to recognize which event is the last dithering cycle, or which one is the first type-III ELM event. Distinct from ELMs as a MHD phenomenon, the dithering cycles are identified as intermediate phase (I-phase) between the L and H modes due to the hysteresis of the H-mode power. Dithering H-mode have been achieved by carefully adjusting the input power on DIII-D [169]. This provides a standard technical approach for the investigation of the L-H transitions. Dithering cycles are interpreted as a sequence of short L-H-L transitions by relating the phase of D_α rise with L-mode and the phase of D_α drop with H-mode. In particular, several recent works have shown that the dithering cycles demonstrates a modulated interplay between turbulence and shear flows [146, 169-171]. The proposed electrostatic scenario for dithering cycles is distinct from a MHD characteristic pertaining to ELMs. The understanding of the dithering phenomenon may provide key insights for the mechanism of the L-H transition itself.

ELMs are considered to originate from a combination of current and pressure gradient driven MHD modes [172], where the initial MHD instability develops flute-like ripples (e.g. n ~5–20 [173], n denotes the toroidal quasi-mode number) in the pedestal thermodynamic quantities, which later grow in magnitude and evolve into distinct plasma filaments. The filaments are expelled from the plasma edge into the

SOL. They carry part of the energy released during an ELM event and propagate through the SOL. The ELM filaments showing as fingerlike perturbations localized in the edge pedestal has been visualized in an electron cyclotron emission imaging (ECEI) on KSTAR [174]. Moreover, the characteristics of ELM filaments have been extensively studied in the SOL on a number of tokamaks using different diagnostic techniques. With the advent of fast visible imaging system, ELMs induced filaments were observed to extend along the local magnetic field line on MAST [159, 160]. Gas puff imaging (GPI) diagnostic on NSTX were used to trace the radial and poloidal velocity of ELM filaments [175]. Beam emission spectroscopy (BES) measurements on DIII-D clearly show the ejection of plasma structures and their 2D movement during ELM events [176]. The structures of individual filaments have been resolved in the divertor power deposition using infrared thermography [177], and the dynamical information of ELM filaments was captured with H_α/D_α radiation array on ASDEX Upgrade [178]. Langmuir probes, as a localized diagnostic with high spatial and temporal resolution, provide a unique access to the local measurements of ELMs. The investigations on characteristics of ELM filaments with Langmuir probes have been widely implemented in JET [178-180], ASDEX Upgrade [52, 181, 182], MAST [159, 181], DIII-D[162, 176], JT-60[161], and TCV[183]. Figure 5.4 shows the substructure of type-I ELM detected by the Langmuir probe on JET. ELM filaments are witnessed as isolated coherent spikes in the ion saturation current signal J_{sat}.

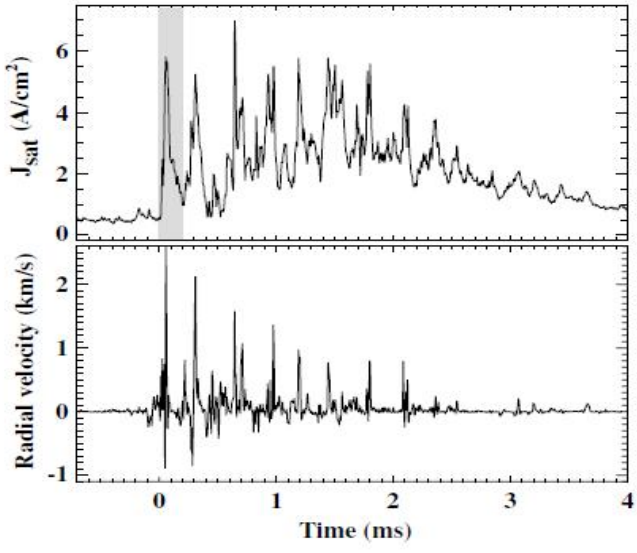

Figure 5.4. Time evolution of ion saturation current J_{sat} and radial E×B electric drift velocity v_r during a small Type-I ELM [179].

It is generally clear that the ELM filaments carry significant particle and energy out from the pedestal during ELM cycles. However, the ability of current transport by ELM filaments is still ambiguous. The magnetic signature of current carrying

filaments in ELMs has been measured in JET using arrays of fast magnetic pickup coils and forward modelling [184, 185]. A spontaneous long-lived rotating current filament or ribbon is observed before the first ELM event inside the JET plasma. It is located at the pedestal top, and regulates transport across the plasma pedestal, significantly delaying the appearance of ELMs [186]. In H-mode with type-I ELMs on ASDEX Upgrade, it is observed that the magnetic-field-aligned ELM filaments carry considerable current during the propagation through the SOL [187]. As shown in the figure 5.5, the ELM filaments give raise to a closed path in the radial and poloidal component of the magnetic field during their passage around the magnetic coils, which indicate a signature of monopolar current transport in the SOL. This experimental observations support the theory reported in [188, 189], which interprets the electromagnetic features of filamentary structures in the boundary plasma. Additionally, bursts in the Scrape-Off Layer Current (SOLC) have been observed concurrently with ELMs [190]. It was proposed that the SOLC plays an important role in triggering the ELMs through magnetic field produced by SOLC which can affect the stability of MHD modes at the boundary and specifically close to the X-point [191-193]. Therefore, the current transport related to the ELM seems to play a key role in regulating the pedestal dynamics.

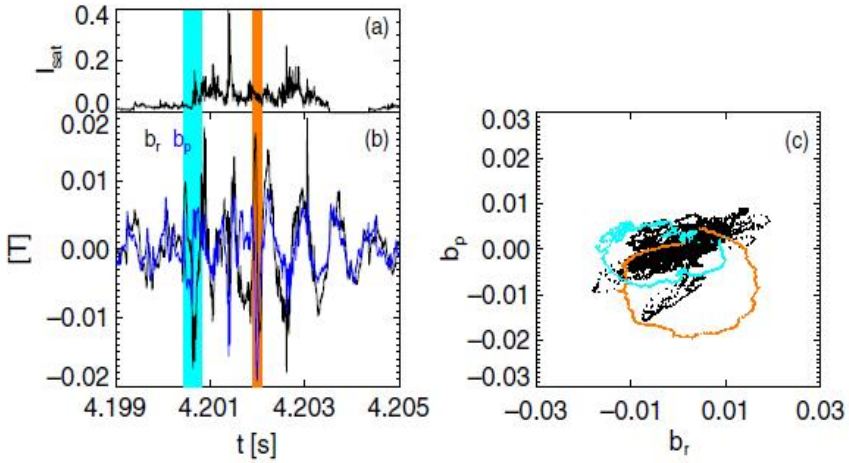

Figure 5.5. (*a*) Ion saturation current, (*b*) radial and poloidal component of the magnetic field, (*c*) hodogram of the perpendicular magnetic field. The two highlighted closed loops correspond to the highlighted time windows in panels (*a*) and (*b*), which indicate passage of current filaments during type-I ELM [194].

To data, the knowledge of ELMs is still limit due to the limitation of diagnostics. The main objectives of this chapter are to study the different types of ELMs, contributing to a better understanding of the transport of ELMs and associated filaments. The electromagnetic characteristics will be recorded during ELMs as well as dithering cycles using Langmuir- magnetic probe in this chapter.

5.2. Langmuir- magnetic probe and discharges

In order to analysis the ELM structure experimentally, a combined Langmuir-magnetic (L-M) probe head was mounted on the reciprocating manipulator on EAST for measuring the dynamics of ELM filaments. Since ELMs are highly non-linear electromagnetic events originating mainly from the transport barrier region (just inside the LCFS), magnetic pick-up coil arrays are prime candidates for ELM structure analysis. Since the local magnetic perturbations fall off fast, probes far away from perturbations are not suited to pick up localized magnetic structures. In our measurement, the probe can be moved radially by a mechanical drive from a position behind the limiters towards slightly across the separatrix. Thus, it possesses capabilities for the near field diagnosis when the ELMs pass by the probe head which can be located transiently (several tens of ms) slightly inside the separatrix close to the threshold power of L-H transitions in EAST. However, even with a near field measurement, the spatial location of responsible magnetic perturbations remains uncertain from such a magnetic diagnostic. To overcome this defect, the probe head is equipped with multi-pin Langmuir probes, which can determine the radial position of ELM structures. L-M probes have been widely implemented to investigate the ELM induced filamentary structures and their dynamics in the SOL and limiter shadow [182, 195, 196].

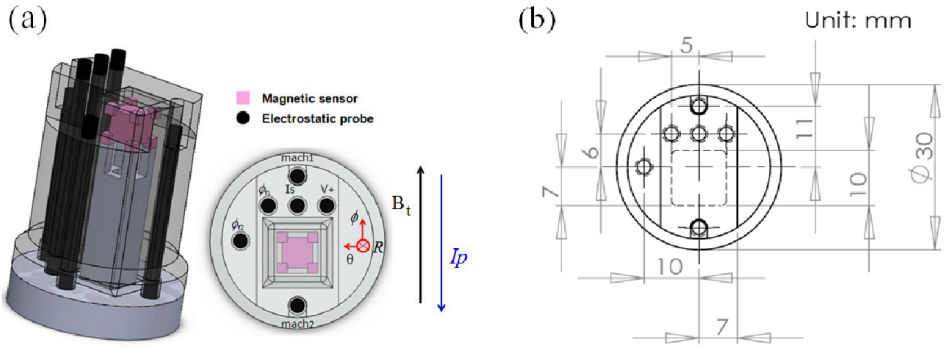

Figure 5.6. (a) Schematic drawing of the probe head constituted by electrostatic pins (black) and magnetic sensor (pink). The top view of probe head shows the location of pins and the magnetic sensor. ϕ aligns along with the toroidal direction, and θ points in poloidal direction. R denotes the radial direction. (b) Detailed layout drawing for the position of Langmuir tips and magnetic coils in the probe head.

Figure 5.6 shows the schematic of the probe head. On the front of a cylindrical boron nitride matrix of about 30mm diameter and 41 mm length, three graphite pins of 2.2 mm diameter and 2 mm length constitute a triple probe. These three pins are equidistantly spaced by 5mm in poloidal direction to measure the floating potential ϕ_{fl}, potential of positively biased probe tip V_+, ion saturation current Is respectively, and

provide diagnostic information on electron density n_e, electron temperature T_e and plasma potential V_{pl}. Three graphite pins are located at another stair of the matrix, which is lower than the top surface by 3 mm. Two of them (*mach1* and *mach2*) are located on each side of the matrix on the toroidal direction as a pair of the Mach probes, and the toroidal separation of them is $L_{mach1\text{-}mach2}$=22mm. The Is pin is separated from the mach1 pin by 5 mm in the toroidal direction. The third pin (ϕ_{f2}) located poloidally 10 mm away from the center of probe head is used to measure the floating potential. The Mach number is estimated from the ratio of the ion saturation current signals, $M_t=0.4\ln(mach_1/mach_2)$, where *mach1* and *mach2* are ion saturation currents to the tips facing upstream and downstream directions respectively [197]. With this probe arrangement, the local toroidal velocity during ELM bursts can be captured. Inside the matrix, 8 mm behind the front side, a triple axis magnetic sensor ($7\times7\times7$ mm^3) is located, measuring the time derivative of the three components of the magnetic field. The boron nitride matrix is enclosed inside a protective graphite tube, but with the top and poloidal surfaces of the matrix being exposed to the plasma to enhance the penetration of magnetic fluctuations. The sensor has a measurement bandwidth of 1 MHz. Table.1 shows the global parameters of discharges investigated using L-M probe head.

Shots	Ip (kA)	B_t(T)	n_e (10^{19}m^{-3})	q_{95}	P_{tot} (MW)			MC	P_{th} (MW)*
					P_{OH}	P_{LHW}	P_{ICRH}		
35353	600	1.8	4.2	3.5	0.3	0.9	×	LSN	1.1
35357	600	1.8	4.2	3.5	0.3	0.9	×	LSN	1.1
39298	500	1.8	2.2	4	0.25	0.7	×	DN	0.82
40547	400	1.9	2.8	5	0.15	0.7	×	DN	0.94
43239	400	1.9	3.6	5	0.15	1.1	1.5	LSN	0.81
43386	400	1.9	4	5	0.15	1.5	×	DN	0.63
43423	350	1.8	3.2	6	0.15	1.4	×	DN	0.76

Table 1. Parameters of the shots presented here: Ip the plasma current, B_t the toroidal magnetic field, n_e the line averaged electron density during the probe measurements, q_{95} safety factor at 95% magnetic flux, P_{in} the injection power composes: P_{OH} the Ohmic heating power, P_{LHW} the lower hybrid wave heating power during the measurements, and P_{ICRH} the injection power from ion cyclotron resonant heating antenna. MC shows the magnetic configuration of the discharges, where LSN and DN indicate the lower single null divertor configuration and the double null divertor configuration, respectively. †The power across the separatrix is caculated as $P_{loss}=P_{OH}+P_{LHW}+P_{ICRH}-P_{rad}-dW_{dia}/dt$, where P_{rad} is the radiation power, dW_{dia}/dt denotes the time variation of stored plasma energy. *The L–H threshold power is estimated as $P_{th}=0.0488 n_{e20}^{0.72} B_t^{0.8} S_A^{0.94}$, where n_{e20} is the line-averaged electron density at the L-H transition in 10^{20} m^{-3}, B_t is the magnetic field in Tesla and S_A is the plasma surface area in m^2 [139]. Detailed investigations on the L–H threshold power on EAST has been carried out and described in [198].

5.3. Survey of precursor activity prior to type-III ELMs and dithering cycles

Typically, type-III ELMs occur in H-mode plasma close to the threshold power P_{th} of the L-H transition. They are characterized with a decreasing repetition frequency f_{ELM} when the input power P_{in} increases ($df_{ELM}/dP_{in} \leq 0$). A coherent magnetic precursor with toroidal quasi-mode number n≈5-15 has been widely observed preceding type-III ELMs [173, 175, 199]. However, the radial location of the precursor has not been unambiguously determined. Similar to type-III ELMs, dithering cycles take place at L-H/H-L transitions when the power across the separatrix P_{loss} is marginal to the threshold power P_{th}. It is important to discriminate dithering cycles and type-III ELMs carefully, since they appear quite similar in the D_α signal and occur subsequently at L-H/H-L transitions. Earlier work pointed out that dithering cycles were not preceded by precursor oscillation which was a typical MHD signature of type-III ELMs [200].

The first H-mode with type-III ELMs was obtained with about 1MW lower hybrid wave (LHW) power on the EAST superconducting tokamak in the 2010 campaign. Type-III ELMs are observed near the H-mode power threshold and produce small energy losses (1-3% of the stored energy) on EAST. The ELM frequency ranges from 0.2 to 0.8 kHz and peaks at 0.4 kHz [198]. The discharge (#35357) investigated here was performed with plasma current I_p=0.6MA, a toroidal field B_t=1.8T on the magnetic axis, and the total input power P_{in} was 1.2 MW with lower single null divertor (LSN) configuration. As shown in figure 5.7, the plasma enters the H-mode at about 3.6s, which is manifested by the sudden increased plasma density and plasma energy. The type-III ELMs appear after a short (~50ms) ELM-free period. The reciprocating probe located 17cm behind the limiter starts to move towards edge plasma at 4.03s and return to the same radial position at the time 4.35s. The front tips reach ~1 cm inside the separatrix at 4.15s and stay there for 50ms, where the uncertainty of LCFS [201] are estimated to be ranged in ±5 mm in this shot. They become emissive in L-mode from 4.18s due to the accumulation of heat load onto the probe in the plasma. The detailed time trace of probe position is shown in figure **5.7** (f), whereas the emissive episode is indicated by the dotted trace.

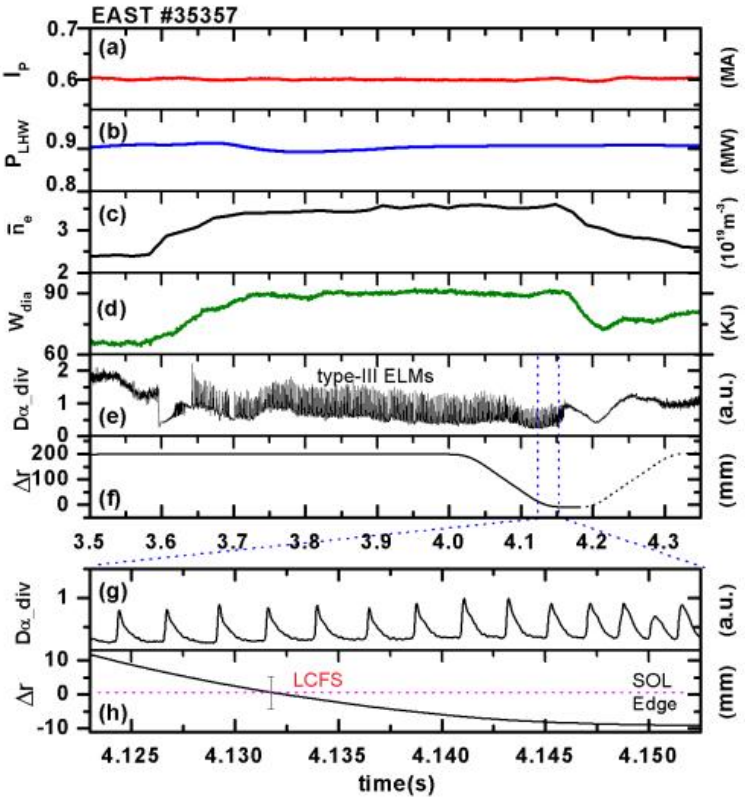

Figure 5.7. Discharge information for the #35357 (type-III ELMy H-mode) (a) plasma current, (b) LHW injection power, (c) line-averaged density, (d) plasma stored energy W_{dia}, (e) divertor D_α emission, (f) radial position of probe tip Is with respect to LCFS, The zoom-in plots show the signals of (g) divertor D_α emission and (h) radial position of probe tip Is with respect to LCFS.

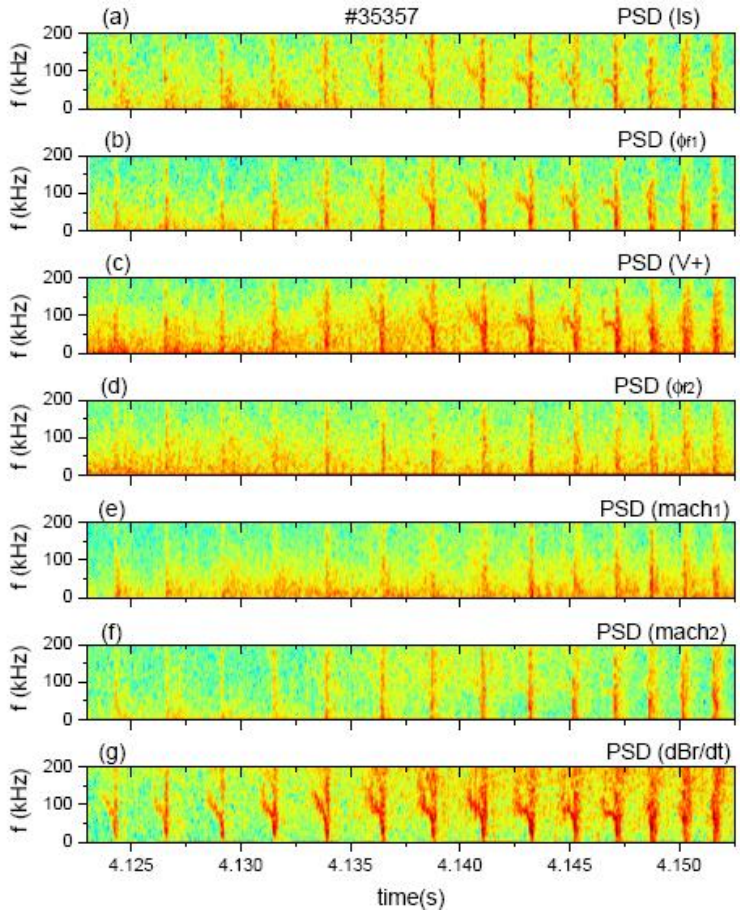

Figure 5.8. Power spectral density (PSD) from (a) ion saturation current Is, (b) floating potential ϕ_{f1}, (c) floating potential of double probe V_+, (d) floating potential ϕ_{f2}, (e) ion saturation current $mach_1$, (f) ion saturation current $mach_2$, (g) time derivative of the radial magnetic field dBr/dt.

Power spectral density (PSD) analysis based on Fourier decomposition has been applied to the raw signals acquired during the time slice as in figure 5.7 (h). As shown in figure 5.8 (g), a precursor before each ELM event is clearly visible in the magnetic fluctuations until after the time 4.148s. The frequency of the precursor decreases from 130 kHz to 30 kHz within approximately 0.4 ms before the ELM breaks out. The Langmuir tips only pick up the precursor inside the last closed flux surface (LCFS) (see PSD(Is), PSD(ϕ_{f1}), PSD(V_+) 4.132s <t<4.148s), but do not detect the precursor in the SOL. The pair of Mach tips ($mach_1$, $mach_2$) and floating potential signal ϕ_{f2} do not capture clear precursor signals in this same time slice, presumably as they are 3 mm further out from the top surface of the probe head. Langmuir probe measurements works based on the interaction between the local plasma and probe tips, we thus conclude that the precursors are initially generated inside the separatrix. However, the magnetic coils can still detect the precursor clearly even though they are located further outside than all the Langmuir tips. This observation strongly indicates

that the precursors occurring inside the separatrix are essentially a current oscillation, which raises the distant magnetic fluctuations. Furthermore, the precursor oscillation is not associated with increase of the particle transport into the SOL, which is evident from the absence of precursor in the ion saturation current Is before 4.133s. After 4.148s, the precursor signals disappear from Langmuir tips even if Langmuir tips located slightly deeper in the edge plasma region. Simultaneously, the magnetic coils do no longer detect the precursor mode. This suggests that the precursor mode actually disappears in this period, implying an underlying new phase different from type-III ELMs taking over after the time 4.148s.

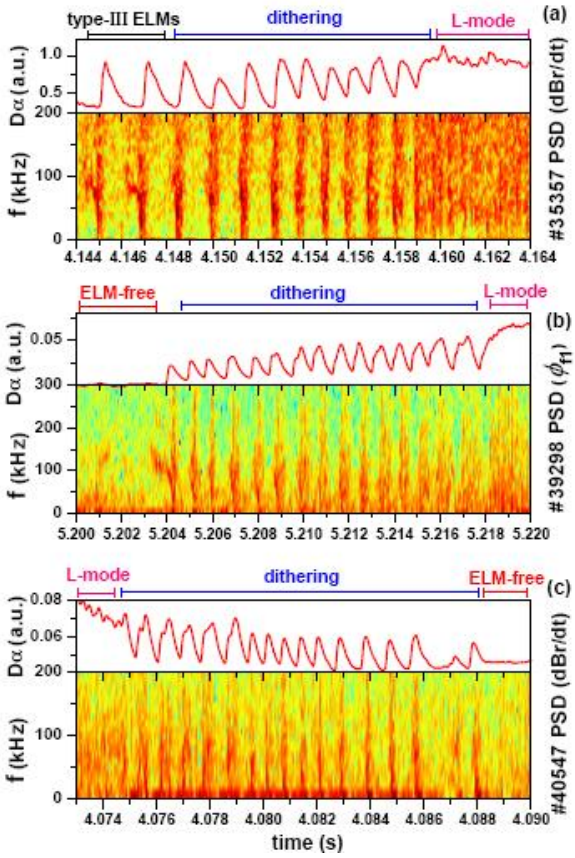

Figure 5.9. Divertor D_α emission together with power spectrum of the signals in (a) magnetic fluctuation dBr/dt in #35357 with H-L transition (type-III ELMs - dithering - L-mode), (b) floating potential ϕ_{fl} in #39298 with H-L transition (ELM-free H-mode - dithering - L-mode), (c) magnetic fluctuation dBr/dt in #40547 with L-H transition (L-mode - dithering - ELM-free H-mode).

Figure 5.9 (a) shows the spectrum analysis of the continued time series of magnetic fluctuations in figure 5.8 (g). The leading probe tips stay at the constant radial position (△r~-10mm) inside the LCFS from 4.15s to 4.2s during the probe stroke in #35357. As is indicted by the D_α signal, an H-L back transition takes place at

4.159s. Thus, it is considered that the H-L dithering cycles are suspected to be responsible for the absence of the precursor mode. As shown in figure 5.9 (b), the absence of precursor modes before the dithering cycles at H-L back transition is further confirmed by probing inside the separatrix (Δr~-10 mm), in which the precursor only appears prior to the first burst event at the transition from ELM-free H-mode to L-mode. The dithering at the L-H transition has been investigated also with magnetic probes near the separatrix Δr~5 mm (see figure 5.9 (c)). The precursor oscillations disappear in the dithering phase at L-H transition as well. Thus, it seems that the precursor oscillation is a signature to distinguish type-III ELMs and dithering cycles. The conclusion from [200] that the type-III ELMs could be discriminated from dithering cycles by the occurrence of magnetic precursor oscillations is further confirmed by the observations in our measurements.

5.4. Multiple filaments composed in type-III ELMs and dithering cycles

5.4.1 Electromagnetic characteristics of multiple filaments

As depicted in section 5.1, plasma filaments have been observed during ELMs in a wide range of tokamaks using a variety of diagnostics. Particularly, ELM filaments have been studied extensively using Langmuir probes. In the probe measurements, the filaments manifest themselves as burst structures in the ion saturation current Is. Besides the identification of filaments, the movement of ELM filaments can be inferred from the signals of Langmuir multi-pins array. On MAST, the reciprocating probe measurements indicate filaments of typical toroidal quasi-mode number n~10 and with toroidal width ~15 cm every 75 cm around the plasma periphery at the mid-plane. The radial velocities of the filaments were deduced from the time delay between the raise of Is at the mid-plane reciprocating probe and the start of the rise in mid-plane D_α emissions. Filaments were observed to speed up with radial velocity 0 in the plasma edge to 1.5km/s at 20 cm outwards [181]. On the mid-plane of ASDEX Upgrade, the toroidal extent of ELM filaments was measured to be 50-80 cm with Langmuir pins. The poloidal width of filaments is about 8-13 cm, separated poloidally by 16 cm[202]. In JET, the characteristics of type-I and type-III ELM filaments were investigated using a reciprocating probe in the SOL. Filaments in type-I ELMs were found to be significantly larger and faster than those observed in type-III ELMs near the limiter radial position. The radial velocity of filaments during type-I ELMs was up to 6 km/s, but it was only on the order of 0.5km/s in type-III ELMs. The radial extension of filaments in type-I ELMs was about 4.8 cm, and the radial extension of filaments in type-III ELMs is around 1.25 cm [179].

Although there is no strict definition of filaments structure in probe measurements, it is generally accepted the large scale spiking structures (1.5 times

larger than the background ELM value [179]) in the ion saturation current Is are due to the interaction between individual filaments and the probe tips. As shown in figure 5.10 (a), the filaments structure during a type-III ELM event can be identified by three distinct peaks in the ion saturation current signal. They last δt~10-20 μs in Is signal, and the interval waiting time between such three Is spikes is Δt~5-10 μs. Since measurements are performed at a single toroidal and poloidal location, the temporally separated structures inside the ELM suggest individual filaments sweeping past the probe. Interestingly, the amplitudes of three detected Is spikes decrease gradually. After these three successive spikes, some trailing structures of small amplitude can still be recognized until 4.1471s. Statistically, the first one is always stronger than the subsequent filaments in our measurements. It is not reasonable to interpret these well declined Is spikes as recurrences of a single filament rotating after a toroidal circumference L along the same field line, since the toroidal velocity (v_t~L/Δt) required in that case is estimated to be in the order of 1000km/s, which significantly deviates from the toroidal velocity (30-90km/s) measured by Mach probe in figure 5.10 (c). The observations may suggest these three prominent Is spikes and small coherent structures are created by multiple passing filaments with degressive plasma density. With this assumption, the toroidal extent of filaments is about 60-120 cm and quosi-quasi-mode number is estimated to be n~10-15. In addition, a prominent time delay between the Is peak and ϕ_{f1} peak is found to be Dt~0-20 μs, yet spiking of ϕ_{f1} is always in phase with spiking of ϕ_{f2}. The time delay between Is spikes and $\phi_{f(1,2)}$ might result from the divergence in topology structure of density and potential in filaments.

The characteristics of fluctuation field are directly influenced by the properties of the sources that give rise to that field, especially the state of polarization of fluctuation field provides greater insight into underlying source of radiation [203]. The degree of polarization (DOP) analysis is an approach for characterizing the polarization properties of fluctuating electromagnetic fields [204-207]. It is estimated from the cross-spectral density matrix $J = [< B_i^* B_j >]$, where the subscripts i and j label the radial/poloidal components and angular brackets denote the ensemble average. As shown in figure 5.10 (e), the ELM precursor is of high DOP values above 0.9. The highly polarized magnetic fluctuations indicate the precursors oscillating in a fixed direction. The decreased DOP of magnetic fluctuations during ELM filaments suggests the magnetic field radiated by filaments is more symmetric in the plane (radial, poloidal) perpendicular to the toroidal direction. This implies that the filaments extend most likely in the toroidal direction and carry a current component.

Figure 5.11 (a) shows the measurement of filament structure during a dithering cycle. As can be seen in the Is signal, more than 10 distinct filaments are detected in one dithering cycle. The transition time of the filaments measured by Is pin is on the same order of magnitude as in type-III ELM (δt~10-20 μs). In the time slice pointed by green arrow in figure 5.11 (a), a crash takes place in Is signal, signifying the

density center of filaments missing the Is pin. At the meantime, the $\phi_{f(1,2)}$ dramatically increase. This observation suggests that the electric potential and the density of filaments are spatially displaced. Most recently, the dithering phase is observed to be accompany with remarkable magnetic fluctuations in EAST [208] and HL-2A [209], but the radiation source of the magnetic fluctuations are not clear in these works. It is the first time here to clarify that the current filaments are responsible for the generation of magnetic fluctuations during dithering phase.

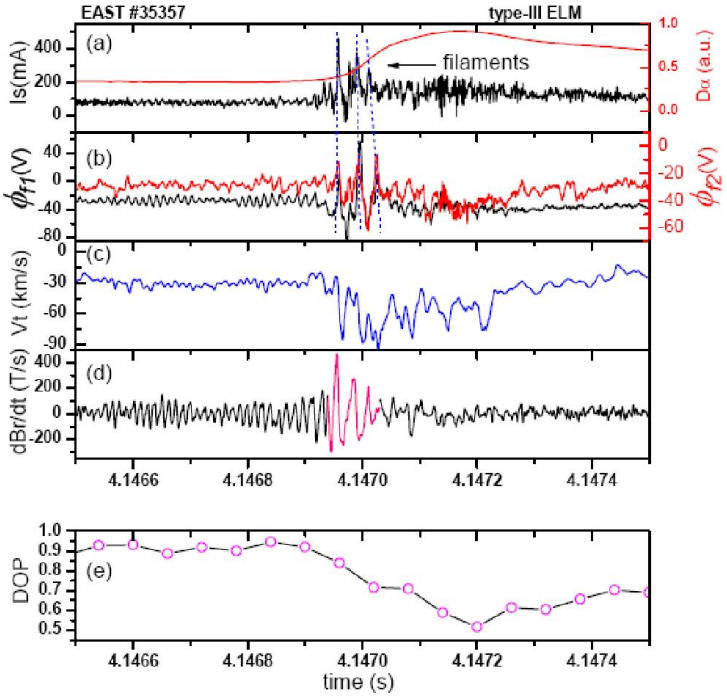

Figure 5.10. (a) Divertor D_α emission together with ion saturation current Is during one type-III ELM event, (b) floating potential ϕ_{f1} and floating potential ϕ_{f2} during one type-III ELM event, (c) toroidal rotation speed V_t during one type-III ELM event, (d) time derivative of the radial magnetic field dBr/dt during one type-III ELM event, the pink signal highlights the magnetic fluctuations induced by the filaments during one type-III ELM event, (e) the degree of polarization of magnetic fluctuations.

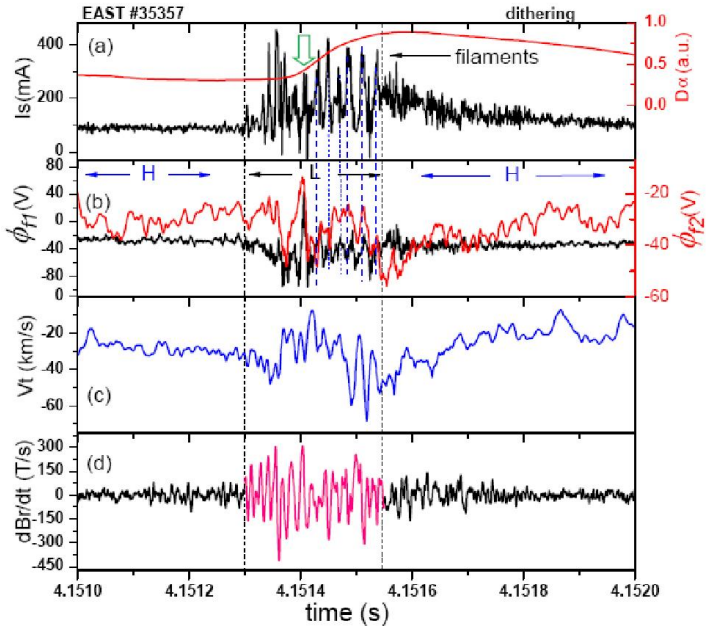

Figure 5.11. (a) Divertor D_α emission together with ion saturation current Is during one dithering cycle, (b) floating potential ϕ_{f1} and floating potential ϕ_{f2} during one dithering cycle, (c) toroidal rotation speed V_t during one dithering cycle, (d) time derivative of the radial magnetic field dBr/dt during one dithering cycle, the pink signal highlights the magnetic fluctuations induced by the filaments during one dithering cycle.

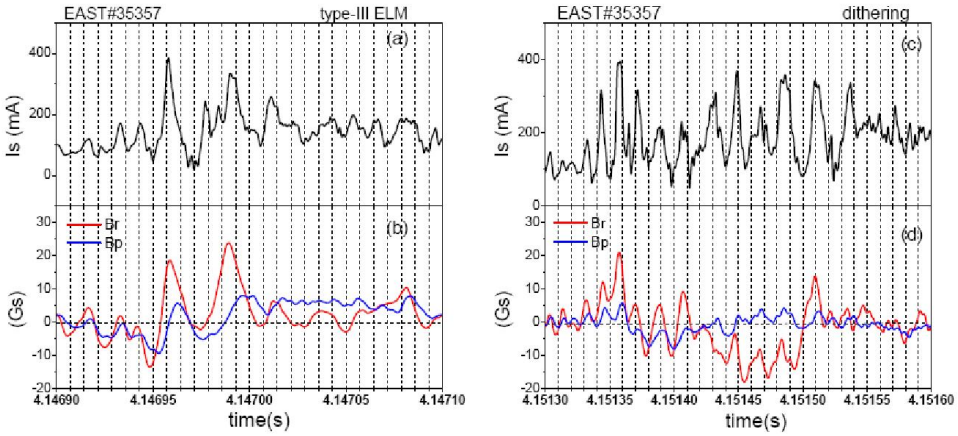

Figure 5.12. (a) filaments in type-III ELM manifested by the spiking structure in ion saturation current Is, (b) the radial component Br and poloidal component Bp of magnetic perturbation during the propagation of type-III ELM filaments, (c) filaments in dithering cycle manifested by the spiking structure in ion saturation current Is, (d) the radial component Br and poloidal component Bp of magnetic perturbation during the propagation of filaments in dithering cycle.

Although it has been realized that the current may exist in the ELM filaments, direct experimental evidence is still very rare due to the ambiguity of the probable current topology in filaments. Even though the basic monopolar and bipolar current models for ELM filaments carrying current has been proposed [188, 210], enormous challenges are still faced when examining the current distribution in filaments with the induced magnetic perturbations experimentally. The validation of current models is a complicated process and can be influenced by many factors such as the direction and velocity of filaments propagation, the distance between magnetic coils and filaments, the action of the other MHD modes, mutual interference among current filaments. The first direct evident for monopolar current carrying filaments during ELMs is reported by Vianello and Naulin et al in ASDEX Upgrade [187], which offers a fundamental reference for our work.

Figure 5.12 shows the induced magnetic perturbations by filaments (shown in figure 5.10 and figure 5.11). The radial and poloidal magnetic perturbations reach their maximal values during the passage of filaments, suggesting a localized current in filaments. It is argued in Ref.[187] that the hodograph of the detected radial and poloidal magnetic field preferably demonstrate a elliptic trace during a radial/poloidal passage of a magnetic field-line aligned monopolar current, and exhibits a cardioid-like shape during the radial/poloidal transverse of magnetic field-line aligned bipolar current. The hodograph of radial and poloidal perturbations, as an indicator of the current topology in filaments, is investigated for filaments both in type-III ELM (figure 5.13 (a)) and dithering cycle (figure 5.13 (b)). However, we failed to obtain a fine elliptic/cardioid hodograph related to the propagating monopolar/bipolar current filaments. It is difficult to assess the current distribution in each filament shown in figure 5.12, since the detected magnetic perturbation during the propagation of a single filament can be readily interrupted by the emergence of another following filament. The current topology of filaments in type-III ELMs and dithering cycles are still ambiguous in our measurements.

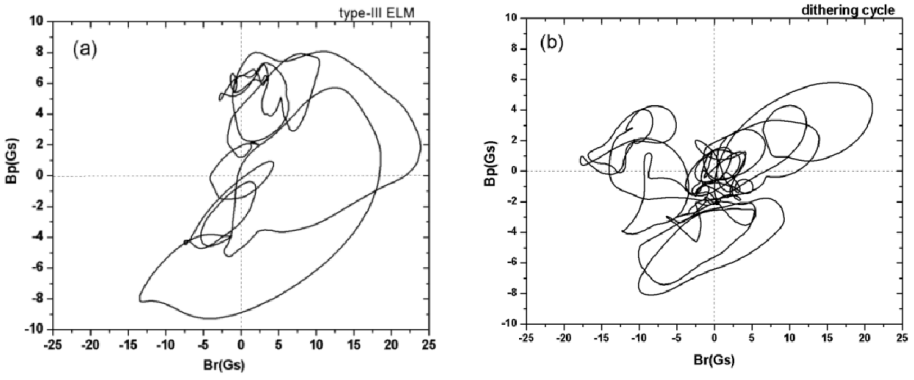

Figure 5.13. The hodograph of radial and poloidal magnetic perturbations during (a) type-III ELM event, and (b) dithering cycle respectively shown in figure 5.12.

5.4.2 The observation of fine structure of type-III ELM in the SOL

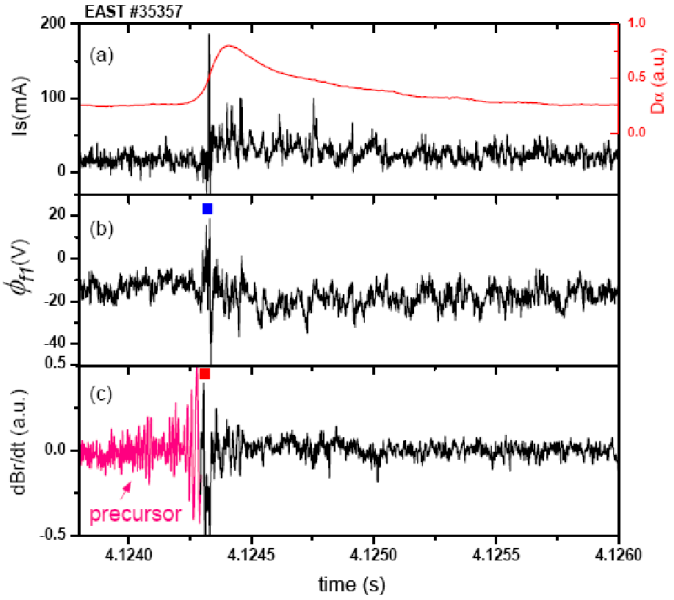

Figure 5.14. Time trace during a single type-III ELM event of (a) ion saturation current Is together with the D_α signal from the divertor target, (b) floating potential ϕ_{fl}, blue square marker refers to the large burst in ϕ_{fl} at the onset of the ELM event,(c) time derivative of the radial magnetic field dBr/dt, red square marker refers to the large burst in dBr/dt at the onset of the ELM event, and the pink line highlights the magnetic precursor preceding the type-III ELM event.

Figure 5.14 demonstrates the fine structures of a type-III ELM event measured at Δr~10 mm. One can note that the precursor in the magnetic fluctuation is clearly visible in figure 5.14 (c), indicated by the enhanced magnetic fluctuation level (pink signal) prior to the ELM onset. In the meantime, the precursor is absent from the Langmuir tip signals (Is and ϕ_{fl}), which has already been depicted in spectrum analysis shown in figure 5.8. Since Langmuir tips are not influenced by the precursor in the SOL, it can provide a clear indication for the transport phase of type-III ELM when it is located in the SOL. As demonstrated in figure 5.14, the type-III ELM manifest itself by an onset of a large spike then followed by a sequence of smaller spikes in the ion saturation current Is, the floating potential ϕ_{fl} and the magnetic fluctuations dBr/dt. These observations agree with our observations inside the separatrix that the primary filament is larger than the subsequent structures.

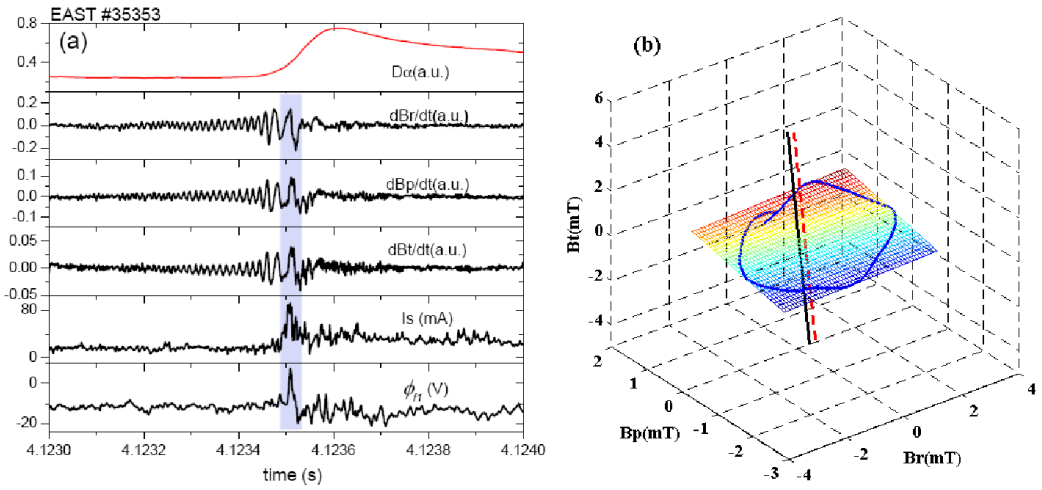

Figure 5.15. (a) The raw signal of time derivative of the three components of magnetic field and electrostatic probe measurements together with the D_α signal from the divertor target (b) Trajectory of a type-III ELM current filament associated magnetic field line excursions in all three spatial directions, the black line shows the direction of the equilibrium magnetic field, and the red dashed line denotes the direction of the minimum variance of magnetic excursion during the passage of density filaments

Figure 5.15 (a) shows a prominent density structure/filaments observed at the onset of a type-III ELM at $\Delta r \sim 17$ mm. As indicated by the vertical bar in figure 5.15 (a), during the passage of the density filaments manifested by the prominent spike in Is, the associated magnetic excursions have dominant odd symmetry for dBr/dt, and a clearly dominant even symmetry for dBp/dt. The localized magnetic perturbations imply a current component persisting in the passing filament. figure 5.15 (b) shows the 3D trajectory of the magnetic field excursion during an ELM. The direction normal to the plane is determined using the minimum variance analysis technique [211]. As can be seen in figure 5.15 (b), the normal direction of this plane (red dashed line) is aligned with the local magnetic field line (black line). It suggests that the filaments at onset of type-III ELM is localized magnetic plasma structure extending along the equilibrium magnetic field.

5.5. Investigations on single ELM filament

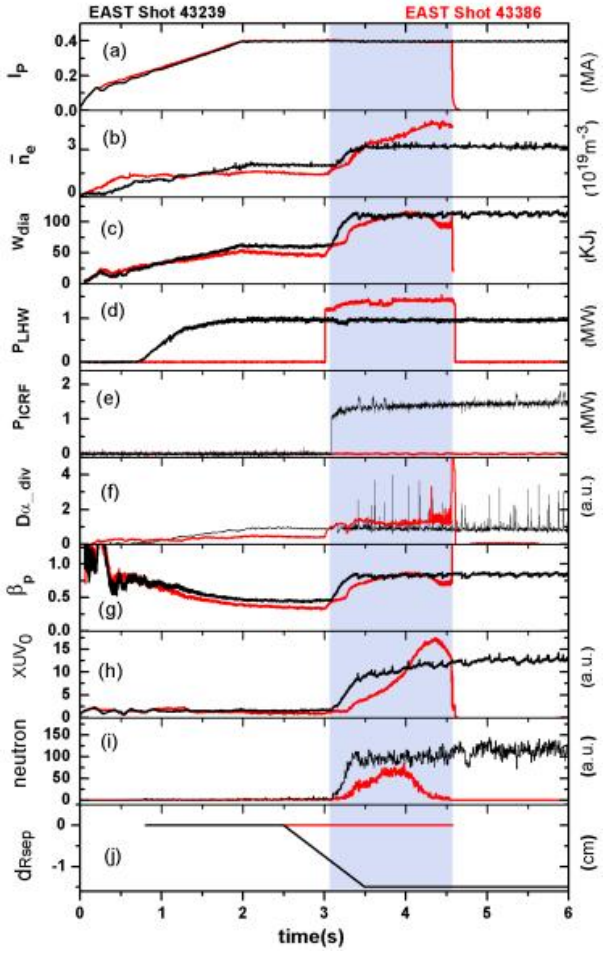

Figure 5.16. Discharge information for the #43239 (type-I ELMy H-mode with LSN configuration) and #43386 (H-mode with DN configuration). (a) plasma current, (b) line-averaged density, (c) plasma stored energy W_{dia}, (d) LHW injection power, (e) ICRH injection power, (f) divertor D_α emission, (g) poloidal beta β_p, (h) XUV radiations in the core plasma, (i) neutron flux，(j) dRsep between two X-points. The lightblue colored region mark the overlapped time window of the H-mode phase between the two shots for comparison.

ELMy H-modes are considered to be the reference scenario for the next step fusion devices, and ITER is envisaged to operate in the type-I ELMy H-mode regime [158]. However, the resulting high heat flux due to type-I ELMs may impose intolerable power loads on the divertor targets, thus posing a serious threat to ITER. The operation regime of plasma performance as type-I ELMy H-mode and less divertor heat loads is desirable for the future fusion device.

In the latest 2012 experimental campaign of EAST, the source power of LHCD and ICRH were upgraded to 3MWand 4MW, respectively. Type-I ELMy H-mode discharges have been successfully achieved with total input power above 2 MW, with

the power threshold P_{th}~0.7MW for the access to H-mode. Most H-mode with type-I ELMs has been obtained with LSN configuration. A typical type-I ELMy H mode discharge is presented in the figure 5.16 (#43239). The plasma stored energy rises from 60kJ to 120 kJ at the L-H transition. The type-I ELMs give raise to giant bursts in the D_α emission signal, and produce considerable energy losses (5%-10% of the stored energy). The β_p increases from 0.5 to 0.8 during the transition, implying an improved confinement in H-mode. The extreme ultra-violet (XUV) bolometer radiation in the core plasma indicates a pinching of density in the plasma, which can be directly confirmed by the enhancement of the central-line-averaged electron density signal ($\bar{n}_e$). In #43386, lower hybrid wave heating (LHW) up to 1.5 MW combined with an Ohmic heating power about 0.15MW is applied to access the H-mode. The total input power is lower than in #43239 $P_{OH+LHW+ICRH}$~2.75 MW, which therefore produces a lower neutron flux than in #43239. Similar confinement parameter has been achieved as in #43239，indicated by the comparable plasma energy and β_p. The key ingredient in this difference of ELM regimes lies in the d_{Rsep}, which is defined as the distance between the two X points mapped at the low field side (LFS) mid-plane. The d_{Rsep}≈-1.5cm, and 0 cm, signifying LSN and DN divertor topologies, are respectively shown in figure 5.16 (j). The intermittent bursts in the D_α emission on the lower outer divertor plate in #43386 is significantly lower than in #43239 (type-I ELMy H-mode discharge) during ELM events.

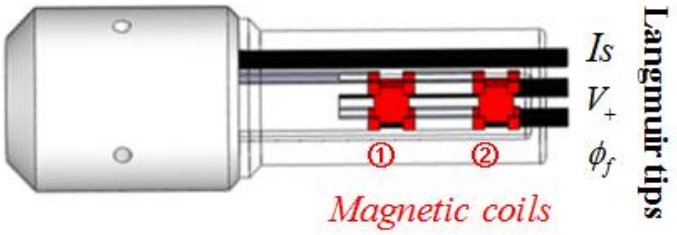

Figure 5.17. Schematic drawing of the filament probe head on EAST. It consists three Langmuir pins (black components) and two magnetic pick-up coils (red components)

The measurements in the discharges shown in figure 5.16 are taken by a pair of superposed triple magnetic coils (8×8×8 mm^3) separated radially by 1cm, see figure 5.17. We use the subscript 1 for the signals on outer coils and subscript 2 for the signals on the inner coils. The probe head stays in the limiter shadow to avoid overheating by the high injected heating power. One disadvantage is that Langmuir pins do not receive significant signals in the limiter shadow, yet the magnetic coils are still able to detect magnetic perturbations without contact with ELM filaments.

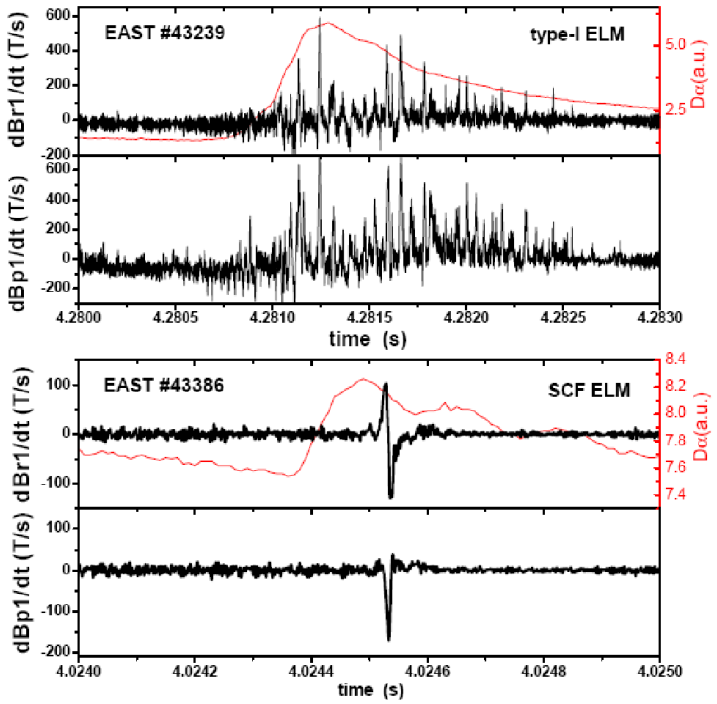

Figure 5.18. Time derivative of the radial dBr_1/dt and poloidal dBp_1/dt magnetic field together with the D_α signal from the divertor target in #43239 and #43386, respectively.

As shown in figure 5.18, the type-I ELM crash produces a number of magnetic perturbations occurring every few tens of μs, which are suspected to originate from movement of current filaments. The comprehensive study on type-I ELM filaments are beyond the scope of this work. ELMs emerging in the parameter regime of #43386 produced small energy losses (2–3% of the stored energy). Distinct from type-III ELM regimes, there are no precursor mode preceding such ELMs. It is worth noting here, that the radial magnetic perturbation exhibits a sinusoidal oscillation pattern, and the poloidal magnetic perturbation appears as solitary peaks. To interpret such appearance, a simple heuristic model has been invoked, which is aiming at investigation of the motion of prescribed magnetic field line aligned current filaments in figures 5.19 (a) and 5.19 (b). The filament carrying a monopolar current, radially induces a magnetic field in the cylindrical configuration, and h indicates the perpendicular distance between the filaments and magnetic coils. Such a propagating current filament raises a magnetic perturbation at the location of magnetic coils during its propagation. We have to stress here that the current filament in our model is assumed to be infinitely long, and we ignore the torodicity of the local magnetic field. Since the pitch angle θ [212] of local magnetic field lines around the magnetic coil is small θ~3.8°, we focus our study here on the plane perpendicular to the toroidal magnetic field without taking the effect of the pitch angle into the account. This model has been previously proposed for filament motion in the SOL [210], but

without experimental input. With the prediction from this simple model, it is found that the measured solitary magnetic perturbations during ELM (#43386) in figure 5.18 are well consistent with the magnetic field induced by the field-aligned radial propagating current filaments. For convenience, we refer to such an ELM regime, with single current filaments, as SCF ELM regime. A similar solitary magnetic perturbation has recently been observed during the so-called 'Edge Snake' MHD instability which consists of a radially and poloidally strongly localized current wire on ASDEX Upgrade [213, 214].

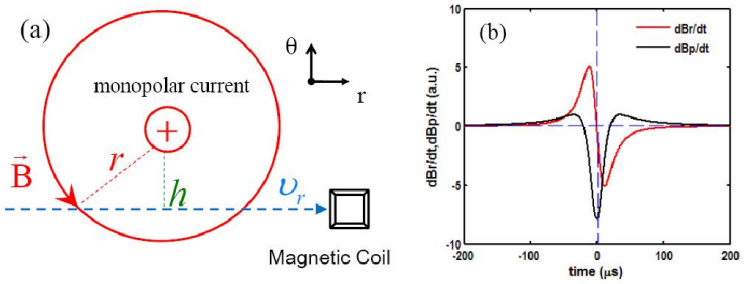

Figure 5.19. (a) Sketch of a propagating monopolar current (b) The time derivative of the radial and poloidal components of magnetic field detected by the magnetic coils during the radial passage of the monopolar current.

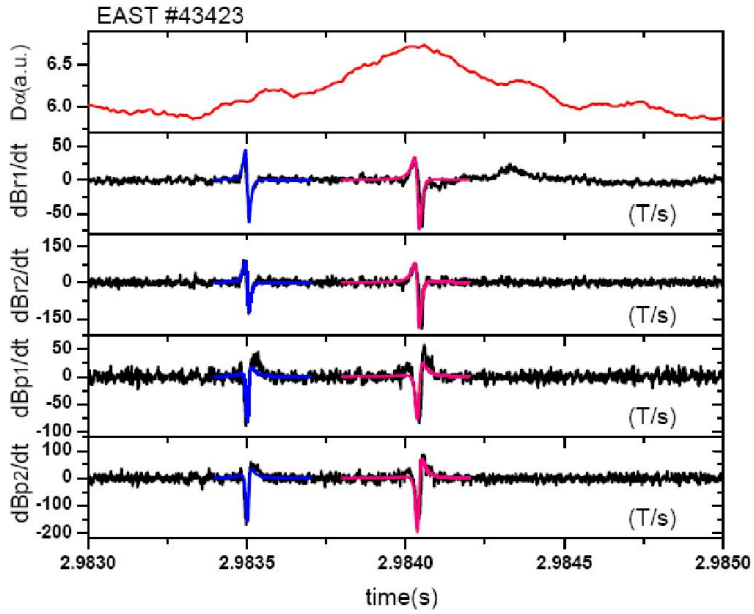

Figure 5.20. Time evolution of D_α signal， time derivative of the radial (dBr_1/dt from outer coil and dBr_2/dt from inner coil) and poloidal (dBp_1/dt from outer coil and dBp_2/dt from inner coil）magnetic field components from a SCF ELM. The blue curve and pink curve is the predictive magnetic perturbation from a monopolar current.

During a SCF ELM event, one can detect 1-3 isolated magnetic perturbations. As shown in figure 5.20, two independent magnetic perturbations occur consecutively during an ELM cycle. It is worth commenting that transport is not localized as in the usual ELM process, which could be inferred from the broad D_α signal. The poloidal magnetic field fluctuation exhibits a detectable 'right shoulder' rather than asymmetric pattern, suggesting a poloidal propagation of filament. Such magnetic perturbation can be well described by the time evolution of induced magnetic fluctuations from a monopolar current filament extended along local magnetic field line (blue line and pink line in figure 5.20). The dynamical trace of the solitary filament is deduced from the approaching match between the measurements and the monopolar current filaments mode as Vp/Vr ~0.75±0.1. Here, the Vr and Vp denote the radial and poloidal propagating velocity respectively. As can be seen in figure 5.20, the signals from the inner and outer coils evolve qualitatively in the same way. It suggests that the current filaments do not sweep across the interval region between the inner and outer coils, otherwise the signals from inner coils and outer coils will be opposite in sign. Furthermore, the signals from the inner coils are stronger than from outer coils. Thus, the current filaments are identified propagating in the region further inside than the inner coils.

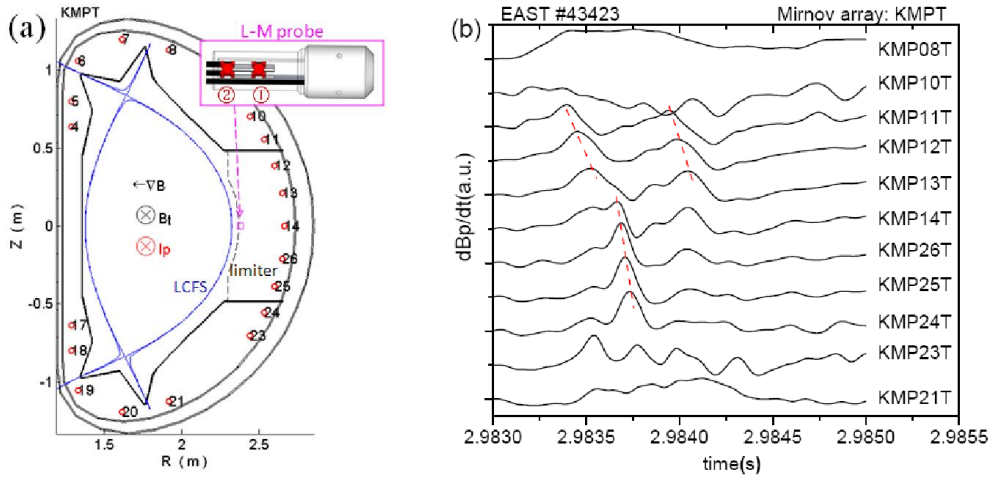

Figure 5.21. (a) The Mirnov coil array KMPT on EAST (b) the magnetic perturbations signal from KMPT

Concerning that the magnetic signature is sensitive to the dynamics of the current structure, the further study of the movement of current structures is assisted by using the Mirnov coil array on EAST. Figure 5.21 (a) shows the Mirnov coil system which consists of 19 channels, located at the same toroidal position. Here, we only show the

signals from Mirnov coils on LFS, as the inboard coils are not able to detect the perturbations associated with ELMs in DN divertor configuration, due to the ballooning character of ELMs, which in DN configuration limits their existence to the LFS from where the ELMs are originating. In figure 5.21 (b), a clear poloidal propagation of the magnetic structures can be observed within the same time slice as in figure 5.20. The poloidal velocity Vp amounts to 2km/s, pointing against the ion B $\times\nabla$B direction, and is propagating in the electron diamagnetic drift direction in this measurement. The conjecture that current structures are propagating in the perpendicular plane of the magnetic field are further explored in figure 5.22, where we show a simulation based on the of a propagating monopolar current filament with Vp/Vr~0.75. With the supposed radial drift velocity of Vr~2.5 km/s, the simulated signals consistent with the experimental measurements can be reproduced if the prescribed current filament sweeps across the magnetic coils with a perpendicular distance h~1.6 cm and carry a monopolar current I_f ~15A. As predicted in the simulation, the magnetic perturbations captured by magnetic coils during the sweeping of the current filament would give an elliptical trajectory in the hodograph of the radial magnetic perturbation Br and poloidal magnetic perturbation Bp. The traverse of the current filament in front of the magnetic coils takes place in radial and poloidal direction, which leads the reversal of the direction of the detected magnetic field during the passing of the current filament. As can be seen in figure 5.22, the hodograph essentially take over in three quadrants, i.e., both the Br and Bp reverse their sign at the propagation of the envisaged current filament. Experimental measurements reach a good agreement with the expectation of the simulation model given that the assumed sweeping distance h and the filament current I_f are reasonable. Thus, it is demonstrated that current filaments confidently persist in the SCF ELM regime. However, it is still unclear where and how the current filaments are created in the SOL.

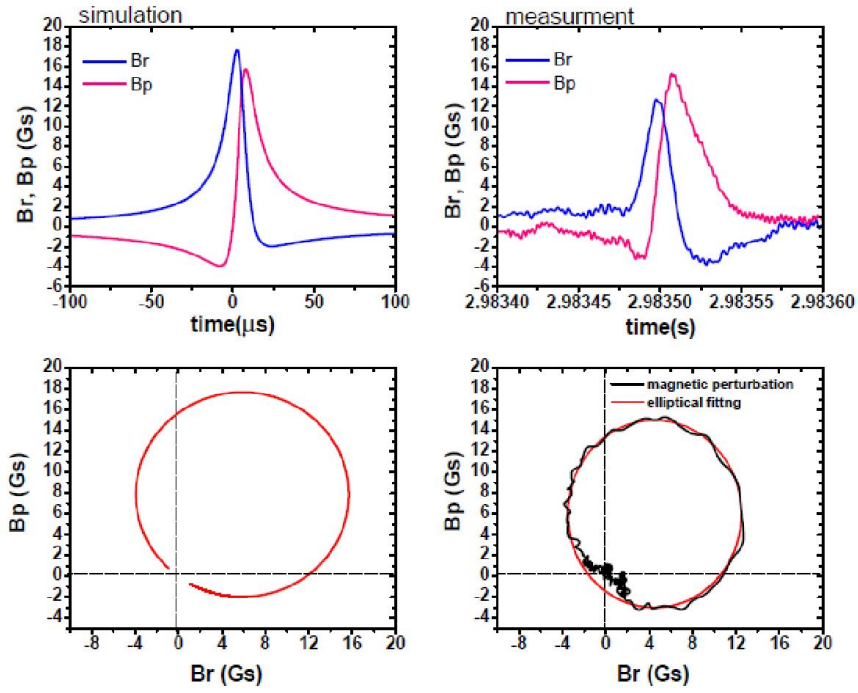

Figure 5.22. Simulation of magnetic perturbation induced by a monopolar current (left panels) and the experimental observation of current filament-like structure by inner magnetic coils (right panels)

5.6. Particle, heat and poloidal momentum transport by ELMs

5.6.1 Particle and heat transport by ELMs

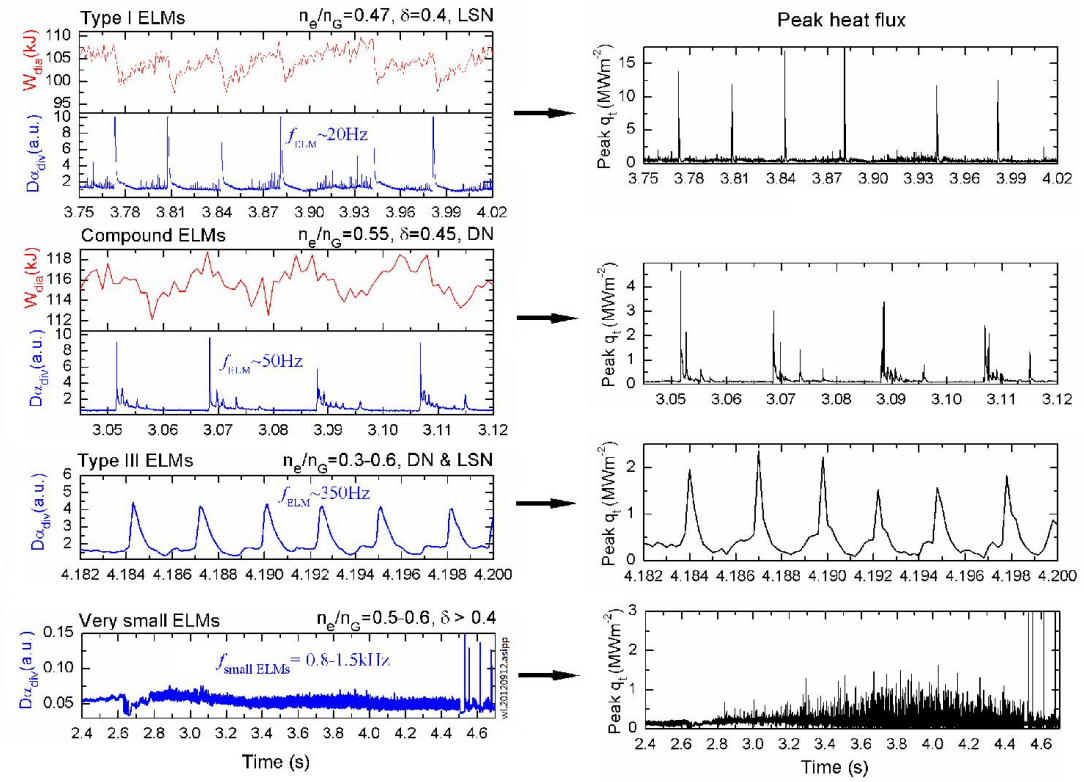

Figure 5.23. Left plot shows the characterization of type-I ELMs, compound ELMs, type-III ELMs, very small ELMs and irregular ELMs and corresponding peak heat flux on divertor targets in right plot.

Various types of ELMs are achieved in EAST H-mode plasmas. They are classified according to their repetitive frequency and caused heat load to the divertor targets. Figure 5.23 shows the characteristics of four typical types of ELMs observed on EAST. i.e. type-I ELMs, compound ELMs, type-III ELMs, small ELMs. The frequencies of the type I, compound, type-III and small ELMs are f_{ELM} ~ 20 Hz, ~50 Hz, ~350 Hz and 0.8–1.5 kHz, respectively. The peak heat flux q_t on divertor targets caused by type-I ELMs is about 10MWm^{-2}. The compound ELMs pose heat flux of 2-5 MWm^{-2} to the divertor target, which is slightly higher than it result from type-III ELMs (q_t<2 MWm^{-2}). Small ELMs are of smaller amplitude, and thus lead to a benign heat load which is below 1 MWm^{-2} on divertor. Different ELMs are practically achieved under different operational regime. The type-I ELMs appeared only in LSN configuration when the total heating power exceeded 1.5 times the L–H threshold power P_{th}, with the line-averaged density n_e/n_G < 0.5 and the triangularity δ ~ 0.4. Here, n_G denotes Greenwald density limit. The compound ELMs are usually

manifested by an initial large burst followed by a sequence of small spikes in D_α signal. They were typically observed at higher densities ($n_e/n_G \sim 0.55$) in DN, with higher triangularity ($\delta \sim 0.45$) and lower heating power than type-I ELMs. The type-III ELMs are obtained in EAST around the L–H threshold power in both DN and LSN, showing no strong dependence on the plasma shape. The small ELMy H-mode regime was also achieved in highly shaped plasma at high density ($n_e/n_G \sim 0.6$), but disappeared for $\delta < 0.4$. The different ELMy H-modes produce a wide range of schemes for particle transport and power distribution on divertor. They can provide alternative approaches for the operations of fusion device like ITER.

In order to obtain detail insight on the ELM transport, double-deck Langmuir-Mach probe array are mounted on the reciprocating manipulator to implement the measurements in the SOL during the ELM events. Two layers are radially separated by dr = 3 mm. Each layer is composed of 4-tip Langmuir probe and Mach probe array. The 4-tip Langmuir probe consist a 220 V biased double probe ($\phi_{+1,2}$, $Is_{1,2}$), and two additional floating potential $\phi_{f1,2}$ or $\phi_{f3,4}$. The detailed arrangement are sketched in figure 5.24. This probe array is able to measure the local electron density n_e, electron temperature T_e, plasma potential ϕ_p and parallel ion flow velocities $V_{//}$ simultaneously. The graphite pin is 2 mm in length and 2 mm in diameter. Poloidal electric field E_θ is deduced from two floating potentials separated by $d_\theta \sim 7mm$ in the poloidal direction assuming that the temperatures and the sheath drops are identical in both the probe tips and that the plasma structures are larger than the separation between the probes, i.e. $E_\theta \sim (\phi_{f1} - \phi_{f2})/d_\theta$.

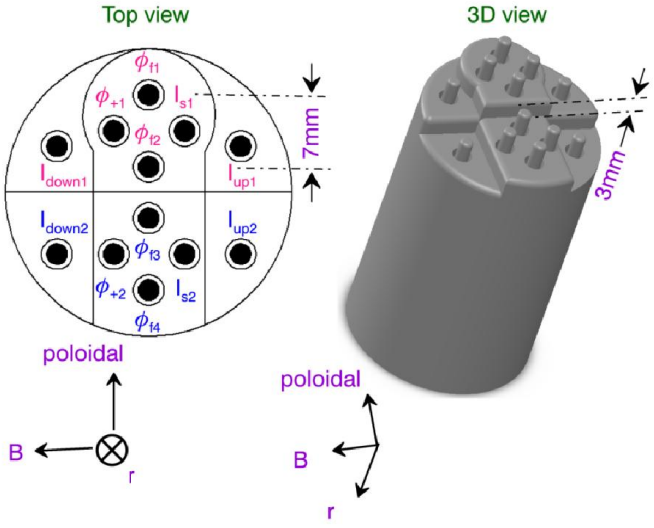

Figure 5.24. Layout of the double-deck Langmuir-Mach probe array.

Assuming the toroidal magnetic field B_t, the arrangement of 4-tip Langmuir probe also allows the simultaneous measurements of the turbulent (electrostatic) particle flux Γ_r, heat flux Q_r, which reads respectively:

$$\Gamma = \frac{1}{B_t} < \tilde{n}_e \tilde{E}_\theta > ;$$

$$Q = \frac{3}{2B_t} < n_e T_e E_\theta >= Q_{conv} + Q_{\mathrm{cond}}$$

$$= \frac{3}{2B_t} n_{e0} < \tilde{T}_e \tilde{E}_\theta > + \frac{3}{2B_t} T_{e0} < \tilde{n}_e \tilde{E}_\theta > \qquad (5.1)$$

Each parameter $(x = n_e, T_e, E_\theta)$ are expressed as a summation of stationary x_0 and fluctuating component $\tilde{x}$, i.e. $x = x_0 + \tilde{x}$. Where the heat flux Q is contributed by two components, i.e. conductive term Q_{cond} and convective term Q_{conv}. Therefore, the 4-tip Langmuir probe array provide unique capabilities in allowing the determination of detailed information of ELM induced particle and heat transport in the SOL plasma. Since the type-III ELMs and type-I ELMs are routinely observed in the experiment, we focus our investigation here on these two common types of ELMs.

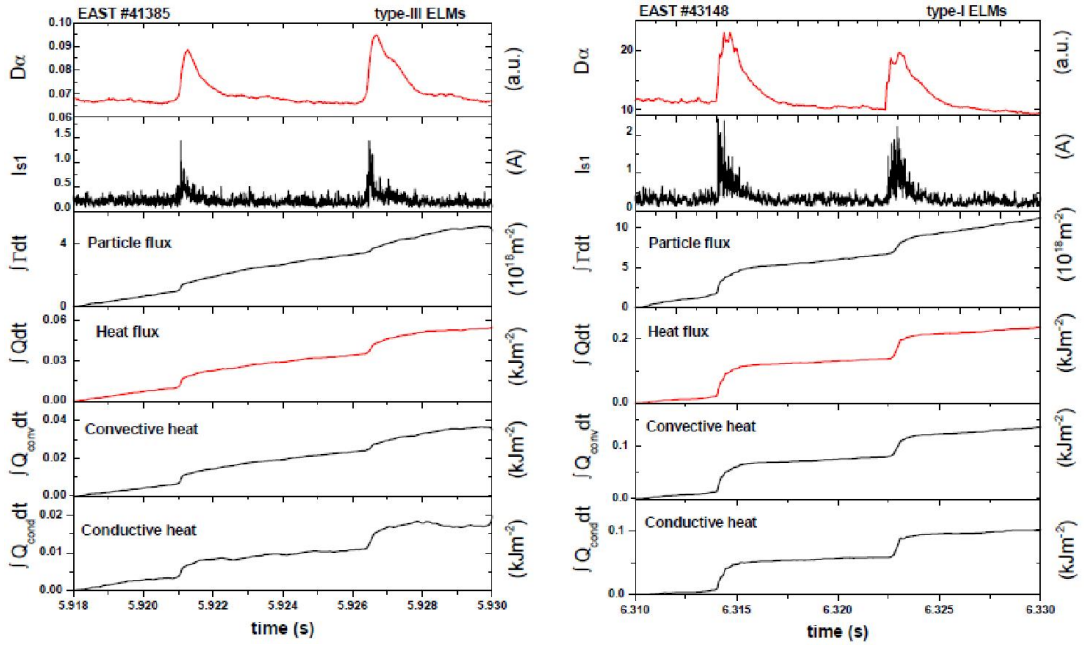

Figure 5.25. The time integrated radial turbulent particle and heat flux during type-III ELMs (left panel) and type-I ELMs (right panel). The measurements were made about 0.5 cm outside the separatrix.

The turbulence induced particle and heat flux during type-I and type-III ELMs are measured by the front 4-tip Langmuir probe. As shown in the figure 5.25, a sequence of two type-III and two type-I ELMs are analyzed. These two types of

ELMs are captured about 0.5cm outwards away from the separatrix. As indicated by the ion saturation current signal I_{s1} the amplitude of type-I ELMs is about twice than it of type-III ELMs. The time integrated radial particle and heat flux is significantly higher during the type-I ELMy H-mode than in type-III ELMy H-mode SOL plasma. At the occurrence of type-I ELMs, the particle and heat flux are suddenly enhanced, which lead to a pronounced lift-up step at the time integrated flux. Each type-I ELM can increase about 2×10^{18} m^{-2} particle flux and 0.1kJm^{-2} at the measuring position, whereas type-III ELM induced particle flux is less than 1×10^{18} m^{-2} and the local heat flux carried by type-III ELM is one order lower than in type-I ELMs. For both type-I and type-III ELMs, the convective and conductive heat transport are almost balanced to each other. This consequence are also manifested during inter-ELM period.

5.6.2 Radial transport of ELM induced poloidal momentum

Compared to ELM induced energy and particle transport, however, there has been considerably less effort addressing momentum transport by ELMs. Since overall confinement is sensitive to rotation and velocity shear, momentum transport by ELMs has naturally attracted a large concern [215-217]. In this section, we focus our attention on the radial transport of ELM induced momentum. The radial flux of turbulence driven poloidal momentum reads:

$$M_{pr} =< nv_r v_\theta >= n_0 < \tilde{v}_r \tilde{v}_\theta > + v_{\theta,0}\Gamma + < \tilde{n}\tilde{v}_r \tilde{v}_\theta > \qquad (5.2)$$

Here, n denotes the plasma density, v_r radial velocity of plasma is, v_θ poloidal velocity. The total poloidal momentum flux is composed of three terms. They are, Reynolds stress term $M_{p,Re} = n_0 < \tilde{v}_r \tilde{v}_\theta >$, convective momentum $M_{p,conv} = v_{\theta,0}\Gamma$ and triple fluctuation term $M_{p,trip} =< \tilde{n}\tilde{v}_r \tilde{v}_\theta >$, respectively.

The necessary parameter for the determination of radial flux of poloidal momentum could be derived from the measurement of double-deck Langmuir-Mach probe array. Assuming the temperature fluctuations is small, the turbulent radial electric field and poloidal electric field are obtained as $E_r \sim (\phi_{pu}-\phi_{pl})/d_r$, $E_\theta \sim (\phi_{f1}-\phi_{f2})/d_\theta$ with $d_r=3mm$, $d_\theta=7mm$. ϕ_{pu} and ϕ_{pl} represent the plasma potential measured in upper stairs and down stairs of the double-deck Langmuir-Mach probe array. The radial and poloidal plasma velocity could be derived accordingly as $v_{r,\theta} = E_{\theta,r}/B_t$. Therefore, we are able to evaluate the contribution from the Reynolds stress term, convective momentum term and triple fluctuation term to the poloidal momentum transport using the double-deck Langmuir-Mach probe array.

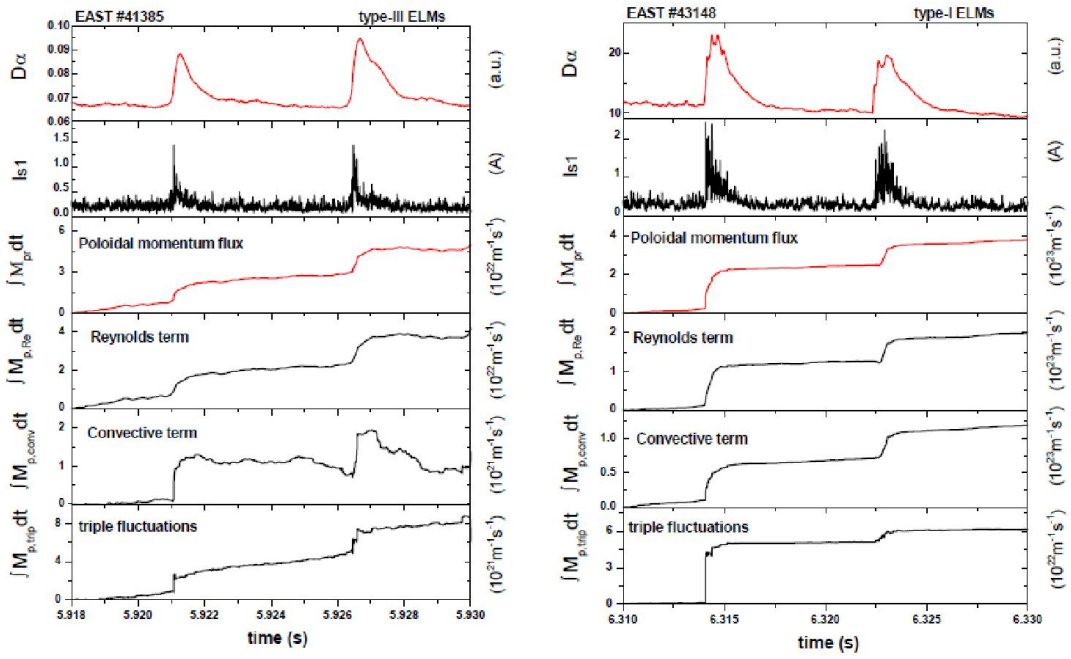

Figure 5.26. The time integrated radial flux of poloidal momentum during type-III ELMs (left panel) and type-I ELMs (right panel). The measurements were made about 0.5 cm outside the separatrix.

The figure 5.26 shows the time trace of integrated radial flux of poloidal momentum and its three main driven terms. Radial flux of turbulence driven poloidal momentum during type-III ELMs is one order lower than it during type-I ELMs. For both type-III and type-I ELM events, by Reynolds stress term is a main contributor for the radial transport of the poloidal momentum, and the triple fluctuation term are one order smaller than the momentum driven by Reynolds stress. The convective momentum during the type-III ELM events is one order smaller than the momentum driven by Reynolds stress, but it become comparable with the Reynolds stress driven poloidal momentum flux during the type-I ELMs. To sum up, the poloidal momentum is mainly driven by Reynolds stress during type-III ELMs, and it is consisted by two decisive portion with same order of amplitude, i.e. the Reynolds stress term as the most important contributor, and the convective momentum as secondary important contributor.

5.6.3 Radial transport of ELM induced toroidal momentum

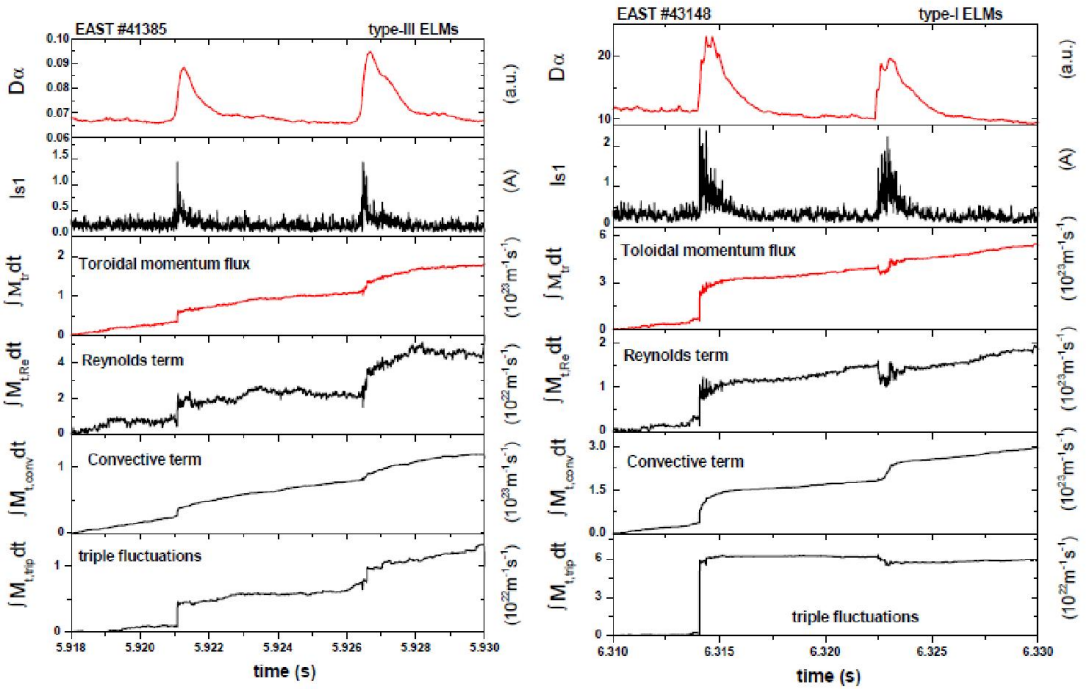

Figure 5.27. The time integrated radial flux of toroidal momentum during type-III ELMs (left panel) and type-I ELMs (right panel). The measurements were made about 0.5 cm outside the separatrix.

The radial flux of turbulence driven toroidal momentum reads:

$$M_{tr} =< nv_r v_t >= n_0 < \tilde{v}_r \tilde{v}_t > + v_{t,0}\Gamma + < \tilde{n}\tilde{v}_r \tilde{v}_t > \qquad (5.3)$$

Here, n denotes the plasma density, v_r radial velocity of plasma is, v_θ poloidal velocity. The total poloidal momentum flux is composed of three terms. They are, Reynolds stress term $M_{t,Re} = n_0 < \tilde{v}_r \tilde{v}_t >$, convective momentum $M_{t,conv} = v_{t,0}\Gamma$ and triple fluctuation term $M_{t,trip} =< \tilde{n}\tilde{v}_r \tilde{v}_t >$, respectively. The toroidal rotation v_t velocity are obtained approximately as $v_t \sim M_{//} C_s$, where the $M_{//}$ signifies the parallel Mach number measured using the mach probe, C_s is the local sound speed.

As shown in the figure 5.27, the radial transport of toroidal momentum is dominated by convective term for both type-I ELMs and type-III ELMs. The Reynolds stress driven toroidal momentum flux is one order lower than convective momentum during type-III ELMs, and it degrade to the secondary drive for the toroidal momentum transport in type-I ELMs. In general, the grade of Reynolds stress driven momentum and convective momentum during ELMs are exactly reversed in the scenario of radial transport of poloidal momentum with respected to the radial transport of toroidal momentum transport.

Chapter 6

Summary and outlook

6.1. Summary

For over three decades, the filamentary plasma structure has attracted large attentions. The radial ballistic transport of filaments redistributes the particle and energy in the SOL, which is strongly connected to the flatness of SOL profile, robust turbulent fluctuations, and the erosion of plasma facing components. It has been widely accepted these coherent structures play a key role in reducing the plasma confinement. In L-mode, such filamentary structures are named blobs, whereas the filaments emerging in ELM events as associated substructures, are termed ELM filaments. This thesis devotes itself to characterize the plasma filaments observed both in L-mode and H-mode plasma using the probe diagnostics. Conclusion remarks will be documented bellow according to main works presented in this thesis.

- **L-mode plasma**

In L-mode plasma, the edge pedestal sets up with a poloidal E×B velocity shear layer. The velocity shear reduces the turbulence intensity and modifies the cross phase angle of density and plasma potential to be zero. Edge shear layer effectively blocks the spreading of turbulence generated from the inward region. The coherent modes GAM are observed with a frequency f_{GAM}~4-7 kHz in the top of edge pedestal. They are characterized as toroidal and poloidal symmetric electrostatic structure. The experimental scaling of f_{GAM} is well consistent with the theoretical prediction, i.e. f_{GAM}~$C_S/2\pi R$, where the C_S and R resents the ion sound speed and major radius of the device. GAM disappears outwards in the radial location with steep pressure gradient.

Blobs are observed to created together with the holes in the edge shear layer in EAST. They are usually witnessed as isolated density structures of amplitude 1.5-3.5 times of background density fluctuations. The blobs propagate radially outwards. They penetrate the pedestal and eject into the SOL. The intensity of background turbulent fluctuations decline outwards. Hence, isolated blobs become more conspicuous in the background turbulence in the far SOL. The PDF of density fluctuations follows a log-normal distribution. Moreover, the skewness (S) and kurtosis (K) of the PDF of density fluctuations shows a parabolic regression ($K=1.97S^2+2.68$), which agrees well with the international multi-machine scaling. The two dimensional turbulence code ESEL on interchange instability is invoked to predict the behavior of SOL turbulence on EAST. The profiles of background plasma predicted from ESEL code reach a good agreement with the Langmuir probe measurement in the SOL plasma in EAST. The statistic feature of SOL turbulence from ESEL simulation and EAST measurements resembles each other. Particularly,

the skewness and kurtosis of the PDF of density fluctuations in ESEL also follows parabolic curve ($K=1.42S^2+2.65$). Our observations suggest that the coherent structure blobs/filaments are generated from the interchange driven turbulence.

The temperature fluctuations is investigated in the L-mode plasma. It was measured that the blobs in limiter plasma are of exceeded temperature in the density center. However, the temperature in the blob center are detected to be lower than surrounding plasma in divertor discharge. Using two point correlation technique, the size of blobs is estimated to be larger than the probe separation in limiter plasma, whereas it is smaller than the probe separations in the divertor plasma. The spatial size of the blobs is believed to affect the temperature evaluation using Langmuir probe tips. The technical error could occur when the blob size is smaller than the probe separation according to the stand Langmuir probe theory. ESEL code predicts that the blobs are of exceed temperature in the density center. On the contrary, the artificial probe array imbedded in ESEL simulation shows that the blobs are of a depletive temperature structure. Therefore, both the EAST measurements and ESEL simulation can qualitatively demonstrate the influence of probe separation on the estimations of blob temperature.

The parallel SOL flow shows a strong dependence on the plasma density in EAST. Analytical study based on Pfirsch-Schliiter flow were carried out to improve the understanding of the ion flows. Considering the fact that ions is natually hotter than electrons in the SOL plasma (i.e. $T_i>T_e$), and the SOL ion temperature decay length tends to be larger than the electron temperature decay length $\lambda_{Ti} >\lambda_{Ti}$, the obtained plasma profiles from Langmuir probe measurements are modified with the assumptions: $T_i\approx2T_e$ and $\lambda_{Ti}\approx1.5\lambda_{Te}$. It was found the Pfirsch-Schlüter flow accounts for a dominant fraction in the parallel SOL flow in EAST.

- **L-H transitions**

Near the power threshold, a modulation of D_α signal at a frequency ~2kHz were frequently observed just before the L-H transition. By probing inside the separatrix at the L-H transition, oscillation of radial electric field E_r are detected to occur perfectly in step with the of D_α modulation happening in the divertor target. The E_r regulation is strongly correlated with Reynolds stress force. Once the shear rate of $E_r\times B$ flows exceeds the turbulence decorrelating rate, then the local turbulence is suppressed. Our observations suggest a signature of Zonal flow preceding the L-H transitions.

Multiple transient L-H-L transitions are investigated using Langmuir probe. During the L-H-L transitions, the evolution of edge turbulence intensity leads the radial electric field inside the separatrix. It suggests that the zonal flow is a dominant component of the E_r at the transient L-H-L transitions. Besides, the probe measurements shows the SOL are gradually cooling throughout a sequence of

transient L-H-L transitions.

- **ELM physics**

In ELMing H-mode plasma, a Langmuir-magnetic probe is used to observe the dynamics of ELMs and associated ELM filaments. Specifically, the current transport ability of ELM filaments is investigated in this thesis.

Both type-III ELMs and dithering cycles occur near the power threshold of L-H/H-L transition. They take place sequentially and look similar from the D_α signal. Type-III ELMs are found to be preceded by a MHD precursor with a declining frequency 130kHz-30kHz, but the precursors are absent at dithering cycles. Therefore, the precursor is a favorable indicator to distinguish the type-III ELMs and dithering cycles. For type-III ELMs, the precursor locates inside the separatrix, and it does not lead to particle transport into the SOL. The precursor gives rise to distant magnetic perturbations, thus it is suspected to originate from a current oscillations inside the separatrix.

Type-III ELMs compose a limit number of filaments. The primary filament is observed to be stronger in amplitude than the subsequent ones. Compared to type-III ELMs, dithering cycles tends to release more filaments. The density topology is not concentric with potential topology in filaments of both type-III ELM and dithering cycles. All the individual filaments carry a current component which generates a distant magnetic perturbations. However, it is difficult to evaluate the current topology inside the filaments due to the mutual interference between the multiple filaments. Dithering cycles are deemed to be a electrostatic scenario as intermediate phase between the L and H. Our work provides the first explanation for origination of the widely observed magnetic fluctuations during the dithering phase.

In a type-I ELM like operational regime, the ELM events are observed to excite a solitary magnetic perturbations. It is found to originate from propagation of magnetic field aligned current filaments. The hodograph of radial and poloidal magnetic perturbations associated with current filament exhibits a elliptical trajectory, which indicates a monopolar current component persisting in the filaments.

The particle, heat and momentum transported in type-I ELMs are observed to one order higher than in type-III ELMs. Specifically, the convective and conductive transport almost break even during heat transport during ELMs. The Reynolds stress dominantly drive the radial transport of poloidal momentum, whereas the convective momentum lead the radial transport of toroidal momentum at ELM events. The grade of Reynolds stress driven momentum and convective momentum during ELMs are reversed in the scenario of radial transport of toroidal momentum with respected to the radial transport of poloidal momentum transport.

6.2. Outlook

This thesis presents the characteristics of plasma filaments observed in the L-mode and H-mode plasma using probe diagnostic. Regrettably, the dynamics of filaments are not well resolved among probe tips due to the fast movements of filaments. On the other hand, the filaments extend several meters along the magnetic field. It is difficult to evaluate the global movement of filaments from local probe measurements. Wide angle coverage diagnostic are desirable to facilitate the investigation of filaments.

Recently, the GPI diagnostic are set up to view turbulence in boundary plasma. It provide a capability on the studying of filament dynamics by tracing the filaments in 2D view (130×130 mm square, with 65 mm outside the separatrix and 65 mm inside the separatrix). The spatial resolution of the optical system is 2 mm at the gas cloud plane, which is smaller than the typical edge turbulence structure size of 10~30 mm measured by reciprocating probes on EAST. The temporal resolution is 2.56 μs per frame and the exposure time is 2.156 μs, which are much shorter than the typical autocorrelation time of the edge turbulent eddy of 10~20 μs. Figure 6.1 clearly shows the birth and movements of coherent structures/filaments during one type-III ELM in GPI visual field. The forward research are envisaged to characterize the dynamics of ELM filaments using GPI diagnostic system.

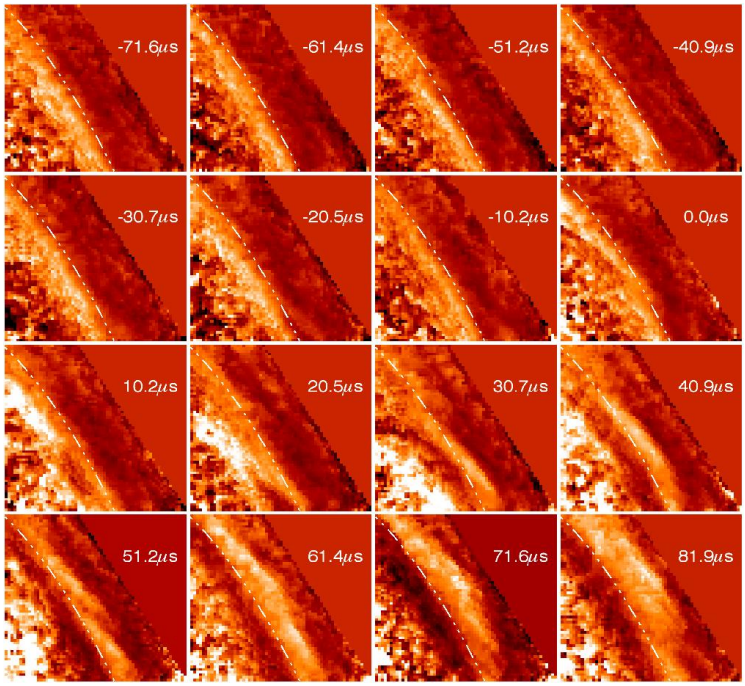

Figure 6.1. GPI imaging of 2D turbulence field during a type-III ELM event. The dashed lines indicate the locations of the separatrix.

Reference

[1]F. F. Chen, Springer (2011).
[2]J. Wesson, Oxford University Press (2004).
[3]J. P. Freidberg, Cambridge University Press (2007).
[4]J. D. Lawson, Proceedings of the Physical Society B **70**, 6 (1957).
[5]Y. Andrew *et al.*, Europhysics Letters **83**, 15003 (2008).
[6]R. Brakel, Plasma Phys. Control. Fusion **39**, B273 (1997).
[7]K. H. Burrell *et al.*, Plasma Phys. Control. Fusion **31**, 1649 (1989).
[8]J. W. Coenen *et al.*, Journal of Physics B: Atomic, Molecular and Optical Physics **43**, 144015 (2010).
[9]T. Happel *et al.*, Physics of Plasmas **18**, 102302 (2011).
[10]K. Ida, S. Kado, and Y. Liang, Review of Scientific Instruments **71**, 2360 (2000).
[11]K. Kamiya *et al.*, Nuclear Fusion **51**, 053009 (2011).
[12]R. M. McDermott *et al.*, Physics of Plasmas **16**, 056103 (2009).
[13]J. Schirmer*et al.*, Nuclear Fusion **46**, S780 (2006).
[14]G.S.Xu, Chin Phys Lett **31**, 137.
[15]M. Hirsch, Contributions to Plasma Physics **50**, 487 (2010).
[16]K. Kamiya *et al.*, Physical Review Letters **105** (2010).
[17]H. Meyer *et al.*, Nuclear Fusion **51**, 113011 (2011).
[18]H. Mastsusmoto *et al.*, Plasma Physics and Controlled Fusion **34**, 615 (1992).
[19]R. Groebner *et al.*, Physical Review Letters **64**, 3015 (1990).
[20]E. Viezzer *et al.*, Nuclear Fusion **53**, 053005 (2013).
[21]A. Hassam *et al.*, Physical Review Letters **66**, 309 (1991).
[22]T. Stringer, Physical Review Letters **22**, 770 (1969).
[23]K. Shaing and E. Crume, Physical Review Letters **63**, 2369 (1989).
[24]J. A. Heikkinen, Plasma Phys. Control. Fusion **40**, 693 (1998).
[25]P. H. Diamond *et al.*, Physics of Fluids B: Plasma Physics **3**, 1626 (1991).
[26]Y. H. Xu, Physical Review Letters **84**, 3867 (2000).
[27]B. D. Scott, Contributions to Plasma Physics **46**, 714 (2006).
[28]T. T. Ribeiro *et al.*, Plasma Physics and Controlled Fusion **47**, 1657 (2005).
[29]O. E. Garcia *et al.*, Physics of Plasmas **13**, 082309 (2006).
[30]B. K. H, Science **281**, 1816 (1998).
[31]S. Jachmich, Plasma Phys. Control. Fusion **40**, 1105 (1998).
[32]E.-j. Kim, Journal of Physics: Conference Series **44**, 10 (2006).
[33]G. R. Tynan, Plasma Phys. Control. Fusion **38**, 1301 (1996).
[34]V. Antoni, Plasma Phys. Control. Fusion **42**, 83 (2000).
[35]T. A. Carter and J. E. Maggs, Physics of Plasmas **16**, 012304 (2009).
[36]S. K. Saha *et al.*, Plasma Physics and Controlled Fusion **46**, 1065 (2004).
[37]M. Shats *et al.*, Physical Review Letters **99** (2007).
[38]P. Gohil, Nuclear Fusion **38** (1998).
[39]J. Boedo, Nuclear Fusion, **40**, 1397 (2000).
[40]G. R. Tynan *et al.*, Physics of Plasmas **1**, 3301 (1994).
[41]R. A. Moyer *et al.*, Physics of Plasmas **2**, 2397 (1995).
[42]V. Antoni, Plasma Phys. Control. Fusion **42**, 83 (2000).

[43] J. A. Boedo, Nucl. Fusion **42**, 117 (2002).
[44] H. Y. Guo *et al.*, Journal of Nuclear Materials **415**, S369 (2011).
[45] B. Wan, J. Li, H. Guo, Y. Liang, and G. Xu, Nuclear Fusion **53**, 104006 (2013).
[46] J. Li *et al.*, Nature Physics **9**, 817 (2013).
[47] T. Ido *et al.*, Nuclear Fusion **46**, 512 (2006).
[48] P. C. Stangeby, Nuclear Fusion **30** 1225 (1990).
[49] N. Mahdizadeh *et al.*,, Plasma Physics and Controlled Fusion **47**, 569 (2005).
[50] R. Schrittwieser, Plasma Phys. Control. Fusion **44**, 567 (2002).
[51] J. Horacek, J. Adamek, H. W. Müller, J. Seidl, A. H. Nielsen, V. Rohde, F. Mehlmann, C. Ionita, and E. Havlíčková, Nuclear Fusion **50**, 105001 (2010).
[52] H. W. Müller *et al.*, Nuclear Fusion **51**, 073023 (2011).
[53] I. H. Hutchinson, Physics of Plasmas **9**, 1832 (2002).
[54] L. Oksuz and N. Hershkowitz, Plasma Sources Science and Technology **13**, 263 (2004).
[55] P. C. Stangeby, Physics of Fluids **27**, 2699 (1984).
[56] K. S. Chung and I. Hutchinson, Physical Review A **38**, 4721 (1988).
[57] E. Ko and N. Hershkowitz, Plasma Physics and Controlled Fusion **48**, 621 (2006).
[58] C. S. MacLatchy, C. Boucher, D. A. Poirier, and J. Gunn, Review of Scientific Instruments **63**, 3923 (1992).
[59] W. Zhang *et al.*, The Review of scientific instruments **81**, 113501 (2010).
[60] L. Wang *et al.*, Nuclear Fusion **52**, 063024 (2012).
[61] L. M. Shao *et al.*, Plasma Physics and Controlled Fusion **55**, 105006 (2013).
[62] S. I. Krasheninnikov, Phys. Lett. A **283**, 368 (2001).
[63] D. A. D'Ippolito, J. R. Myra, and S. I. Krasheninnikov, Physics of Plasmas **9**, 222 (2002).
[64] V. Naulin, Journal of Nuclear Materials **363-365**, 24 (2007).
[65] O. E. Garcia *et al.*, Physics of Plasmas **12**, 062309 (2005).
[66] J. L. Terry *et al.*, Physics of Plasmas **10**, 1739 (2003).
[67] I. Furno *et al.*, Physical Review Letters **100** (2008).
[68] Y. H. Xu *et al.*, Plasma Physics and Controlled Fusion **47**, 1841 (2005).
[69] S. H. Müller *et al.*, Physics of Plasmas **13**, 100701 (2006).
[70] S. J. Zweben *et al.*, Nuclear Fusion **44**, 134 (2004).
[71] M. Agostini *et al.*, Physics of Plasmas **14**, 102305 (2007).
[72] J. A. Boedo *et al.*, Physics of Plasmas **10**, 1670 (2003).
[73] G. Serianni *et al.*, Plasma Physics and Controlled Fusion **49**, B267 (2007).
[74] A. Loarte *et al.*, Nuclear Fusion **47**, S203 (2007).
[75] B. LaBombard *et al.*, Physics of Plasmas **8**, 2107 (2001).
[76] S. K. Erents *et al.*,Plasma Physics and Controlled Fusion **46**, 1757 (2004).
[77] O. E. Garcia *et al.*, Nuclear Fusion **47**, 667 (2007).
[78] B. LaBombard *et al.*, Nuclear Fusion **44**, 1047 (2004).
[79] J. R. Myra *et al.*, Physics of Plasmas **13**, 092509 (2006).
[80] B. Nold *et al.*,New Journal of Physics **14**, 063022 (2012).
[81] O. Garcia *et al.*, Physical Review Letters **92**, 165003 (2004).

[82]O. E. Garcia *et al.*, Plasma Physics and Controlled Fusion **48**, L1 (2006).
[83]C. Theiler *et al.*,Physical Review Letters **103** (2009).
[84]T. Windisch *et al.*, Physics of Plasmas **13**, 122303 (2006).
[85]T. Happel *et al.*, Physical Review Letters **102** (2009).
[86]R. J. Maqueda and D. P. Stotler, Nuclear Fusion **50**, 075002 (2010).
[87]G. S. Xu *et al.*, Nuclear Fusion **49**, 092002 (2009).
[88]B. Nold *et al.*, Plasma Physics and Controlled Fusion **52**, 065005 (2010).
[89]J. Cheng *et al.*, Plasma Physics and Controlled Fusion **52**, 055003 (2010).
[90]P. Manz *et al.*, Physical Review Letters **107** (2011).
[91]F. Militello *et al.*, Plasma Physics and Controlled Fusion **55**, 025005 (2013).
[92]R. Dejarnac *et al.*,Plasma Physics and Controlled Fusion **49**, 1791 (2007).
[93]M. Kočan *et al.*, Plasma Physics and Controlled Fusion **54**, 085009 (2012).
[94]N. Mattor *et al.*, Physical Review Letters **72**, 486 (1994).
[95]K. H. Burrell, Plasma Physics and Controlled Fusion **48**, A347 (2006).
[96]T. Estrada *et al.*, Nuclear Fusion **51**, 032001 (2011).
[97]F. Sattin *et al.*, Plasma Physics and Controlled Fusion **51**, 055013 (2009).
[98]F. Sattin *et al.*, Physica Scripta **79**, 045006 (2009).
[99]P. Sura *et al.*, Journal of Physical Oceanography **38**, 639 (2008).
[100]S. Alberghi *et al.*, J. Appl. Meteorol. **41**, 885 (2002).
[101]B. Labit *et al.*, Physical Review Letters **98** (2007).
[102]M. Cristelli *et al.*, Physical Review E **85** (2012).
[103]I. Sandberg *et al.*, Physical Review Letters **103** (2009).
[104]O. E. Garcia, Physical Review Letters **108** (2012).
[105]J. P. Graves *et al.*, Plasma Physics and Controlled Fusion **47**, L1 (2005).
[106]F. Sattin *et al.*, Physics of Plasmas **11**, 5032 (2004).
[107]J. A. Krommes, Physics of Plasmas **15**, 030703 (2008).
[108]A. V. Filippas *et al.*,Physics of Plasmas **2**, 839 (1995).
[109]A. H. Nielsen *et al.*, Physics of Plasmas **3**, 1530 (1996).
[110]D. A. D'Ippolito *et al.*, Physics of Plasmas **18**, 060501 (2011).
[111]T. A. Carter, Physics of Plasmas **13**, 010701 (2006).
[112]M. Spolaore *et al.*, Physical Review Letters **102** (2009).
[113]P. H. Diamond *et al.*, Plasma Physics and Controlled Fusion **47**, R35 (2005).
[114]A. Fujisawa *et al.*, Physical Review Letters **93** (2004).
[115]C. Silva *et al.*, Plasma Physics and Controlled Fusion **55**, 025001 (2013).
[116]A. Liu *et al.*, Physical Review Letters **103** (2009).
[117]D. Gupta *et al.*, Physical Review Letters **97** (2006).
[118]Y. Hamada *et al.*, Nuclear Fusion **45**, 81 (2005).
[119]G. R. McKee *et al.*, Physics of Plasmas **10**, 1712 (2003).
[120]V. A. Vershkov *et al.*, Nuclear Fusion **45**, S203 (2005).
[121]G. D. Conway *et al.*, Plasma Physics and Controlled Fusion **47**, 1165 (2005).
[122]G. R. McKee, Plasma Phys. Control. Fusion **45**, A477 (2003).
[123]J. Hugill, Journal of Nuclear Materials **196-198**, 918 (1992).
[124]W. Fundamenski *et al.*, Nuclear Fusion **47**, 417 (2007).
[125]S. K. Erents, Plasma Phys. Control. Fusion **42**, 905 (2000).

[126]N. Asakura, Journal of Nuclear Materials **363-365**, 41 (2007).
[127]N. Asakura *et al.*, Nuclear Fusion **44**, 503 (2004).
[128]N. Asakura, Physical Review Letters **3093-3096** (2000).
[129]R. A. Pitts *et al.*, Journal of Nuclear Materials **363-365**, 505 (2007).
[130]T. D. Rognlien, Journal of Nuclear Materials **266-269**, 654 (1999).
[131]A. V. Chankin, Journal of Nuclear Materials **241-243**, 199 (1997).
[132]M. Kočan *et al.*, Journal of Nuclear Materials **415**, S1133 (2011).
[133]M. Kočan *et al.*, Journal of Nuclear Materials **390-391**, 1074 (2009).
[134]M. Kočan *et al.*, Journal of Nuclear Materials **363-365**, 1436 (2007).
[135]M. Reich *et al.*, Plasma Physics and Controlled Fusion **46**, 797 (2004).
[136]A. Huber, Plasma Phys. Control. Fusion **42**, 569 (2000).
[137]F. Wagner *et al.*, Physical Review Letters **49**, 1408 (1982).
[138]F. Wagner, Plasma Physics and Controlled Fusion **49**, B1 (2007).
[139]Y. R. Martin *et al.*, Journal of Physics: Conference Series **123**, 012033 (2008).
[140]E. Wolfrum *et al.*, Plasma Physics and Controlled Fusion **54**, 124002 (2012).
[141]Y. Ma *et al.*, Nuclear Fusion **52**, 023010 (2012).
[142]J. W. Connor, Plasma Phys. Control. Fusion **42**, R1 (2000).
[143]W. Fundamenski *et al.*, Nuclear Fusion **52**, 062003 (2012).
[144]Z. Lin, Science **281**, 1835 (1998).
[145]S.-I. ITOH, Nuclear Fusion **29**, 1031 (1989).
[146]E.-j. Kim *et al.*, Physical Review Letters **90**, 185006 (2003).
[147]K. C. Shaing *et al.*, Physics of Plasmas **2**, 1801 (1995).
[148]B. A. Carreras *et al.*, Physics of Plasmas **3**, 4106 (1996).
[149]A. Scaggion *et al.*, 39th EPS Conference & 16th Int. Congress on Plasma Physics, P2.903.
[150]Y. Andrew *et al.*, Plasma Physics and Controlled Fusion **46**, A87 (2004).
[151]C. Bourdelle *et al.*, Nuclear Fusion **54**, 022001 (2014).
[152]C. F. Maggi *et al.*, Nuclear Fusion **54**, 023007 (2014).
[153]F. Ryter *et al.*, Nuclear Fusion **49**, 062003 (2009).
[154]G. S. Xu *et al.*, Nuclear Fusion **51**, 072001 (2011).
[155]P. N. Guzdar, Physics of Plasmas **2**, 4174 (1995).
[156]H. Q. Wang *et al.*, Nuclear Fusion **52**, 123011 (2012).
[157]G. S. Xu *et al.*, Physics of Plasmas **19**, 122502 (2012).
[158]K. Kamiya *et al.*, Plasma Physics and Controlled Fusion **49**, S43 (2007).
[159]A. Kirk *et al.*, Physical Review Letters **96** (2006).
[160]A. Kirk *et al.*, Physical Review Letters **92** (2004).
[161]N. Oyama *et al.*, Nuclear Fusion **44**, 582 (2004).
[162]L. Zeng *et al.*, Plasma Physics and Controlled Fusion **46**, A121 (2004).
[163]T. Eich *et al.*, Journal of Nuclear Materials **337-339**, 669 (2005).
[164]H. Zohm, Plasma Phys. Control. Fusion **38**, 105 (1996).
[165]T. H. Osborne *et al.*, Journal of Physics: Conference Series **123**, 012014 (2008).
[166]N. Oyama *et al.*, Nuclear Fusion **45**, 871 (2005).
[167]Y. Kamada, Plasma Phys. Control. Fusion **42**, A247 (2000).
[168]A. C. Sontag *et al.*, Nuclear Fusion **51**, 103022 (2011).

[169]R. Colchin *et al.*, Physical Review Letters **88** (2002).
[170]L. Schmitz *et al.*, Physical Review Letters **108** (2012).
[171]G. D. Conway *et al.*, Physical Review Letters **106** (2011).
[172]P. B. Snyder *et al.*, Plasma Physics and Controlled Fusion **46**, A131 (2004).
[173]H. Wilson *et al.*,Physical Review Letters **92** (2004).
[174]G. S. Yun *et al.*, Physical Review Letters **107** (2011).
[175]R. J. Maqueda *et al.*, Journal of Nuclear Materials **390-391**, 843 (2009).
[176]J. A. Boedo *et al.*, Physics of Plasmas **12**, 072516 (2005).
[177]T. Eich *et al.*, Plasma Physics and Controlled Fusion **47**, 815 (2005).
[178]M. Endler *et al.*, Plasma Physics and Controlled Fusion **47**, 219 (2005).
[179]C. Silva *et al.*, Plasma Physics and Controlled Fusion **51**, 105001 (2009).
[180]R. A. Pitts *et al.*, Nuclear Fusion **47**, 1437 (2007).
[181]A. Kirk *et al.*, Plasma Physics and Controlled Fusion **47**, 315 (2005).
[182]J. Neuhauser *et al.*, Nuclear Fusion **48**, 045005 (2008).
[183]R. A. Pitts, 34th EPS Conference on Plasma Physics (2007).
[184]C. Maszl *et al.*, Journal of Nuclear Materials **415**, S451 (2011).
[185]P. Migliucci *et al.*, Physics of Plasmas **17**, 072507 (2010).
[186]E. R. Solano *et al.*, Physical Review Letters **104** (2010).
[187]N. Vianello *et al.*, Physical Review Letters **106** (2011).
[188]J. R. Myra, Physics of Plasmas **14**, 102314 (2007).
[189]G. S. Xu *et al.*,Physics of Plasmas **17**, 022501 (2010).
[190]H. Takahashi, 32nd EPS Conference on Plasma Phys. **29C**, P (2005).
[191]T. E. Evans *et al.*, Journal of Nuclear Materials **390-391**, 789 (2009).
[192]A. Wingen *et al.*, Physical Review Letters **104** (2010).
[193]L. Zheng *et al.*, Physical Review Letters **100** (2008).
[194]E. Martines *et al.*, Plasma Physics and Controlled Fusion **51**, 124053 (2009).
[195]A. Kirk *et al.*, Plasma Physics and Controlled Fusion **48**, B433 (2006).
[196]A. Schmid *et al.*, Plasma Physics and Controlled Fusion **50**, 045007 (2008).
[197]N. Asakura, physical Review Letters **84**, 3093 (2000).
[198]M. Jiang *et al.*, Plasma Physics and Controlled Fusion **54**, 095003 (2012).
[199]G. Bateman *et al.*, Plasma Physics and Controlled Fusion **48**, A93 (2006).
[200]H. Zohm, Nuclear Fusion **32** (1992).
[201]G. J. Liu *et al.*, Review of scientific instruments **84**, 073502 (2013).
[202]A. Kirk *et al.*, Plasma Physics and Controlled Fusion **47**, 995 (2005).
[203]J. Ellis and A. Dogariu, Physical Review Letters **95** (2005).
[204]M. A. Alonso and E. Wolf, Optics Communications **281**, 2393 (2008).
[205]J. Ellis *et al.*, Optics Communications **248**, 333 (2005).
[206]P. Sun *et al.*, Journal of Optics **15**, 055708 (2013).
[207]A. A. Qasimi, Optics Letters **32**, 1015 (2007).
[208]T. Zhang *et al.*, Physics Letters A **377**, 1725 (2013).
[209]J. Cheng *et al.*, Physical Review Letters **110** (2013).
[210]V. Rozhansky *et al.*, Plasma Physics and Controlled Fusion **50**, 025008 (2008).
[211]A. V. Khrabro, Journal of Geophysical Research **103**, 11 (1998).
[212]F. Levinton *et al.*, R. P. Wenninger *et al.*, Nuclear Fusion **52**, 114025 (2012).

[214]F. Sommer *et al.*, Plasma Physics and Controlled Fusion **53**, 085012 (2011).
[215]T. W. Versloot *et al.*, Plasma Physics and Controlled Fusion **52**, 045014 (2010).
[216]F. Mehlmann, 37th EPS Conference on Plasma Physics **P1.1064** (2010).
[217]F. Mehlmann, 39th EPS Conference & 16th Int. Congress on Plasma Physics **P2.090** (2012).